

**SMALL SIGNAL STABILITY ANALYSIS OF A
VOLTAGE SOURCE CONVERTER (VSC) BASED HIGH
VOLTAGE DIRECT CURRENT SYSTEM WITH
ONSHORE WIND POWER GENERATION**

Nsofwa M. Kangwa

IN FULFILMENT OF THE MASTER OF SCIENCE DEGREE IN ENGINEERING

COLLEGE OF AGRICULTURE, ENGINEERING AND SCIENCE

UNIVERSITY OF KWAZULU-NATAL

December 2017

Supervisor: Prof. D. Dorrell

Co-Supervisor: Dr. C. Venugopal

EXAMINER'S COPY

DECLARATION 1 - PLAGIARISM

I, Nsofwa M. Kangwa, declare that


1. The research reported in this dissertation, except where otherwise indicated, is my original research.
2. This dissertation has not been submitted for any degree or examination at any other university.
3. This dissertation does not contain other person's data, pictures, graphs or other information unless specifically acknowledged as being sourced from other persons.
4. This dissertation does not contain other person's writing unless specifically acknowledged as being sourced from other researchers. Where other written sources have been quoted, then:
 - a. Their words have been re-written but the general information attributed to them has been referenced.
 - b. Where their exact words have been used, then their writing has been placed in italics and inside quotation marks and referenced.
5. This dissertation does not contain text, graphics or tables copied and pasted from the internet, unless specifically acknowledged, and the source being detailed in the thesis and in the Reference sections.

Signed:

.....

Ms. Nsofwa M. Kangwa

As the candidate's Supervisor, I agree to the submission of this thesis.

Signed: 

.....

Professor David G. Dorrell

Date: 10/01/2018

Dedicated to my greatest cheerleaders, my family, for your endless encouragement and support.

ACKNOWLEDGEMENTS

First and foremost, I would like to thank the almighty God, who has been my source of strength throughout my entire research program. I would not have been able to achieve anything if it were not for His love and grace.

Secondly, I would also like to express my gratitude to the following people, whose invaluable contribution helped put my research together:

- My supervisors, Professor David Dorrell and Dr. Chitra Venugopal for their guidance and support during my work.
- My family and friends, the greatest support structure. Thank you for always believing in me and lifting me up whenever I needed the boost.
- Eskom, for their financial support, through the Eskom Power Plant Engineering Institute (EPPEI) Program.

ABSTRACT

Advances in power electronics over several decades has led to high voltage direct current (HVDC) transmission emerging as a good option for electricity transmission in many circumstances, and it is able to integrate with, and augment, conventional high voltage alternating current (HVAC) transmission. This is because HVDC provides enhanced system operation and improved support in the development of onshore and offshore transmission networks. Because of its speed and flexibility, HVDC technology can provide transmission systems with several advantages such as transfer capacity enhancement, better power flow control, transient stability improvement, damping of power oscillations, enhanced voltage stability and control, rejection of cascading disturbances, and the absence of reactive power generation or absorption by the cable or line.

In Africa, there are three HVDC systems. The Caprivi Link Interconnector between Zambia and Namibia is the first and only one on the continent employing voltage source converters (VSC), as opposed to conventional line commutated converters (LCC). HVDC VSCs use insulated gate bipolar transistors (IGBTs) technology as switches. IGBTs provide more controllability and flexibility than the thyristors used in LCC technology. These features make them suitable for implementation in multi-terminal HVDC networks; which are envisaged to form HVDC grids in future. The Caprivi Link interconnector is therefore a pioneering project in the development of electricity transmission in Africa. The southern African power pool (SAPP) currently has inadequate electricity generation capacity. Investing in more renewable energy options, such as wind generation, coupled with the use of HVDC transmission, could be possible remedies for this.

The aim of this research was to investigate small signal stability issues that can be present in VSC-HVDC systems. The Caprivi Link Interconnector is used as the contextualization of the investigated system. Different conditions such as AC system strength, controller parameter and wind power generation levels are investigated for their influence on the small signal stability of the system. Small signal stability analysis is also investigated for different HVDC configurations. It is found that the systems experience both electromagnetic as well as sub-synchronous oscillations. The sub-synchronous oscillations are generally well damped and only affect the DC impedances. Power System Stabilizers (PSS) as well as Thyristor Controlled Series Compensators (TCSC) are implemented as mitigation for the electromagnetic modes.

DECLARATION 2 – WORKSHOP AND PUBLICATION

The following workshop output and publication emanated from this research investigation:

- [1] N. Kangwa, D. G. Dorrell and C. Venugopal, “Small Signal Stability analysis of a VSC-based HVDC system with wind power generation.” *Proceedings of the 4th Eskom Power Plant Engineering Institute Student Workshop*, Eskom Academy of Learning, Midrand, South Africa, 29-30 May 2017.

- [2] N Kangwa, I. E. Davidson and C. Venugopal, “A review of the performance of VSC-HVDC and MTDC systems.” *Proceedings of the IEEE PES Power Africa Conference*, Accra, Ghana, 27-30 June 2017, pages 267-273.

Signed:

TABLE OF CONTENTS

DECLARATION 1 - PLAGIARISM	ii
ACKNOWLEDGEMENTS.....	iv
ABSTRACT	v
DECLARATION 2 – WORKSHOP AND PUBLICATION	vi
LIST OF FIGURES.....	xi
LIST OF TABLES	xiv
LIST OF ABBREVIATIONS.....	xv
1 INTRODUCTION.....	1
1.1 Background	1
1.2 Problem Statement	2
1.3 Key Research Questions	3
1.4 Aims and Objectives	3
1.5 Methodology	4
1.5.1 Simulation Tool.....	4
1.5.2 Research Process	4
1.6 Scope and Limitations.....	6
1.7 Significance of the Study and Project Contribution.....	7
1.8 Outline of Thesis.....	7
2 LITERATURE REVIEW.....	9
2.1 The Evolution of Power Systems	9
2.2 HVAC and HVDC Transmission.....	9
2.3 Advantages of HVDC	10
2.4 HVDC Converters.....	10
2.5 HVDC Topologies	12
2.6 Existing projects in HVDC	13
2.6.1 Gotland HVDC Link	13
2.6.2 Sardinia-Corsica-Italy	13
2.6.3 Hydro Quebec-New England Interconnection	14
2.6.4 Caprivi-Link Interconnector.....	15
2.7 Control of VSC-HVDC.....	16
2.7.1 Direct Control.....	16
2.7.2 Vector Oriented Control.....	17
2.8 Wind Energy Systems	18
2.8.1 Components of a Wind Turbine	19
2.9 Types of Wind Turbines.....	20

2.9.1	Fixed Speed Wind Turbines	20
2.9.2	Limited Variable-Speed Wind Turbines	21
2.9.3	Partial-Scale Converter Variable Speed Wind Turbines	22
2.9.4	Full Scale Converter Variable Speed Wind Turbines	22
2.10	Power System Stability	23
2.11	Rotor Angle Stability	24
2.11.1	Transient Stability	24
2.11.2	Small Signal Stability.....	28
2.11.3	Types of Modes.....	32
2.11.4	Right Eigenvector.....	33
2.11.5	Left Eigenvector.....	34
2.11.6	Participation Factors.....	34
2.11.7	Observability and Controllability.....	35
3	COMPONENT MODELLING	36
3.1	Model Contextualization.....	36
3.2	DC POWER RATING	37
3.3	DC Line.....	37
3.4	Converter Sizing	37
3.5	Transformer Sizing.....	38
3.5.1	Transformer on the Zambia side	38
3.5.2	Transformer on the Namibia side.....	38
3.6	DC Capacitor Sizing	38
3.7	Phase Reactors	39
3.7.1	AC Phase Reactors.....	39
3.7.2	DC Line Phase Reactors.....	40
3.8	Control System.....	40
3.9	Inner Current Control Loop	41
3.9.1	PI Regulator	42
3.9.2	PWM Converter	42
3.9.3	System.....	42
3.10	Outer Controller Loops	42
3.10.1	DC Voltage Control	42
3.10.2	Active and Reactive Power Control.....	43
3.10.3	AC Voltage Control	43
3.11	Wind Farm Modelling.....	44
3.11.1	IEC 61400-27-1 Type 3a Wind Turbine Model.....	45
3.11.2	Mathematical Model of DFIG.....	45

3.11.3	Voltage Equations	46
3.11.4	Flux Equations	46
3.11.5	Equation of Motion	46
3.12	Modal Analysis	47
4	MODEL VALIDATION AND TESTING	49
4.1	Base Case	49
4.1.1	HVDC Parameters.....	49
4.2	VSC Controller Parameters.....	51
4.2.1	Inner Controller	51
4.2.2	Outer Controller	51
4.3	Controller Step response test.....	52
4.4	Base Case Modal Analysis.....	53
5	RESULTS AND ANALYSIS.....	55
5.1	Monopole with Wind Power Generation	55
5.2	Small SIGNAL Stability Analysis	57
5.2.1	Participation Factor Analysis of New Modes	58
5.2.2	Time Domain Analysis	60
5.3	The effect of SCR on small signal stability.....	60
5.4	Effect of change in Inner (Current) Controller Gain.....	62
5.5	Effect of Outer (DC Voltage) Controller Gain.....	64
5.6	Effect of Varying Wind Power Output	65
5.7	Expansion of the Monopole to a Bipole VSC-HVDC Network	67
5.8	Effect of SCR on Small Signal Stability	69
5.9	Effect of Inner Current Controller Gain.....	70
5.10	Effect of Outer Controller Gain	72
5.11	Effect of Wind Power Output	74
5.12	Comparison: Monopole and Expansion to Bipole	75
5.12.1	Time domain Analysis	75
5.12.2	Effects of Different conditions.....	75
5.13	Power Oscillation Damping	77
5.13.1	Power System Stabilizers	77
5.13.2	Residue Based Tuning of the PSS.....	78
5.13.3	Phase Compensator Design.....	79
5.13.4	Optimization of the PSS Gain.....	79
5.14	PSS Design for Monopole Configuration	80
5.15	PSS Design for Bipole configuration.....	86
5.16	Design of TCSC for Monopole and Bipole configurations.....	90

5.17	PSS AND TCSC TIME DOMAIN ANALYSIS.....	95
5.18	Conclusions.....	96
6	CONCLUSIONS AND RECOMMENDATIONS.....	98
6.1	Conclusions.....	98
6.2	Recommendations for Future Research	99
	REFERENCES.....	101
	APPENDIX.....	109

LIST OF FIGURES

Figure 1-1 Simulation Process	6
Figure 2-1 Monopole back-to-back HVDC Configuration [21]	12
Figure 2-2 Monopolar configuration [21]	12
Figure 2-3 Bipolar configuration [21]	13
Figure 2-4 Sardinia-Corsica-Italy Interconnection [16]	14
Figure 2-5 Hydro Quebec New England Interconnection [16]	14
Figure 2-6 Caprivi Link Interconnector [35]	15
Figure 2-7 VSC-HVDC Overview [50]	17
Figure 2-8 Inner Current Control Loop	18
Figure 2-9 Parts of a wind turbine [59]	18
Figure 2-10 Wind turbine speed characteristics [60]	20
Figure 2-11 Fixed Speed Wind Energy System [63]	21
Figure 2-12 Limited Speed Variable Speed Wind Energy System	21
Figure 2-13 Double Fed Induction Generator (DFIG) Configuration [66]	22
Figure 2-14 Full Scale Power Wind Energy System [66]	23
Figure 2-15 Power System Stability Classification [69]	23
Figure 2-16 Power Angle Relationship	25
Figure 2-17 Equal Area Criterion (δ_c set to the critical value δ_{cr})	28
Figure 2-18 State Space representation of a system	29
Figure 2-19 VSC-HVDC Control Structure	30
Figure 2-20 The S Plane	32
Figure 3-1 Simplified Representation of VSC-HVDC System [52]	36
Figure 3-2 Simplified Representation of Caprivi Link Interconnector [3]	36
Figure 3-3 Vector control transformation axes [83]	41
Figure 3-4 VSC Model Single Line Diagram [80]	41
Figure 3-5 Inner current controller block diagram	41
Figure 3-6 DC voltage controller block diagram [52]	43
Figure 3-7 Active and Reactive power controller blocks [52]	43
Figure 3-8 AC Voltage control block [80]	44
Figure 4-1 Base Case Network	50
Figure 4-2 Inner Controller Block Diagram	51
Figure 4-3 AC Voltage Step Response Test	52
Figure 4-4 DC Voltage Step Response Test	52
Figure 4-5 Eigenvalue plot of base case	53
Figure 5-1 Monopole with wind power generation network	56

Figure 5-2 Eigenvalues of Monopole with Wind Generation	57
Figure 5-3 Participation factor of added modes	59
Figure 5-4 Time domain comparison with and without wind power generation	60
Figure 5-5 Effect of Change in SCR on Eigenvector Trajectory	61
Figure 5-6 Effect of change in SCR on Damping Ratio of modes 18 & 19.....	61
Figure 5-7 Effect of change in SCR on Damping Ratio of modes 22 & 23.....	62
Figure 5-8 Effect of Varying Inner Current Gain	63
Figure 5-9 Effect of varying Inner Current Controller Gain on Modes 18 & 19.....	63
Figure 5-10 Effect of varying Inner Current Controller Gain on Modes 22 & 23.....	64
Figure 5-11 Effect of varying Outer Controller Gain	64
Figure 5-12 Effect of varying Outer Controller Gain on modes 18 & 19.....	65
Figure 5-13 Effects of varying Outer Controller Gain on modes 22 & 23	65
Figure 5-14 Effect of varying wind speed.....	66
Figure 5-15 Effect of Wind Power Output on Damping Ratio of different modes.....	67
Figure 5-16 Eigenvalues for Bipole expansion.....	69
Figure 5-17 Effect of change in SCR on Eigenvectors	70
Figure 5-18 Effect of Varying Inner Current Controller Gain	71
Figure 5-19 Effect of Varying Outer Controller Gain.....	73
Figure 5-20 Effect on Varying Wind Power Output of Eigenvector Trajectory.....	74
Figure 5-21 Time domain of monopole and bipole expansion rotor oscillations.....	75
Figure 5-22 Monopole and Bipole Comparison with varying SCR.....	76
Figure 5-23 Monopole and Bipole Comparison with varying inner current controller gain.....	76
Figure 5-24 Monopole and Bipole Comparison with varying outer controller gain.....	77
Figure 5-25 Monopole and Bipole Comparison with varying wind power output	77
Figure 5-26 Classical PSS block diagram [90]	78
Figure 5-27 Rotor Speed without PSS and AVR	80
Figure 5-28 Power System Stabilizer of PSS.....	80
Figure 5-29 Time domain analysis at Gain = 0.....	82
Figure 5-30 Time domain analysis at Gain = 10.....	83
Figure 5-31 Time domain analysis at Gain = 20.....	83
Figure 5-32 Time domain analysis at Gain = 30.....	84
Figure 5-33 Time domain analysis at Gain=40.....	85
Figure 5-34 Time domain analysis at Gain = 50.....	85
Figure 5-35 Time domain analysis at Gain = 80.....	86
Figure 5-36 Power System Stabilizer at Gain = 10.....	88
Figure 5-37 Power System Stabilizer at Gain = 20.....	88
Figure 5-38 Power System Stabilizer at Gain setting 30	89

Figure 5-39 Power System Stabilizer at Gain setting 40	90
Figure 5-40 TCSC Block Diagram [98].....	90
Figure 5-41 TCSC Gain Optimization	94
Figure 5-42 Monopole oscillation damping.....	95
Figure 5-43 Bipole oscillation damping.....	95

LIST OF TABLES

Table 2-1 Comparison of LCC and VSC	11
Table 2-2 Summary of other existing HVDC Projects around the world	16
Table 4-1 VSC-HVDC Parameters used in Base Case	49
Table 4-2 Outer Controller Parameters	51
Table 4-3 Base Case Eigenvalues	54
Table 5-1 Eigenvectors of VSC Monopole HVDC with wind power generation.....	58
Table 5-2 Eigenvectors of bipole expansion.....	68
Table 5-3 Effect of SCR on Damping Ratio	70
Table 5-4 Eigenvectors of Modes affected by change in Inner Current Controller Gain	71
Table 5-5 Effects of Varying Current Controller Gain on Damping Ratio.....	72
Table 5-6 Eigenvectors of Modes affected by change in Outer Controller Gain.....	73
Table 5-7 Effects of Varying Outer Controller Gain on Damping Ratio.....	73
Table 5-8 Eigenvectors of the poorly damped modes.....	74
Table 5-9 Damping Ratios of the poorly damped modes at different levels of wind power output	75
Table 5-10 Eigenvector with and without PSS	87
Table 5-11 TCSC design parameters	91

LIST OF ABBREVIATIONS

AC	Alternating Current
AVR	Automatic Voltage Regulator
CLI	Caprivi Link Interconnector
DC	Direct Current
DFIG	Doubly Fed Induction Generator
DQ	Direct Quadrature
FACTS	Flexible Alternating Current Transmission Systems
HVDC	High Voltage Direct Current
HVAC	High Voltage Alternating Current
IGBT	Insulated Gate Bipolar Transistor
LCC	Line Commutated Converter
LFO	Low Frequency Oscillations
MTDC	Multi Terminal Direct Current
PSS	Power System Stabilizer
PWM	Pulse Width Modulation
SCR	Short Circuit Ratio
SSCI	Sub-synchronous Control Interactions
SSO	Sub-synchronous Oscillations
SSR	Sub-synchronous Resonance
SSTI	Sub-synchronous Torsional Interaction
TCSC	Thyristor Controlled Series Capacitor
VSC	Voltage Source Converter

1 INTRODUCTION

1.1 BACKGROUND

Modern society revolves around a sound and stable electricity supply system [1]. Electricity has turned into an essential need for modern living with applications ranging from industry, transport to household use. Coupled with water, sanitation and food supply, electricity is classed as an essential by many. In a power system, electricity is generated, transmitted and distributed to consumers in a manner that is reliable, cost-effective and efficient. It consists of generating stations, transmission lines or cables, substations for transformation and connection, and distribution systems.

Therefore, it is essential that a sustainable power system is one that efficiently transmits electricity from its place of production to the consumer. A power system must be capable of maintaining a continuous and secure supply to suit the frequently changing load demands. There are a number of the vital issues concerning the technical performance of a network at both transmission and distribution level that should be dealt with in the designing and assessing of a power system. For an electrical system to be considered effective, it should have the capacity to appropriately address certain issues such as reliability of supply, quality of supply as well as economic and environmentally friendly generation and transmission [2].

High voltage alternating current (HVAC) transmission has been the usual means of electrical power transmission since the late 19th century. Development of power electronics has led to the development high voltage direct current (HVDC) transmission. This is used to improve system operation and support onshore and offshore transmission systems. Because of its speed and flexibility, HVDC technology is capable of providing the transmission system with a number of benefits such as transfer capacity enhancement, better regulation of power flow, improvement of transient stability, power oscillations damping, enhanced voltage stability and control, rejection of cascading disturbances, and the absence of reactive power generation or absorption by the line or cable. Only three HVDC links currently exist in Africa. The Cahora Bassa HVDC link transmits electricity between Songo in Mozambique and Apollo in South Africa. This HVDC link employs Line Commutated Converters (LCC), as does the Inga-Kolwezi HVDC link in the Democratic Republic of Congo. The third HVDC link is the Caprivi Link Interconnector which is the only HVDC link in Africa which employs Voltage Source Converters (VSCs) and transmits electricity between Zambia and Gerus in Namibia. VSC-based HVDC is the more modern of the two systems and is one of the potential HVDC arrangements for future of electricity transmission in Africa; hence VSC-based HVDC is the focus in this research.

One of the key issues regarding the technical performance of any power system is its ability to return to equilibrium within the shortest possible time after it has suffered a disturbance, simply phrased as stability. Power system stability can be categorised into three groups: frequency stability; voltage stability; and rotor angle stability. Rotor angle stability is the ability of interconnected synchronous machines to remain in synchronism after being subjected to a disturbance. Subject to the magnitude of this disturbance, rotor angle stability can be categorized into transient stability and rotor angle stability. Transient stability is the ability of machines to maintain synchronism after being subjected to a severe disturbance, for instance, a short circuit on a transmission line. Small signal stability, on the other hand, is the ability of interconnected machines in a power system to maintain synchronism after a small disturbance, such as changes in the load.

Small signal stability is an important aspect to consider in the design and implementation of an HVDC network. The HVDC system controllers are the heart of the system and hence it is vital to establish how they, and other system components, interact and affect the entire system dynamics. Small signal stability analysis of the HVDC network can aid in the optimization of the VSC controllers to maintain system stability. In addition, if distributed renewable energy sources are introduced into any system, it is also important to know how they would affect the stability of the system; HVDC and distributed generation are both components of a modern system.

Power oscillation damping controllers may be either generator based or Flexible Alternating Current Transmission System (FACTS) based. Power System Stabilizers (PSS), installed in the excitation systems of synchronous generators, have been the most commonly used method for improving the small signal stability of a power system. They are the classical approach to improving the damping of electromechanical modes of oscillation. However, the complexity of modern day power systems has seen the emergence of several FACTS-based controllers such as Thyristor Controlled Series Capacitors (TCSCs). These are employed to improve damping of existing weak modes within the power system. Power System Stabilizers do not always yield adequate damping at certain operating conditions or disturbances, therefore other effective alternatives are sometimes required in place of, or in conjunction with, the PSS. These are most effective when connected in series with the AC network. In addition to oscillation damping, TCSCs can also be used for power flow control, mitigation of sub-synchronous resonance (SSR), and improvement of the system transient stability.

1.2 PROBLEM STATEMENT

The contextualization of this project is the Caprivi Link Interconnector. The system is currently functioning as a monopole, though provision was made for it to function as a bipole in the future, when the need arises. Currently, the Caprivi Link Interconnector is underutilized, transmitting

only 100-150MW of the 300MW that it was built to transmit in its monopole state; but due to generation constraints on the Zambian side, it does not function at its full capacity. One way to increase transmission capacity of the link is to incorporate renewable energy sources such as wind energy.

A few system studies have been carried out on the Caprivi Link Interconnector, such as [3]. They focused on the harmonic interaction between weak AC systems and VSC-based HVDC systems, specifically looking at this link. Other researchers looked at VSC-HVDC system performance issues such as steady-state and dynamic system modelling [4], transient stability [5], and steady-state losses [6]. There have not been any studies done on the small signal stability of this system. There is a gap in the grid codes because they do not include the small stability requirements of HVDC systems when renewable energy is considered.

1.3 KEY RESEARCH QUESTIONS

This investigation was aimed at answering the following research questions:

- What is the impact on the small signal stability of a VSC based HVDC system that incorporates an onshore wind farm?
- What are the effects of different network conditions on the small signal stability of a VSC-based HVDC system?
- How does a Power System Stabilizer compare with a Thyristor Controlled Series Compensator in terms of improving the damping of a VSC-based HVDC system with onshore wind generation?

1.4 AIMS AND OBJECTIVES

In order to address the research questions, this research has the following aims and objectives:

- To establish a test system based on the contextualization of the Caprivi Link Interconnector, to be used for the small signal stability analysis.
- To establish what types of modes are present in a VSC-based HVDC system with onshore wind generation.
- To investigate the effect of the following conditions on the small signal stability of a VSC-based HVDC system:
 - **Short Circuit Ratio (SCR):** The interaction of AC and DC systems can be measured by the strength of an AC system with regards to the DC system. The strength of an AC system has a substantial impact on the behaviour of the VSC-HVDC system and therefore it is important to know the extent of this impact.

- **Controller Parameters:** VSCs are very fast responding power electronic devices. As a result, their control parameters must be suitably selected such that the stability of the system is improved [7]. For this research, inner and outer current controller gains are the controller parameters that are being investigated
- **Wind power generation level:** Being very intermittent in nature, it is important to investigate how the constantly changing wind power generation affects the stability of the system
- To provide remedies for improving the damping electromechanical modes of a VSC-based HVDC network with onshore wind generation by designing a Power System Stabilizer (PSS) as well as a Thyristor Controlled Series Compensator (TCSC)

1.5 METHODOLOGY

1.5.1 Simulation Tool

This research is a theoretical investigation based on simulations. DIgSILENT PowerFactory is the choice of software used in this work. This is a power system simulation package that provides high definition power system modelling and analysis over a wide range of a networks including HVDC networks. DIgSILENT PowerFactory is capable of Load Flow Analysis which is necessary to determine the steady-state conditions of a network [8].

DIgSILENT has a simulation function termed the RMS Simulation which is a time domain simulation for stability analysis, and offers transient events within its environment. This simulation tool can be used to analyse mid-term and long-term transients under both balanced and unbalanced conditions. The software integrates tools for electromagnetic transient (EMT) simulations of instantaneous values with those of electromechanical simulations of RMS values. These make the models suitable for investigations of transient operation, control problems and long term power quality.

DIgSILENT has a widespread library of models of different electrical power systems components. This library comprises of models of motors, generators, controllers, dynamic loads and several passive network components, such as transformers, lines, static loads and shunts.

1.5.2 Research Process

To achieve the set objectives, the research was divided into five phases that were followed systematically. These phases are outlined as:

Phase 1: A thorough literature review was done to establish a wide understanding of VSC-HVDC transmission.

Phase 2: The network used in the study was designed and implemented in DIgSILENT and tested in order to validate it, using step response tests to verify that it had been well implemented.

Phase 3: The parameters and conditions of focus were then clearly defined according to what is considered significant for stability studies of VSC-HVDC systems.

Phase 4: Simulation under the different conditions (change in SCR, inner and outer controller gain, varying wind speed) was performed using the procedure in Figure 1-1.

Phase 5: Results of the simulations were obtained and compared, analysing the effects of the different conditions on small signal stability of the VSC-HVDC system.

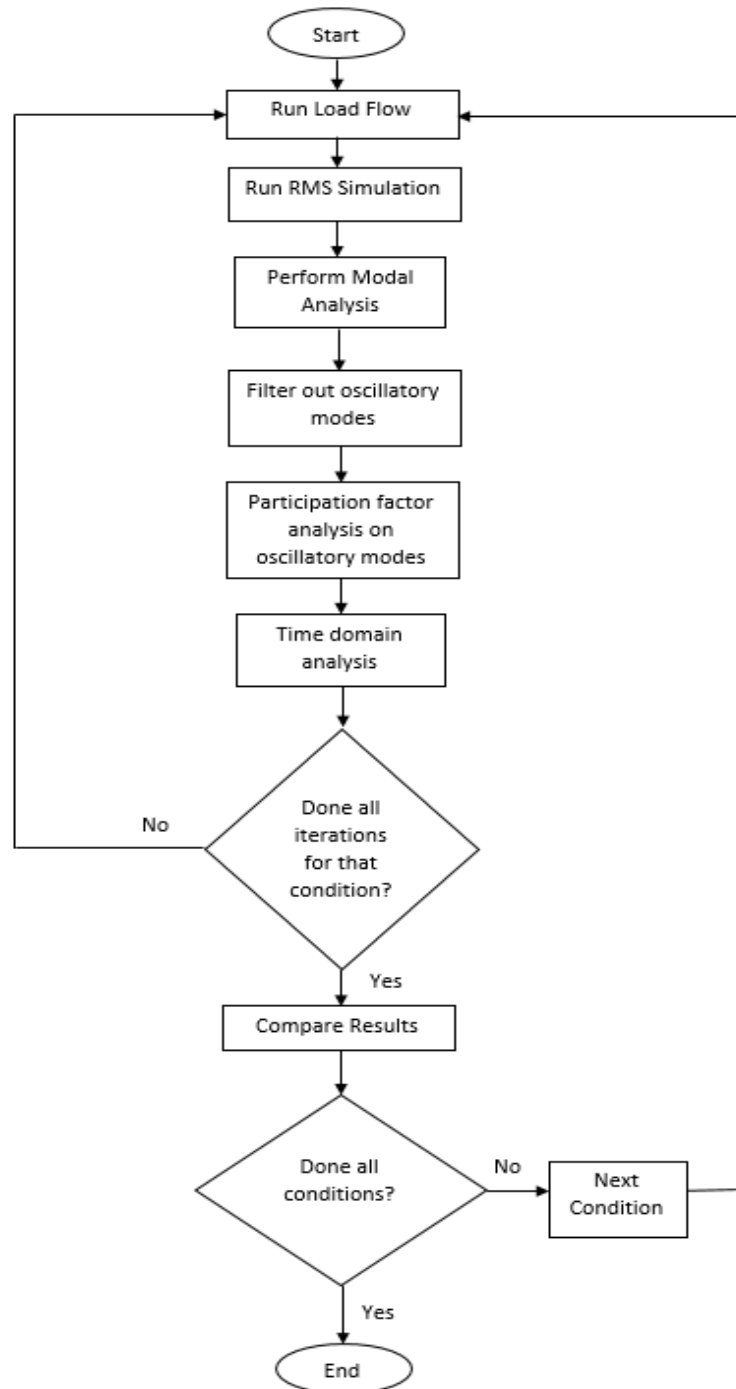


Figure 1-1 Simulation Process

1.6 SCOPE AND LIMITATIONS

The design of the base system used the Caprivi Link Interconnector (CLI) system specification, although confidentiality issues means there is inadequate information available for designing the controllers as they are in the CLI. Therefore, the controllers that are implemented do not entirely match the existing ones. All other parameters, as given in Chapter 3, are designed and calculated from the actual link parameters.

1.7 SIGNIFICANCE OF THE STUDY AND PROJECT CONTRIBUTION

This investigation is a contribution to the establishment of grid codes for the small stability requirements for VSC-HVDC systems that include renewable energy systems. The project also provides a better understanding of the modes that are most likely encountered in such systems as well as ways to improve the damping of these modes.

The research will provide an insight to industry such as the Namibia Power Corporation (NAMPOWER) when they consider implementing the Caprivi Link Interconnector as a bipole and how wind energy could potentially affect the system. It will also provide insight on what planning engineers must consider when designing VSC controllers in terms of how they affect the small signal stability of a VSC-based HVDC system with integrated renewable energy.

1.8 OUTLINE OF THESIS

Chapter 2 gives an overview of the evolution of power systems and briefly compares the merits and demerits of AC and DC transmission. It then goes on to discuss HVDC transmission, highlighting its main advantages over HVAC. There is explanation of the topologies as well as converters employed in HVDC transmission. The chapter goes on to give illustrations of existing HVDC systems around the world, and highlights the different aspects of the control structure that can be used by VSCs. The concept of wind energy generation is introduced, highlighting the different parts of a wind turbine and their functions, and giving the different types of wind turbine. Lastly, the concept of power system stability is explained, focusing on rotor angle stability and further discussion about aspects of small signal stability.

Chapter 3 covers the sizing and mathematical modelling of the equipment, parameters and the components used in this research. Calculations are performed to establish the HVDC parameters used in the simulations. The modelling of VSC controllers and wind components is illustrated here.

Chapter 4 presents the base network model used in this dissertation which consists of two areas interconnected through the HVDC transmission based on the VSC. This base network model is built and validated using DIgSILENT PowerFactory. This chapter presents the validation results of the VSC controllers and goes on to present the small signal stability of the base network to identify the modes initially present.

Chapter 5 highlights the results obtained from simulations of the monopole and bipole systems with the incorporation of an onshore wind farm as an auxiliary supply to the VSC-HVDC link. The chapter provides a comparison between the bipole and monopole systems in terms of their small signal stability under the different conditions. The latter section of the chapter looks at the

design of a PSS as well as a TCSC for both wind integrated monopole and the bipole configuration. The performance of the two power oscillation damping controllers are compared in these two configurations.

Chapter 6 gives a summary on the main conclusions drawn from the simulations, results and analyses, and provides recommendations for future research in this area.

2 LITERATURE REVIEW

This chapter gives an overview of the evolution of power systems and briefly compares the merits and demerits of AC and DC transmission. It then goes on to give detailed explanations of HVDC transmission, highlighting its main advantages over HVAC. Descriptions of the types of topology as well as converter employed in HVDC transmission are given. The chapter goes on to give illustrations of existing HVDC systems in the world, and highlight the different aspects of the control structures that can be used by VSCs. The concept of wind energy generation is introduced, highlighting the different parts of a wind turbine and their functions and describing the different types of wind turbine. Lastly, the concept of power system stability is explained, focusing on rotor angle stability and detailing the different aspects of small signal stability.

2.1 THE EVOLUTION OF POWER SYSTEMS

It was in the late 19th century that major breakthroughs were made in electrical power systems, with several inventions and experiments by scientists and inventors such as Benjamin Franklin, Thomas Edison, and Nicola Tesla. The earliest electrical system was developed by Thomas Edison in 1882 [9, 10]. This system supplied Direct Current (DC) at 110 V to a site with a radius of about 1.6 km [11]. It was formed from DC generators run by steam engines. In the late 1880s Alternating Current (AC) systems were developed, and these offered advantages over DC systems. The DC system could only deliver electricity short distances from the generator [12] and mostly was used for electric lighting. AC systems were strengthened by the discovery of the induction motor by Nicola Tesla in 1880 and the emergence of the transformer. This allowed the transformation of voltage levels for generation, transmission and distribution, and the transmission of electrical power over much longer distance. It is for these reasons that AC has become standard for electrical power systems. However, for long distance transmission, AC can still have issues related to voltage regulation and losses due to line impedance and AC resistance in the line. Travelling waves appear on long lines. DC transmission has economic, technical, and environmental advantages [13]; this was developed in the late 20th century. Mercury arc valves are high power switching devices and were developed in the 1950s [12]. Later, thyristors were developed, and these types of devices allow high voltage and high power rectifiers and inverters to be developed which enables HVDC transmission within a HVAC system.

2.2 HVAC AND HVDC TRANSMISSION

It is essential that power is transmitted at high voltage order to minimize power losses and minimize conductor size. If a constant amount of power is being transmitted, a higher voltage means the current flowing through the conductors is lower, hence reducing copper losses and conductor cross-section. Skin effect restricts the size of a conductor in an AC system and the AC

resistance can be substantially higher than the DC resistance. Line impedance will also lead to regulation issues, particularly under water since water is a good dielectric. Transmission can be done via an HVAC line or alternatively by an HVDC line where circumstances make it advantageous, such as for very long lines or underwater. Although conventional HVAC is more straightforward and normally more cost effective, HVDC transmission has become more attractive with the emergence of the thyristor valve converter which were first installed in 1972.

2.3 ADVANTAGES OF HVDC

- It is fast, easily controllable and more efficient than HVAC if the transmission line is above 500 km for overhead transmission or 50 km for underground cables.
- HVDC can also be used to transmit power between two weak or asynchronous networks [14-16].
- HVDC has less environmental impact; the pylons are smaller and have fewer conductors.
- HVDC can be used for under water cable transmission over 50 km whereas HVAC is not feasible due to high line capacitance and need for compensation.

2.4 HVDC CONVERTERS

There are several different types of HVDC converters. There are converters based on the principle of switch mode operation of a semiconductor device, either a valve type device or transistor device. The valve device is the thyristor which is a device with a gate which is pulsed and turns on. Once conducting it stays on until the current is extinguished either naturally or using forced commutation methods. These can be very high-power devices. To aid commutation, the gate turn-off thyristor was developed (GTO) which has a gate that can also be negatively pulsed to switch it off. This is again a high-power device. These are used in Line Commutated Converters (LCCs) or Current Source Converters (CSC) [17]. These converters can transmit gigawatts of power. However, they are relatively slow switching and are used in phase angle control strategies. Further developments in modern power electronics [18] have produced semiconductor devices that are hybrids of the MOSFET and bipolar device [19]. This type of device is called the Insulated Gate Bipolar Transistor (IGBT) [20, 21] and there are several other derivatives of this device. Their switching speed is somewhat faster than the thyristor; this allows pulse width modulation (PWM) switching strategies to be used and the device to be utilised in a Voltage Source Converter (VSC). The appearance of IGBTs in 1997 [22, 23] brought a more controllable option than the thyristor-based converter, giving the VSC-HVDC system an increased level of flexibility, and easy adaptability for transmission of power from renewable power resources such as wind generation farms [24]. The power range of the VSC-HVDC system is still only several tens or a very few hundred of megawatts but they are very suitable for a transmission link for

transmitting renewable energy such as wind power [2, 25]. Table 2-1, as highlighted in [26], lists the differences between the two converter technologies. The issue with the LCC is that it has a low number of voltage steps, possibly as low as 6 steps for a single bridge or 12 steps for a two-bridge arrangement, so that much filtering is required which affects power quality. The VSC uses PWM and requires much lower filtering, but the power is more limited. To allow for lower filtering at high power transmission levels the modular multilevel converter (MMC) has been developed and is now being deployed as an option.

Table 2-1 Comparison of LCC and VSC

LCC	VSC
Employs thyristors as switches	Employs IGBTs as switches
Current only flows in one direction	Current can flow in either direction
Turned on by a gate pulse but relies on external circuit for its turn off unless GTO is used	Both turn on and off is carried out without the help of an external circuit
High power capacity	Lower power capability
Good at handling overload states	Weak at handling overload states
Functions best in strong AC systems	Functions well in weak AC systems
Additional equipment is needed for black start action	Capable of black start action
Requires AC and DC harmonics filters for removal of distortion harmonics	Requires no filter because it generates an insignificant level of harmonics
Poor in control of reactive power	Good control of reactive power
Large footprint due to harmonic filters	More compact footprint
Requires converter transformer	Employs conventional transformer
Incurs lower power losses	Incurs higher power losses
More mature technology	Still at its infancy
Higher voltage capability of over ± 550 kV	Lower voltage capability - about 350 kV
Mainly used to transmit bulk power for long distance	Used for transmitting power from remote area with renewable energy
Suffers commutation failures, therefore not suitable for use in multi-terminal HVDC systems	Does not suffer commutation failure therefore suitable for multi-terminal HVDC systems

2.5 HVDC TOPOLOGIES

HVDC network topologies are typically classed as back-to-back, monopole, bipole or multi-terminal. The back-to-back topology comprises of two converter stations situated near one another; i.e., at the same site or building. In this configuration, an overhead or underwater HVDC transmission line is not employed. This means that there is no need to have a return via earth as illustrated in Figure 2-1 for and this means that they will tend to be in a monopole configuration as shown.

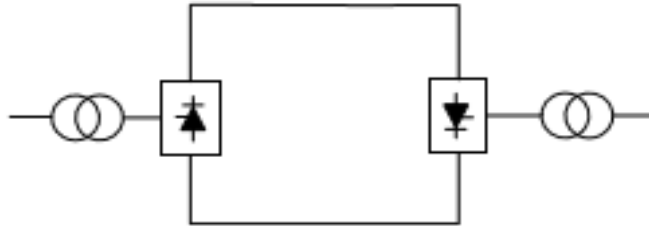


Figure 2-1 Monopole back-to-back HVDC Configuration [21]

The monopole configuration when used for distance transmission is a two terminal DC network consisting of two converters on each end of a positive or negative DC transmission line, with one of the lines connected via an earth line. This is shown in Fig. 2-2 for a positive DC line and an LCC converter. It is advantageous to have a ground return although not all HVDC systems have such a system. The Basslink in Australia links Victoria and Tasmania. It is a 400 kV 500 kW sub-sea system with both go and return via cabling. It transmits from Tasmania to Victoria utilizes LCC technology. This is called a symmetric monopole.

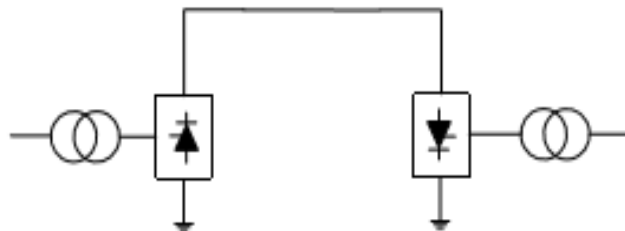


Figure 2-2 Monopolar configuration [21]

The bipolar topology employs two conductors at negative and positive potential both relative to ground. With a centre-point earth then the systems should be able to transmit independently on each line and this is the case with the Cahora Bassa HVDC link. This arrangement is shown in Figure 2-3.

The final topology is known as a multi-terminal direct current (MTDC) system. This configuration includes more than two converters connected to one another in series or in parallel. Parallel configuration is further characterised as either meshed or radial configuration.

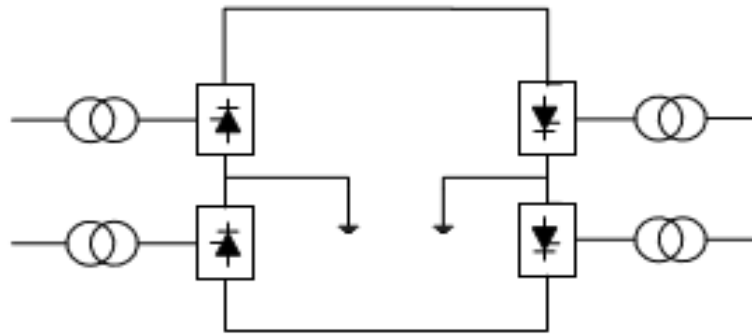


Figure 2-3 Bipolar configuration [21]

Many HVDC links currently implemented are of those connected between two points of an AC system or links aiding the interconnection of two different AC systems. These are often referred to as point-to-point links. There are also several MTDC links; for example, the Quebec New England link as well as the Sardinia Corsica Italy link. These links function with the power being transmitted from a generation station via the DC link to the main load centre with an additional or intermediate load centre within its path [27], thus forming a series multi-terminal configuration. The reason for opting for a MTDC grid over a point-to-point DC link lies with the benefits it offers in the integrated operation with a power system which is capable of fulfilling the requirement to ensure that electricity generation equals the demand while taking into consideration the security, reliability, quality, and cost efficiency of the system [28-31]. The key benefits offered by MTDCs in comparison with the point-to-point links are explained in [27].

2.6 EXISTING PROJECTS IN HVDC

2.6.1 Gotland HVDC Link

The world's first HVDC system that was commercialised was built between the island of Gotland and Sweden in 1954 [32]. This project, called Gotland 1, could only transmit 20 MW over a 98 km underwater cable [33]. This was the beginning of DC transmission in AC power systems. This system used mercury valves. This project was upgraded in 1999 to transmit 50 MW at 80 kV DC using two 70 km underwater cables.

2.6.2 Sardinia-Corsica-Italy

This HVDC system started out as a two terminal link between Sardinia and Italy [34, 35] rated at 200 MW, 200 kV, and it was built in 1967. Successful implementation of this phase of the project led to the expansion of the link into a multi-terminal HVDC system in 1991 which included a 50 MW tapping from Corsica. This system went from being a point-to-point HVDC link to a radial parallel multi-terminal link, making it the first ever multi-terminal HVDC connection. This is illustrated in Figure 2-4.



Figure 2-4 Sardinia-Corsica-Italy Interconnection [16]

2.6.3 Hydro Quebec-New England Interconnection

This is another notable system that started as a point-to-point HVDC link, commissioned in 1990, and later expanded to a multi-terminal HVDC system in 1992 [36]. The first phase of this project was a two-terminal bipolar link rated 690 MW. The second phase of the project involved the expansion of this link by the addition of three more converter stations of the ratings 1800 MW, 2138 MW and 2250 MW [22]. This is shown in Figure 2-5.



Figure 2-5 Hydro Quebec New England Interconnection [16]

These latter two projects both use LCC technology; very few multi-terminal VSC based system have been implemented. However, there are several noteworthy two terminal VSC based HVDC projects in the world.

2.6.4 Caprivi-Link Interconnector

The Caprivi Link Interconnector, in Namibia, is presently the only VSC-based HVDC system in Africa and it is the first in the world that uses overhead transmission. It is illustrated in Figure 2-6. The link is a point-to-point system and is a vital connection in the Southern African Power Pool (SAPP) [27, 37]. It interconnects two weak asynchronous AC networks: the Namibian and Zambian AC systems. The HVDC link is a 952 km bipole 350 kV HVDC transmission line [38] of 300 MW capacity. It has been built to be able to be upgraded to 600 MW at full capacity [39]. The project incorporates ABB light HVDC technology which employs IGBTs.

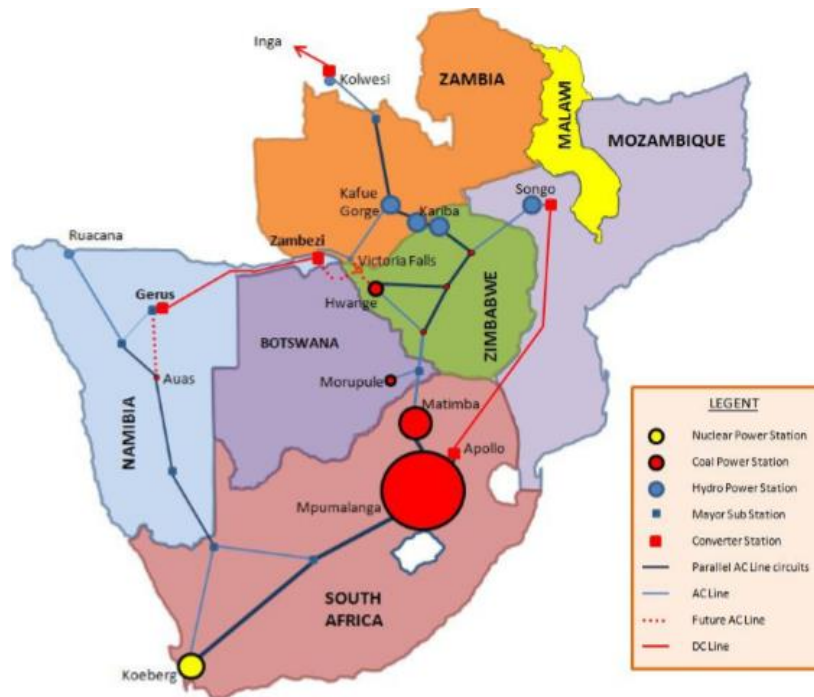


Figure 2-6 Caprivi Link Interconnector [35]

Active power can be up to 300 MW of imported power, and 350 MW overload at low temperature, or from 0 to 280 MW of exported power, without disruption in the flow of power [27]. The link is capable of AC voltage control which works in concurrence with the nuclear control of active power [40]. Reactive power control is only active when selected instead of AC voltage control. When selected, the reactive power exchange is maintained as a constant. The link is capable of frequency control as well as power limit control during islanded network conditions.

Other existing HVDC projects are highlighted in Table 2-2.

Table 2-2 Summary of other existing HVDC Projects around the world [41, 42]

Project	Power Rating [MW]	Distance [km]	Year of Commissioning
Tjaereborg, Denmark	7.2	4.3	2000
Eagle Pass, USA	36	Back-to-back	2000
Direct Link, Australia	180	59	2000
Murray Link, Australia	220	180	2002
Troll, Norway	84	70	2005
Estlink, Estonia Finland	350	105	2006
Valhall, Norway	78	292	2009

2.7 CONTROL OF VSC-HVDC

VSCs operate by means of high frequency pulse width modulation (PWM). This means that they possess the ability to independently control both reactive and active power [43], therefore keeping the voltage and frequency stable [41]. Satisfactory performance of VSC-HVDC system under diverse operating conditions is dependent on the choice of robust parameters for the control scheme [44-47]. Due to their robustness and simple structure, PI controllers are frequently chosen for adjusting the network conditions for desired responses [48]. With regards to point to point VSC-HVDC link, one converter station regulates the DC link voltage, while the other regulates active power. Each converter is able to autonomously regulate either AC side voltage or the reactive power. There are different control schemes for VSC-HVDC, mainly grouped as either direct control and vector oriented control [49].

2.7.1 Direct Control

The direct control strategy deals with the AC voltages and currents of the converter directly in the three phase (*abc*) frame and do not need any transformation as in the case of vector control. This control strategy is not complex and the references for current are considered by establishing them from the load flow calculations between two points [50]. Regardless of its simplicity, this method of control possesses several shortcomings such as the need for fast conversion and computation, as well as switching frequency. This type of control method is very seldom used [51], attributed mainly due to the fact that it is unable to limit the converter current, which is an essential necessity since VSC-HVDC converters do not offer over current protection [52, 53]. There are no internal current control loops with this control method neither is there any pulse width modulation. The switching states are selected by switching tables that implement virtual

flux vector in its control loop. Other shortcomings such as variable switching frequency the need for fast computation and conversion leaves much to be desired for and hence is not very commonly used.

2.7.2 Vector Oriented Control

The most commonly implemented VSC-HVDC method of control is the vector oriented control scheme which provides a nested loop structure consisting of a faster inner current loop and a slower outer control loop which generates d and q axis current references to the current loop controller [54]. The selection between various types of controllers to compute the converter current reference values is determined by the specific application [55]. This is shown in Figure 2-7.

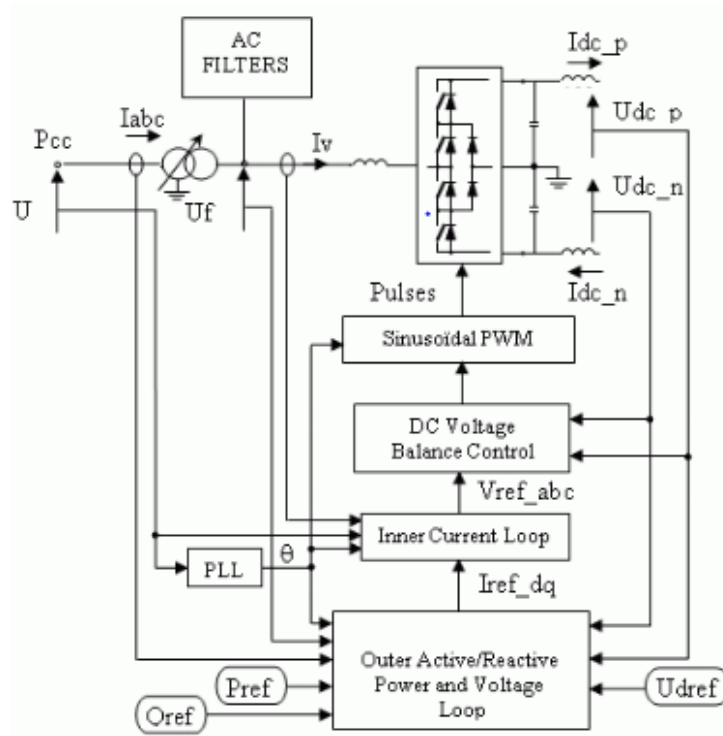


Figure 2-7 VSC-HVDC Overview [50]

To discuss specific components of the system in Figure 2-7:

Phase Lock Loop: The Phase Locked Loop (PLL) measures the frequency of the system and gives the synchronous angle of the phase, which is needed for dq transformation [56, 57].

Inner Current Control Loop: This controller is responsible for generating reference voltage signals which are compared with the high frequency carrier signal of the PWM. This generates the gating signals required to turn the IGBT switches on and off. Switches in the same leg of the converter operate in a complementary manner. Switching of a complementary pair simultaneously forms a short circuit across the DC link which will lead to catastrophic damage

to the converter switches as a result of short-circuit over current [58]. This inner current loop control is shown in Figure 2-8.

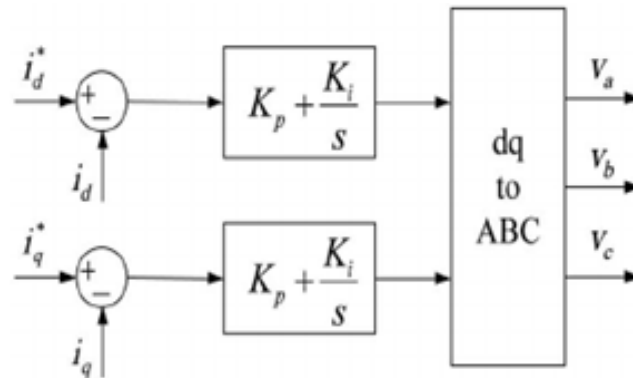


Figure 2-8 Inner Current Control Loop

Outer Control Loop: This loop controls the DC voltage, reactive and active power by means of PI controllers which determine the converter current vector reference values. These serve as the inputs to the inner current controller. The reference value for active (d-axis) current is taken from either the active power controller or the DC voltage controller. The reference value for reactive (q-axis) current is acquired from the reactive power controller or the AC voltage controller. The different outer controllers are looked at more in depth in Chapter 3 and can refer to Figures 3-6, 3-7 and 3-8.

2.8 WIND ENERGY SYSTEMS

An increasing deployment of wind turbines has taken place over the last two decades. The generation of wind power is currently approximately 487 GW, after 55MW was added in 2016. It is predicted to go beyond 760 GW by 2020, making this form of renewable energy a significant element in modern power systems.

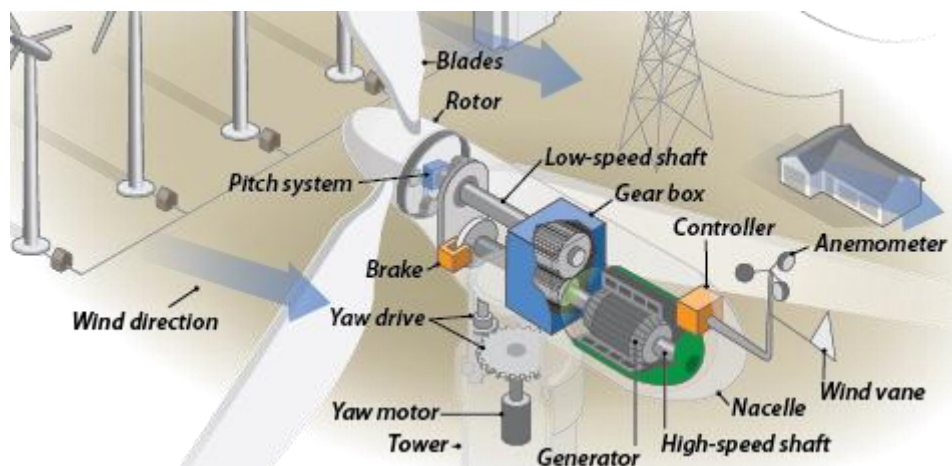


Figure 2-9 Parts of a wind turbine [59]

2.8.1 Components of a Wind Turbine

The different parts and characteristics of a wind turbine are shown in Figure 2-9 and together they serve the following functions [59]:

Anemometer: Captures the wind speed data and conveys this to the controller.

Blades: Spins the rotor as a result of the wind rotating them.

Brake: Bring the rotor to a standstill in emergencies.

Gear box: Raises the rotational speed to a value appropriate for the generator to produce electricity.

Generator: Generates AC electricity either at variable frequency or fixed frequency.

High speed shaft: Connects the high speed side of the gearbox to the generator.

Low speed shaft: Connects the hub and blades to the low speed side of the gearbox.

Nacelle: Is situated above the tower and encompasses the gearbox, low speed shaft, high speed shaft, brake, controller and generator.

Pitch: Prevents the rotor from rotating in very high or very low winds that are not viable or safe to produce electricity.

Tower: The higher the tower, the more wind energy is available due to increased wind speed, thus more electricity can be generated.

Wind vane: Finds the wind direction and controls the yaw drive to position the turbine depending on the wind direction.

Yaw drive: Angles upwind turbines to a position that allows them to face the wind as the direction changes. In the case of downwind turbines, the wind manually blows the rotor away from it and therefore these do not need a yaw drive.

Yaw motor: Energises the yaw drive.

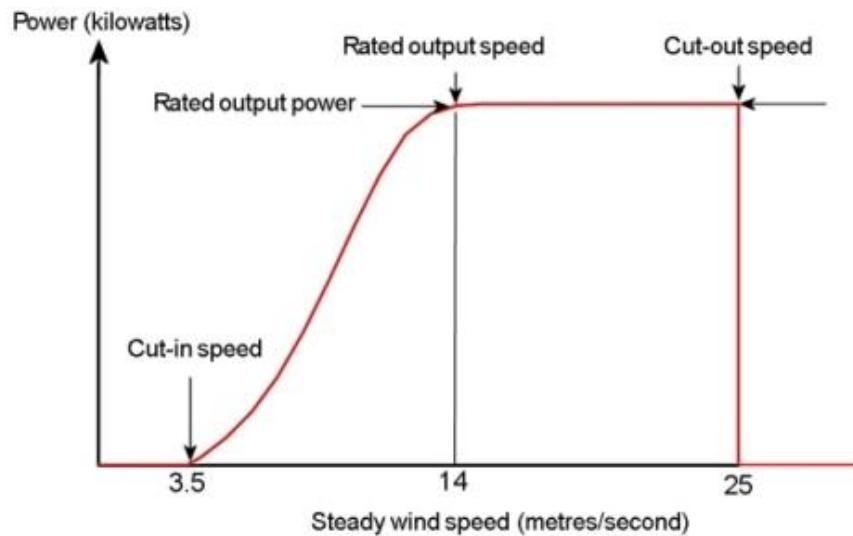


Figure 2-10 Wind turbine speed characteristics [60]

A typical power/wind speed characteristic is given in Figure 2-10. This will vary depending on the type of wind turbine. There are variable and fixed speed turbines; fixed speed turbines are controlled via the blade pitch and use a grid-connected cage induction generator, for variable speed turbines the following points can be made.

Cut-in speed: At lower wind speeds, there is not enough torque generated to allow rotation and generation. The wind turbine only starts rotating as the wind speed increases, and thus generates electricity. The cut-in speed, which is usually in the range of 3-4 m/s, is the speed when the turbine begins rotating and generating electricity.

Rated output power and wind speed: When the wind speed increases beyond the cut-in speed, the output power increases. Within the range of approximately 12-17 m/s, the output power reaches its limit. The rated power output is limit of the generator and turbine and above this rated power wind speed the turbine will run at constant speed and power with control via the pitch of the blades. The turbine will begin to shut down when the cut out speed is reached.

Cut out speed: When the wind reaches a certain level which is typically 25 m/s the turbine will cut out with the blades pitched away from the from the wind and the turbine can coast down. This is essentially storm protection.

2.9 TYPES OF WIND TURBINES

Onshore wind power generation is the most cost effective solution for new grid based power in a number of markets [61]. Wind turbines can be classified into four categories [62]:

2.9.1 Fixed Speed Wind Turbines

This system is typically accompanied by a multiple stage gearbox and a squirrel cage induction generator with a three bladed rotor [63]. The generator is connected to the grid using a transformer

[64]. This configuration operates slightly above the synchronous speed, where the induction machine operates in generator mode, the operating slip range will be from 0 to about -4 % slip to maintain reasonable efficiency [63]. A typical system is shown in Figure 2-11.

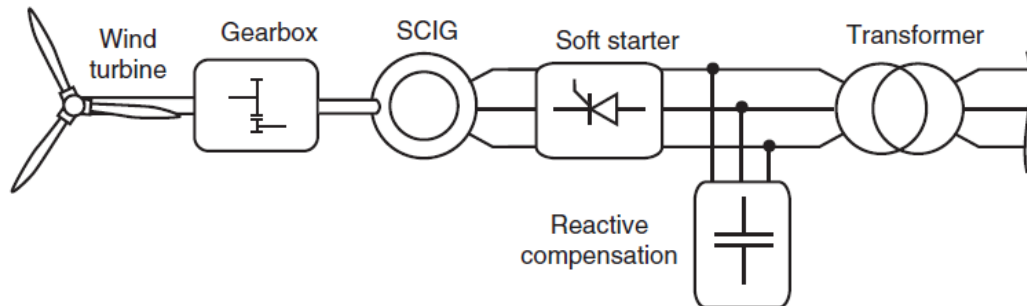


Figure 2-11 Fixed Speed Wind Energy System [63]

This type of wind turbine system, although simple, reliable and lower in cost, has disadvantages such as reactive power burden on power grid, high mechanical stress, power fluctuations and limited fault-ride-through capability [65]. They are good in locations where the wind resource is steady and of good quality such as the west coast of Ireland.

2.9.2 Limited Variable-Speed Wind Turbines

This type employs the wound rotor induction generator (WRIG). This system is a derivative of induction machine slip energy recovery. An effective variable external rotor resistance is used to increase the speed above the synchronous speed; the operating range is increased up to possibly - 10 % p.u. slip and maybe even higher. The slip of the machine is changed by altering the rotor resistances by means of a power electronic converter as illustrated Figure 2-12. Attaining this level of control incurs power loss in the rotor resistances. This partially solves the requirement for variable speed operation to improve the aerodynamic efficiency; however, this system shares similar drawbacks with the fixed speed wind turbine and the speed range is still limited.

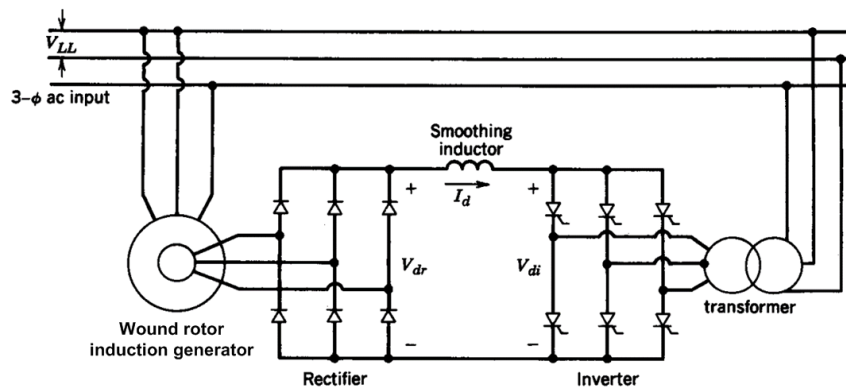


Figure 2-12 Limited Speed Variable Speed Wind Energy System

2.9.3 Partial-Scale Converter Variable Speed Wind Turbines

This wind energy system configuration is a common solution and has been extensively deployed since it appeared in 2000 [66]. This system again uses a wound rotor induction generator in the form of a Doubly Fed Induction Generator (DFIG). The rotor is connected to the grid via back-to-back VSCs which allows bi-directional power flow as well as voltage and reactive power control in the rotor. This system offers a variable speed controlled wind turbine with a wound rotor induction generator and partial scale power converter rated in the region of 30 % of nominal generator power [67]. The system can generate sub-synchronously as well as super-synchronously and operates between per-unit slips of about 0.3 to -0.3.

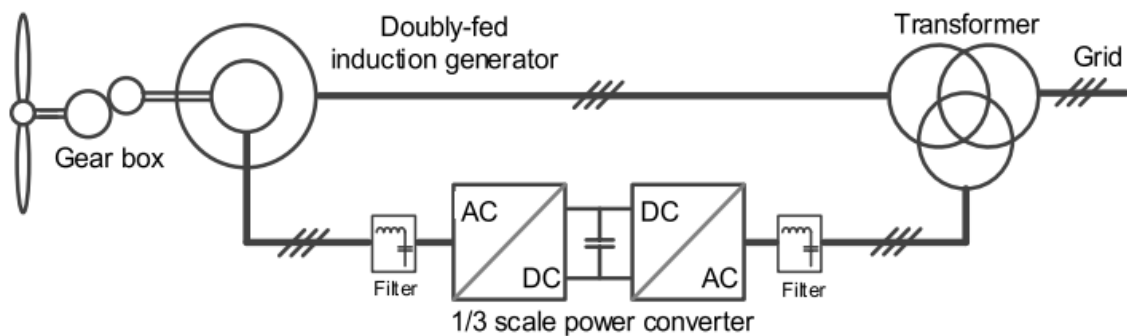


Figure 2-13 Double Fed Induction Generator (DFIG) Configuration [66]

The partial scale converter provides the system with good integration to the grid. The grid side, which is operated separately from the generator side, is able to be controlled to attain an improved voltage support as well as better fault ride-through capability [68]. A noteworthy shortcoming of DFIGs is that they are sensitive to voltage drop and so if a fault occurs in the system, the DFIG terminal voltage drops. The rotor current then increases which may cause damage to the converters.

2.9.4 Full Scale Converter Variable Speed Wind Turbines

This variable speed configuration employs a full-scale converter. It uses an AC generator and the speed and power ranges are wide. The frequency converter carries out the reactive power compensation and ensures a smooth link to the grid [67]. The DC link usually encompasses a DC chopper to stabilize the DC link voltage. This configuration can be employed for different types of generators such as Permanent Magnet Synchronous Generators (PMSGs), Squirrel Cage Induction Generators (SCIGs), as well as Wound Rotor Synchronous Generators (WRSGs) [66].

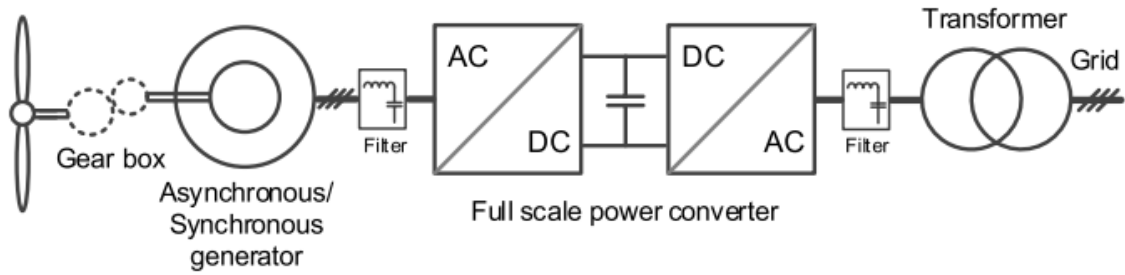


Figure 2-14 Full Scale Power Wind Energy System [66]

In comparison to the DFIG, the key benefits of this type include the exclusion of slip rings. DFIGs are low pole number machines; however, PMSGs and WRSGs can have many more poles so that they can run at a much lower speed. Therefore, the gearbox either has a lower speed ratio or it is omitted all together. It also offers more power and speed control, in addition to improved grid support. The disadvantage of this topology lies in that it has expensive power electronics components and higher power losses in the converter. For this reason, it not often used in wind turbines [66]. However, with the power electronics reducing in cost and the advantages in having no gearbox, they are becoming more common.

2.10 POWER SYSTEM STABILITY

This section gives insight on the concept of power system stability, highlighting it's meaning, importance in a power system as well as the different types of stability that can occur. It specifically details small signal stability.

Power system stability is the capability of the system to return to the steady-state condition within the least possible time after suffering a disturbance. It can also be defined as the ability of a power system to recover to an appropriate equilibrium after undergoing a disturbance. There are three aspects of stability: frequency stability, rotor angle stability and voltage stability. These are presented in Figure 2-15.

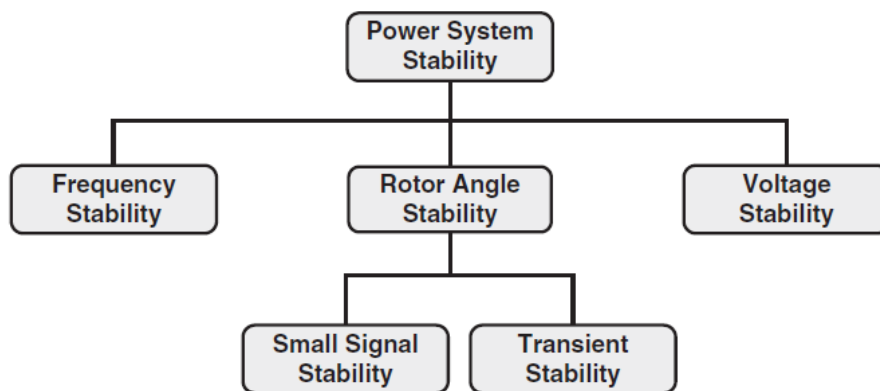


Figure 2-15 Power System Stability Classification [69]

2.11 ROTOR ANGLE STABILITY

This is when connected machines can continue to operate synchronously following a disturbance. It relies on the ability of the system to re-establish a balance between the electromagnetic and mechanical torque of the synchronous machines. The instability that may result when the balance is not met, will likely occur in the form of growing angular oscillations of the generators causing them to lose synchronism [70]. Rotor angle stability can be divided into two classes: small signal (dynamic) stability and transient stability.

2.11.1 Transient Stability

Transient stability is experienced when the power system regains equilibrium after a severe or large disturbance. These kinds of perturbations are often caused by short circuits, with three phase short circuits being the most severe. The aim of the transient stability studies is to establish whether the load angle returns to a steady value following the clearing of the disturbance.

Power system stability is heavily dependent on the relationship between the output power and the angular position of the rotor of each synchronous machine. The electrical power output of a synchronous machine is given by

$$P_e = 3 \frac{EV}{X} \sin \delta \quad [\text{p.u.}] \quad (2.1)$$

where E is the field-controlled excitation EMF of the machine, V is constant voltage of the infinite bus and δ is the angle between E and V , often called the load angle or rotor angle. The voltages are in phase per unit (p.u.) values. This is for a cylindrical machine. A salient pole machine will have a second harmonic with respect to the load angle. The voltages are synchronously-rotating voltage phasors. X is the armature reactance of the machine. It is more suitable to measure rotor angular position with respect to a synchronously rotating reference frame because the rotor angle θ_e (with respect to a stationary reference frame) changes with time through each cycle. Therefore, it is easier to use the load angle δ , given by

$$\delta = \theta_e + \omega_s t \quad (2.2)$$

where ω_s is the mechanical speed. For multiple machines, the machines will have different rotor angles with respect to the busbar depending on the prime mover power and the excitation voltage. Synchronous machines run at a constant speed. If the system is disturbed and one generator momentarily runs at a faster or slower speed than the other generator, the angular separation of their rotors will begin to change. After a specific point, this increasing angular separation is accompanied by a reduction in the transfer of power, as illustrated by Figure 2-16, therefore an increase in angular separation leading to instability.

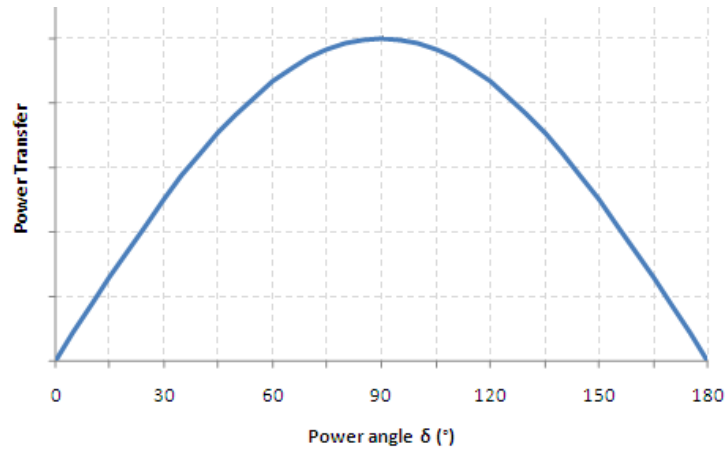


Figure 2-16 Power Angle Relationship

At steady state, mechanical input power P_m into the system is equal to the electrical output power P_e . The rotor angle dynamics come into play when there is a mismatch between electrical power output and mechanical power input. This results in an accelerating or decelerating power P_a . If the speed is considered as constant even with small-signal transient variation (which will be the case if synchronism is not lost) then there is an acceleration torque which changes the machine speed slightly depending on the generator inertia J [kgm²], so that

$$P_a = T_a \omega_s = P_e - P_m \quad [\text{W}] \quad (2.3)$$

$$T_a = J \frac{d\omega_s}{dt} = J \frac{d^2\theta_e}{dt^2} \quad [\text{Nm}] \quad (2.4)$$

If (2.2) is differentiated twice then we find that for small perturbations, P_a can be obtained as a function of δ by considering the accelerating torque, so that

$$\frac{d^2\theta_e}{dt^2} = \frac{d^2\delta}{dt^2} \quad (2.5)$$

$$T_a = J \frac{d\omega_s}{dt} = J \frac{d^2\theta_e}{dt^2} = J \frac{d^2\delta}{dt^2} \quad [\text{Nm}] \quad (2.6)$$

$$P_a = J \omega_s \frac{d\omega_s}{dt} = J \omega_s \frac{d^2\delta}{dt^2} = M \frac{d^2\delta}{dt^2} \quad [\text{W}] \quad (2.7)$$

We need to further develop this to obtain an expression in p.u. The angular momentum $M = J\omega_s$ and this is also called the inertia constant; the stored energy is

$$E_m = \frac{1}{2} J \omega_s^2 = \frac{1}{2} M \omega_s \quad [\text{J}] \quad (2.8)$$

To work in p.u. values we can introduce a normalised inertia constant H where

$$H = \frac{\text{Stored kinetic energy in joules (or MJ) at synchronous speed}}{\text{machine rating in VA (or MVA)}} \\ = \frac{\frac{1}{2} M \omega_s}{S_{\text{rated}}} \quad [\text{MJ/MVA}] \quad (2.9)$$

so that

$$P_a = M \frac{d^2 \delta}{dt^2} = S_{\text{rated}} \frac{2H}{\omega_s} \frac{d^2 \delta}{dt^2} = S_{\text{rated}} \frac{H}{\pi f} \frac{d^2 \delta}{dt^2} \quad [\text{W}] \quad (2.10)$$

where f is the frequency of rotation (equal to the supply frequency for a two-pole generator). This then becomes the swing equation:

$$P_a = P_m - P_e = \frac{H}{\pi f} \frac{d^2 \delta}{dt^2} \quad [\text{p.u.}] \quad (2.11)$$

This can be compared to (2.1) and for a small signal disturbance where $\delta = \Delta + \delta_s \sin(\omega_s t)$ it can be seen that there is the possibility of transient oscillation in the system.

Equal Area Criteria

The equal area criterion is used to evaluate the transient stability of power systems. For practical purposes, the mechanical power P_m is assumed to remain constant during electrical transients. Transient stability is gauged on whether a power system is able to recover from a large disturbance and settle to the constant power P_m with a new load angle δ . In steady-state, P_m is equal to P_e at angle δ_0 . It can be used for switching loads but here we will discuss a fault that disconnects the generator, followed by a reconnection when the fault is cleared.

When a fault occurs, the circuit breakers open therefore decreasing the electrical power P_e to zero. We assume that the mechanical power stays constant, so that the accelerating power increases to a value equivalent to the mechanical power. The difference in accelerating and mechanical power results in an increase in the kinetic energy is stored in the rotor. The rotor therefore accelerates under the impact of the accelerating power and thus the load angle increases were

$$P_a = P_m = M \frac{d\omega_s}{dt} = M \frac{d^2 \delta}{dt^2} \quad (\delta_0 \leq \delta < \delta_c) \quad [\text{W}] \quad (2.12)$$

When the circuit breakers reclose at the angle δ_c , the electrical power flows. At this instance, the electrical power becomes greater than the mechanical power since δ has increased, and accelerating power then becomes negative. This is shown in Figure 2.17. However, since more kinetic energy has been put into the rotor, it is still running at a slightly faster speed than ω_s and so δ will continue to increase while the rotor speed is faster than the synchronous speed, even

when decelerating, but δ does stop increasing at δ_m [71] when the rotor speed is equal to the synchronous speed. Then we have

$$P_a = P_m - P_e = M \frac{d\omega_s}{dt} = M \frac{d^2\delta}{dt^2} \quad (P_a < 0; \delta_c \leq \delta \leq \delta_m) \quad [\text{W}] \quad (2.13)$$

In Figure 2.17 the angles are quite large for illustration – and set at the critical value as discussed below. We can prove that the areas A_1 and A_2 have to be equal for stability. A_1 is an acceleration stage and A_2 is a deceleration stage. We can further work the expression for P_a so that

$$P_a \frac{d\delta}{dt} = M \frac{d^2\delta}{dt^2} \frac{d\delta}{dt} = \frac{M}{2} \frac{d}{dt} \left[\left(\frac{d\delta}{dt} \right)^2 \right] \quad (2.14)$$

$$\left[\text{proof: let } x = \frac{d\delta}{dt} \text{ so that } \frac{d^2\delta}{dt^2} \frac{d\delta}{dt} = \frac{dx}{dt} x = \frac{1}{dt} x dx = \frac{1}{dt} \frac{x^2}{2} = \frac{1}{2} \frac{d}{dt} \left[\left(\frac{d\delta}{dt} \right)^2 \right] \right]$$

Now integrate so we get

$$P_a d\delta = \frac{M}{2} \left(\frac{d\delta}{dt} \right)^2$$

$$\int_{\delta_c}^{\delta_m} P_a d\delta = \frac{M}{2} \left(\frac{d\delta}{dt} \right)^2$$

$$\int_{\delta_0}^{\delta_c} (P_m) d\delta + \int_{\delta_c}^{\delta_m} (P_m - P_e) d\delta = \frac{M}{2} \left(\frac{d\delta}{dt} \right)^2$$

$$A_1 - A_2 = \frac{M}{2} \left(\frac{d\delta}{dt} \right)^2 \quad (2.15)$$

For steady-state to be re-established then the load angle must stop changing so that it can then return to an equilibrium, i.e.,

$$\frac{d\delta}{dt} = 0$$

so that at

$$A_1 - A_2 = \frac{M}{2} \left(\frac{d\delta}{dt} \right)^2 = 0$$

Hence the areas have to be equal to maintain synchronism.

Closing the line at the reclose angle where the area of acceleration A_1 is greater than the area of deceleration A_2 , the load angle will go the point δ_m where the electrical power is lower than the

mechanical power, causing the accelerating power to be positive. This causes the generator to begin accelerating again so that the system becomes unstable [72].

For the example in Figure 2.17, this is a special case where $A_1 = A_2$ describes the stability limit boundary. Therefore, clearing angle δ_c is now referred to as the critical clearing angle, δ_{cr} . The critical clearing angle depends on the areas A_1 and A_2 being equal, hence the equal area criterion. The critical fault clearing time (CCT) is defined as the maximum length of time that a disturbance can be applied while the system stability is still maintained. When the rotor angle peaks and starts decreasing, then it indicates that the system has transient stability. If the rotor angle keep increasing without reaching a maximum, this indicates that the system is unstable.

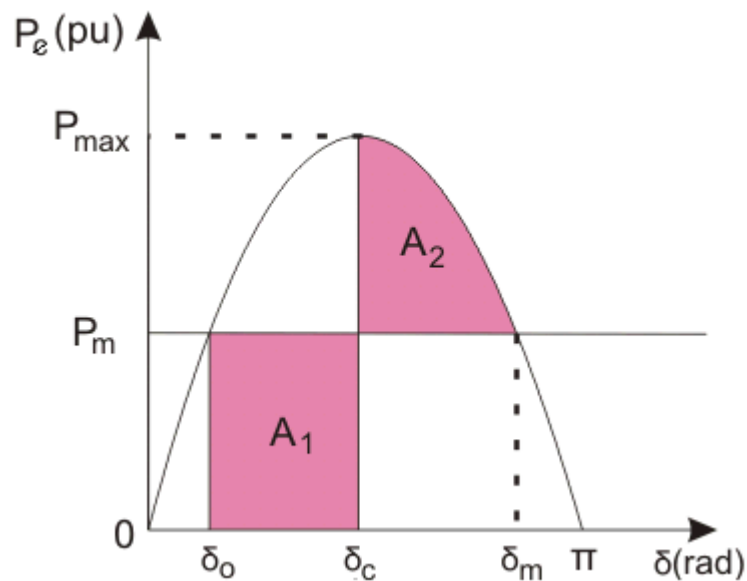


Figure 2-17 Equal Area Criterion (δ_c set to the critical value δ_{cr})

2.11.2 Small Signal Stability

Small signal stability is the capability of a power system to continue operating in synchronism after small disturbance caused by change in loads or generation. These random disturbances may lead to disastrous damage since these can force the rotor angle to increase progressively. In normal operation, these perturbations are taken as being sufficiently small that linearization of the system equations is acceptable for analysis.

Small signal stability analysis can be carried out for a certain steady-state operating condition where the non-linear differential and algebraic equations are linearized. This process produces a new set of variables for the system under disturbance. Small-signal instability arises in two ways:

- Rotor angle steadily increasing because of insufficient synchronizing torque.
- Rotor oscillations characterized by growing amplitude because of insufficient damping torque.

In practice, the latter is of more concern than the former in small-signal rotor-angle stability analysis.

The stability of a linearized system is described by the eigenvalues of the state-space matrix. The state space representation of a system is given by [73] and illustrated in Figure 2-18.

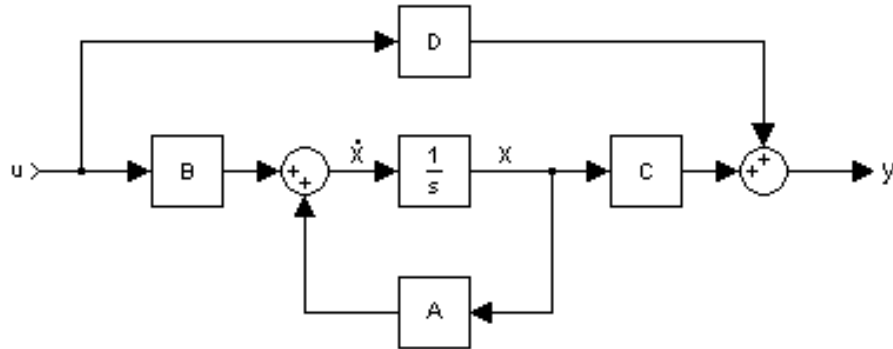


Figure 2-18 State Space representation of a system

The system can be summarised mathematically using the expressions

$$\dot{\mathbf{x}} = \mathbf{A}\mathbf{x} + \mathbf{B}\mathbf{u} \quad (2.16)$$

$$\mathbf{y} = \mathbf{C}\mathbf{x} + \mathbf{D}\mathbf{u} \quad (2.17)$$

Given that \mathbf{x} is the state vector, $\dot{\mathbf{x}}$ is the derivative of the state vector with respect to time, \mathbf{y} is the output vector, and \mathbf{u} is the input or control vector. \mathbf{A} , \mathbf{B} , \mathbf{C} and \mathbf{D} are the system, input, output and feedforward matrices respectively.

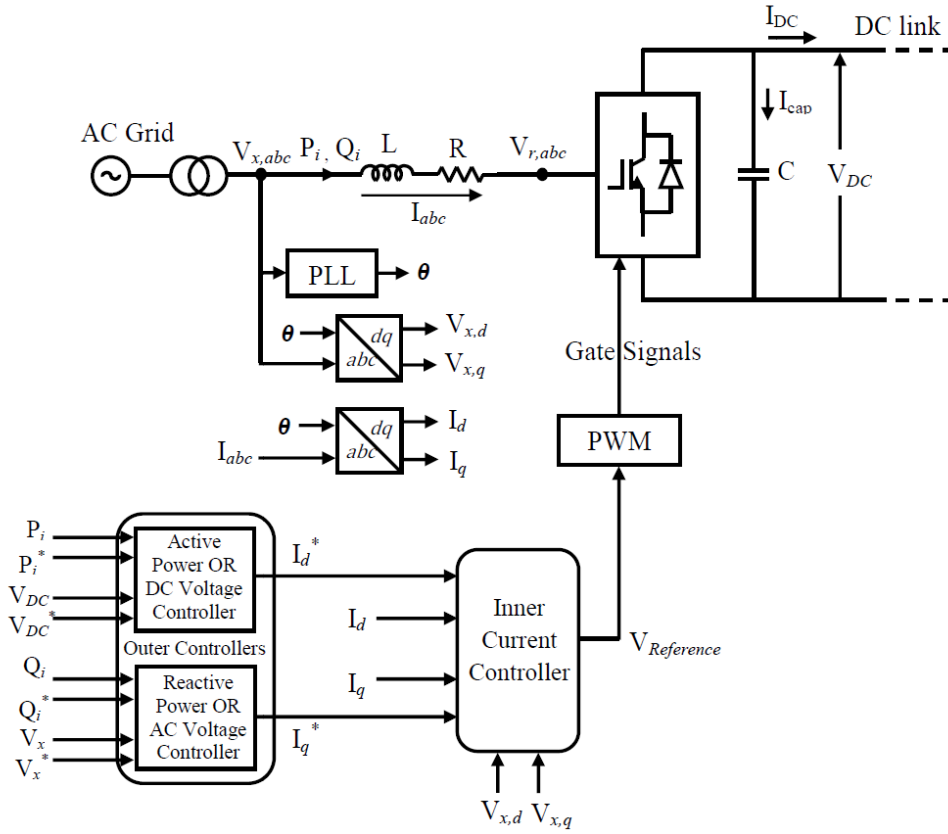


Figure 2-19 VSC-HVDC Control Structure

The system matrices can be derived through the following process illustrated in the d axis. From Figure 2-19

$$\begin{aligned}
 V_{xd} &= \frac{L di_d}{dt} + Ri_d - \omega Li_q + V_{rd} \\
 \frac{di_d}{dt} &= \frac{V_{xd} - Ri_d - V_{rd} + \omega Li_q}{L} \\
 \frac{di_d}{dt} &= -\frac{Ri_d}{L} + \frac{V_{xd} - V_{rd} + \omega Li_q}{L}
 \end{aligned} \tag{2.18}$$

where ω is the fundamental frequency of the AC network and ωLi_q is decoupling term from the controller. Letting

$$u_d = V_{xd} - V_{rd} + \omega Li_q$$

where u_d and u_q are obtained from the PI controller. Therefore

$$u_d = k_p (i_d^* - i_d) + k_i \int (i_d^* - i_d) dt \tag{2.19}$$

Letting

$$\lambda_d = k_i \int (i_d^* - i_d) dt$$

Therefore

$$\begin{aligned} \frac{\lambda_d}{dt} &= k_i (i_d^* - i_d) \\ \frac{\lambda_d}{dt} &= k_i i_d^* - k_i i_d \\ u_d &= k_p (i_d^* - i_d) + \lambda_d \end{aligned} \tag{2.20}$$

Substituting into (2.18) gives

$$\begin{aligned} \frac{di_d}{dt} &= \frac{-Ri_d}{L} + \frac{u_d}{L} \\ &= \frac{-Ri_d}{L} + \frac{k_p (i_d^* - i_d) + \lambda_d}{L} \\ &= \frac{-Ri_d}{L} + \frac{k_p i_d^* - k_p i_d + \lambda_d}{L} \\ &= i_d \left(-\frac{R}{L} - \frac{k_p}{L} \right) + \frac{k_p i_d^*}{L} + \frac{\lambda_d}{L} \end{aligned} \tag{2.21}$$

Expressing (2.20) and (2.21) in the matrix form in (2.16) gives

$$\begin{array}{c} \dot{\mathbf{x}} \\ \left[\begin{array}{c} \frac{di_d}{dt} \\ \frac{d\lambda_d}{dt} \end{array} \right] \end{array} = \begin{array}{c} \mathbf{A} \\ \left[\begin{array}{cc} \frac{-(R+k_p)}{L} & \frac{1}{L} \\ -k_i & 0 \end{array} \right] \end{array} \begin{array}{c} \mathbf{x} \\ \left[\begin{array}{c} i_d \\ \lambda_d \end{array} \right] \end{array} + \begin{array}{c} \mathbf{B} \\ \left[\begin{array}{c} \frac{k_p}{L} \\ k_i \end{array} \right] \end{array} \begin{array}{c} \mathbf{u} \\ i_d^* \end{array}$$

The controllers in this case, as illustrated in Figure 2.8 do not have the C and D components of the state space representation.

A real eigenvalue or a pair of complex eigenvalues is usually referred to as a mode. A mode is used to refer to the natural or characteristic response to a disturbance of the small-signal dynamics of a power system. The real part of an eigenvalue provides the damping, and the imaginary part establishes the frequency of oscillation. The most common way to evaluate the small signal stability of a power system is via modal or eigenvalue analysis. The most essential characteristic of small signal analysis is that it offers an understanding of the power system primary modal

structure and provides insight into its dynamic characteristics that cannot be derived easily from time domain simulations [70]. A complex mode, having real and imaginary parts, is represented in the form of

$$\lambda = \sigma + j\omega \quad (2.22)$$

where the frequency of oscillation and damping ratio are given by

$$f = \frac{\omega}{2\pi} \text{ [Hz]} \quad (2.23)$$

$$\zeta = \frac{-\sigma}{\sqrt{\sigma^2 + \omega^2}} \times 100 \text{ [%]} \quad (2.24)$$

The damping ratio is acceptable if it is between 3 % and 5 % [74].

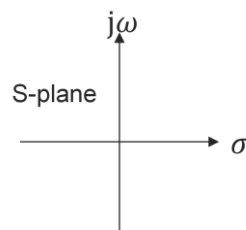


Figure 2-20 The S Plane

The S Plane is given in Figure 2-20. According to Lyapunov's first method, as highlighted in [75]:

- The system is stable if all the eigenvalues are positioned on the left side of the S plane; i.e., when the real part of the eigenvalues are negative. This is known as asymptotic stability.
- The system is considered unstable if there is at least one eigenvalue positioned on the right side of S plane; i.e., the real part of the eigenvalue is positive. The result of this condition it that the state variable can never return to its initial state. This is referred to as aperiodic instability.
- System eigenvalues are usually in the form of complex conjugate pairs. Oscillatory instability occurs if at least one of the complex conjugate pairs falls on the S plane imaginary axis and the system becomes oscillatory.
- If there is at least one eigenvalue is on the origin, the stability of the system cannot be evaluated.

2.11.3 Types of Modes

There are different types of modes depending of their frequency of oscillation and the part of the power system in which they occur. These can be classified as Electromechanical/ Low Frequency Oscillations (LFO) and Sub Synchronous Resonance (SSR). The following section details Low

Frequency Oscillations as these are the focus of this thesis. Sub Synchronous Resonance is outside the scope of this work.

Low Frequency Oscillations

These are electromechanical oscillations caused by the lack of adequate damping torque. These were classified by [69] as follows:

i) Power System Oscillations

- Interarea modes are oscillatory modes taking place between groups of generators that are distant from one another. Generators from a certain location oscillate against generators in another location. Interarea modes typically come about because of power transfer between areas connected by a tie line. Frequencies associated with these modes are typically in the within the range 0.1 to 0.7 Hz.
- Local or Intra-area modes are associated with the oscillation of the rotor angle of one synchronous machine against the rest of the system. These modes are often in the frequency range between 0.7 and 2 Hz.

ii) Sub Synchronous Oscillations (SSOs)

- These oscillatory modes occur in the power system at frequencies below the system frequencies. These exclude electromechanical oscillations associated with rotor swings, and occur at frequencies above 2 Hz. SSOs can be classified into the following as outlined by [76]:
 - Sub Synchronous Torsional Interactions (SSTIs): These are linked to the interaction between the mechanical elements of the synchronous generators and other elements in the power system, for instance, series compensation or reactive power. They also occur between generating units and control systems of HVDC converters.
 - Sub Synchronous Control Interactions (SSCIs): These occur due to interaction between control systems in the electrical power network. These oscillatory modes are due to the controller action in the power system. The controllers include excitation system controllers and power converters controllers.
 - Sub Synchronous Resonance (SSR): This occurs between the generating units and series capacitors.

2.11.4 Right Eigenvector

Using the state space representation of the system, the eigenvalues of the system matrix A is required and thus given by the scalar values of which there are non-trivial solutions to (2.25). The column vector ϕ_i satisfying (2.25) is referred to as the right eigenvector of a specific mode and

provides its mode shape, which illustrates the relative phasors of the state variables when the mode is triggered [77]. The right eigenvector, $\boldsymbol{\varphi}_i$ of the i^{th} mode is given by

$$A\boldsymbol{\varphi}_i = \lambda_i\boldsymbol{\varphi}_i \quad (2.25)$$

Where $\boldsymbol{\varphi}$ is an $n \times 1$ column vector. For any given eigenvalue λ_i , the $n \times 1$ column vector $\boldsymbol{\varphi}_i$, which fulfils (2.25), is known as the right eigenvector of A , related to λ_i . Hence (2.25) can be written as

$$\boldsymbol{\varphi}_i = [\varphi_{1i}, \varphi_{2i}, \dots, \varphi_{ni}]^T \quad (2.26)$$

Given that $i = 1, 2, \dots, n$. The mode shape of λ_i defines the distribution of the mode through the various system state variables. All of the constituents of the mode shape contain information about the observability of the mode of interest in different state variables corresponding to the system [78].

2.11.5 Left Eigenvector

Similarly, the left eigenvector $\boldsymbol{\psi}_i$ associated with the i^{th} mode is given by

$$A\boldsymbol{\psi}_i = \lambda_i\boldsymbol{\psi}_i \quad (2.27)$$

$$\boldsymbol{\psi}_i = [\psi_{1i}, \psi_{2i}, \dots, \psi_{ni}] \quad (2.28)$$

Given that $i = 1, 2, \dots, n$. The system left eigenvector defines the distribution of state variables of a specific mode of interest. The left eigenvector has a direct effect on the amplitude of the mode of interest as excited by a specific state variable. The various components of the left eigenvector contain information regarding the controllability of the mode of interest with respect to the component of interest [78].

2.11.6 Participation Factors

The chief disadvantage in using the left and right eigenvectors to determine system stability and the different relationships governing the state variables and oscillation modes of interest is that the eigenvectors depend on scaling factors and units linked to the various state variables. This can be avoided by introducing the participation matrix P , which connects the left and the right eigenvectors. The participation factors, which are independent of units and scaling of state variables are used to measure the relative participation or magnitude of the state variables in a mode. Participation factors are attained by multiplying the elements of the right eigenvector with those of the left eigenvector.

$$P_{ki} = \varphi_{ki}\psi_{ki} \quad (2.29)$$

Given that φ_{ki} denotes the k^{th} element of the i^{th} right eigenvector and ψ_{ki} gives the k^{th} element of the left eigenvector and p_{ki} is the participation of the k^{th} state variable in the i^{th} mode. The

participation factor matrix of the system is $P = p_1, p_2, \dots, p_n$. This matrix gives the participation of the state variables in all the modes of the system.

2.11.7 Observability and Controllability

Observability and controllability factors are defined to provide a degree of how effective the choice of input signal is (controllability) and how effective the choice of feedback signal is (observability). If the observability factor for a certain mode is zero, then this mode cannot be seen in the selected feedback signal. An input signal to a damping controller should have high observability. If the controllability factor is zero, the mode is not controllable with the selected feedback signal [79].

Conclusion

In this chapter, an overview of the evolution of power systems has been presented as well a comparison of the advantages and shortcomings of AC and DC transmission. This is followed with a detailed explanation of HVDC transmission, highlighting its main advantages over HVAC. Descriptions of the types of topology, converters employed in HVDC transmission are given and an illustration of existing HVDC systems in the world are then presented. Aspects of the control structures that can be used by VSCs are then highlighted. Then, the concept of wind energy generation is introduced. Finally, the chapter explains power system stability, focusing on rotor angle stability and specifically detailing the different aspects of small signal stability which is the main focus of this thesis.

3 COMPONENT MODELLING

This chapter covers the sizing and mathematical modelling of the equipment, parameters and the components used in this research. Calculations are performed to find the HVDC parameter values used in the simulation. Modelling of the VSC controllers and wind components are illustrated here.

3.1 MODEL CONTEXTUALIZATION

The system contextualization is the Caprivi link Interconnector (CLI) that was constructed to supply electricity to the Namibia Electrical Grid (NamPower) from the Zambia Electrical Grid (ZESCO). This power is mainly generated by its hydropower units. The sizes and ratings of the equipment and parameters modelled (transformers, converters, voltage levels, DC line length) are of those used in the CLI. The modelled system (Figure 3-1 for the VSC and Figure 3-2 for the CLI system) is a 300 MW 350 kV (DC) Symmetric Monopole as this is the rating of the (CLI). Currently, however, this system is not being used at its full capacity and only transfers about 80 to 100 MW of power because of constraints on the Zambian side, which itself has a generation deficiency. Utilization of this system would require increased generation capacity from Zambia or other countries such as DR Congo, Zimbabwe or Botswana. The link, in future may also be used to transmit electricity to or from South Africa. One way to increase generation capacity is to invest in implementing more renewable energy plants such as wind and solar energy. Hence the incorporation of a wind farm into the modelled system.

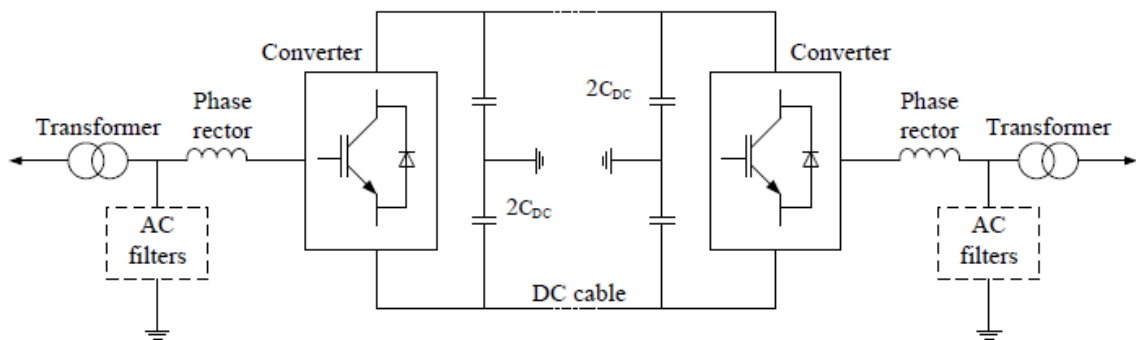


Figure 3-1 Simplified Representation of VSC-HVDC System[52]

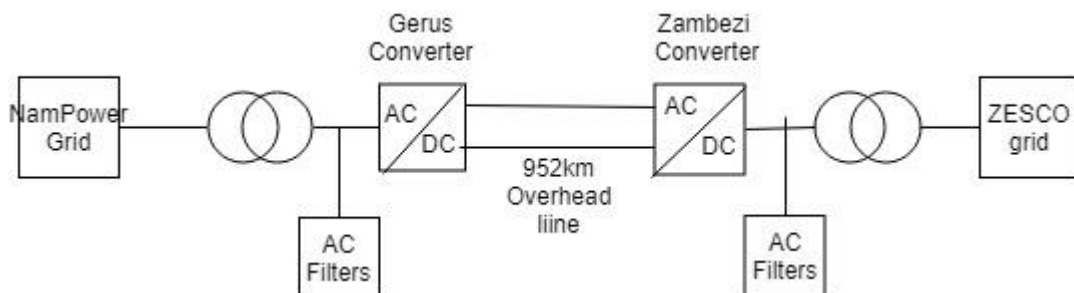


Figure 3-2 Simplified Representation of Caprivi Link Interconnector [3]

3.2 DC POWER RATING

The Caprivi Link Interconnector was built to transfer electricity from the Zambia AC grid to the Namibia AC Grid. The sending end voltage on the Zambian side is 330 kV. The maximum power, if it were being taken directly from the 330 kV AC bus bar, can be obtained from the following process. The relationship between the AC system line voltage and DC link voltage is

$$V_{LL} = \frac{\sqrt{3}U_{dc}M}{2\sqrt{2}} = 0.612MU_{dc} \quad (3.1)$$

where V_{LL} represents the AC line-to-line voltage, U_{dc} is the DC link voltage and M gives the modulation index ($0 \leq M \leq 1$) [80]. From this equation, and taking M as 0.85:

$$U_{dc} = \frac{330}{0.612 \times 0.85} = 634.37 \text{ kV}$$

The DC power is

$$P_{dc} = U_{dc}I_{dc} \quad (3.2)$$

where current rating of a VSC converter is between 500 A and 1500 A. The current rating of the converters used for the Caprivi Link Interconnector is 890 A. Therefore, the maximum transmittable power is

$$P_{dc} = 634.37 \text{ kV} \times 890 \text{ A} = 564.6 \text{ MW}$$

The monopole was planned for a maximum power transfer of 300 MW which is well under the calculated 564.6 MW and therefore validates the 300MW rating.

3.3 DC LINE

The monopole was designed for 300 MW power transmission (and total of 600 MW for the future bipole extension), so one DC line should have a rating:

$$U_{dc} = \frac{P_{dc}}{I_{dc}} = \frac{300 \text{ MW}}{890 \text{ A}} = 337 \text{ kV}$$

The value is taken as 350 kV allowing for a 5 % contingency.

3.4 CONVERTER SIZING

The converters employed in this system are two-level voltage source converters that have six valves, formed from an IGBT and an anti-parallel diode. The IGBTs have a frequency range from 1 to 2 kHz. With a converter current rating of 890 A, and a DC line voltage rating of 350 kV:

$$P_{dc} = 350 \text{ kV} \times 890 \text{ A} = 311.5 \text{ MW}$$

The converter therefore has a rating of 315 MW including contingencies, and an overload rating of 345 MW.

3.5 TRANSFORMER SIZING

The transformers connect the AC system to the converter valve bridges and change the AC voltage level to an appropriate level for the VSC converters.

3.5.1 Transformer on the Zambia side

From (3.1), taking $M = 1$, the DC line voltage is

$$V_{LL} = 0.612 \times 1 \times 5 \times 350 = 214.2 \text{ kV}$$

The limits of V_{LL} should be within $\pm 5\%$. The V_{LL} maximum limit will be used in the transformer sizing to allow for contingencies so that

$$V_{LL \text{ max}} = \left(\frac{5}{100} \times 214.2 \right) + 214.2 = 224.91 \approx 225 \text{ kV}$$

This is the secondary voltage of the transformer. The primary voltage is known to be 330 kV from the AC grid voltage. Therefore, the simulated transformer should be a 330 kV/225 kV step down transformer.

3.5.2 Transformer on the Namibia side

The busbar voltage is 400 kV on the Namibia end at Gerus, therefore the transformer at the inverter side should be a 225 kV/400 kV step up transformer.

The apparent power rating of the transformers is given by

$$S = \frac{P}{\cos \theta} \quad (3.3)$$

Assuming unity power factor, the transformer rating should be 315 MVA.

3.6 DC CAPACITOR SIZING

The DC link capacitors in Figure 3-1 provide steady DC voltage and act as charge reservoirs so that steady DC current flows in the DC transmission line and switching transients are limited to the converters. The DC capacitors minimise ripple presented by harmonics introduced by the VSC to the DC side [80]. They can be sized from

$$C_{dc} = \frac{\tau S_N}{0.5 U_{dcN}^2} \quad (3.4)$$

where the time constant τ is the period required to charge the capacitor from zero to the rated voltage U_{dcN} when the converter is operating at the nominal volt-amps S_N . τ can be selected to be lower than 5 ms to obtain only minor ripple in the transient overvoltage on the DC voltage. A value of $\tau = 1.5$ ms was used in this project so that

$$Q = \frac{V^2}{X_c} = V^2 (2\pi f) C_{dc} \quad (3.5)$$

Where Q is the reactive power rating of the capacitor, f is the electrical frequency and C_{dc} is the total DC capacitor size.

Applying (3.4) and (3.5):

$$C_{dc}(\text{Total}) = \frac{(0.0015)(315)}{(0.5)(350^2)} = 7.7134 \times 10^{-6} \text{ F}$$

Therefore the two series capacitors on each end of the DC Link, give a total equivalence of 7.7143×10^{-6} F. Each of the capacitors are then individually sized using:

$$\frac{1}{C_{eq}} = \frac{1}{C_1} + \frac{1}{C_2} \quad (3.6)$$

$$C_1 = C_2 = 15.43 \times 10^{-6} \text{ F}$$

$$Q_{\text{Total}} = (350^2)(2\pi \times 50)(7.7134 \times 10^{-6})$$

$$Q_{\text{Total}} = 296.73 \text{ MVar} = 300 \text{ MVar}$$

3.7 PHASE REACTORS

The phase reactor in Figure 3-1 controls the active and reactive power between the converter and the AC system. The voltage across the reactor causes a current of phase and magnitude that limits the power injected or absorbed by the converter [81]. The phase reactor also limits short-circuit currents when faults occur in the DC side of the converter and filters the high frequency harmonics of the current. The AC reactors also serve the purpose of reducing harmonic currents. DC reactors on the other hand, decrease harmonic voltages and currents in the DC line. These DC side harmonics, if not combated, may cause interference in neighbouring telephone systems.

The phase reactors are usually in the range 0.1 to 0.2 pu [80] where the resistance is 1 % of the inductive reactance [82]. For this project, the inductor was chosen to be 0.1 pu, therefore the resistance was 0.001 pu.

3.7.1 AC Phase Reactors

To calculate the phase reactance:

$$Z = \frac{\sqrt{3}V^2}{S} \quad (3.7)$$

$$Z_{\text{base}} = \frac{\sqrt{3}(225 \text{ kV})^2}{345 \text{ MVA}} = 254.16 \ \Omega$$

$$\omega L = Z(\text{ pu })Z_{\text{base}} \tag{3.8}$$

$$L = \frac{(0.1)(254.16)}{2\pi(50)} = 0.0809 \text{ H} = 80.9 \text{ mH}$$

$$R = (1\%)(0.1) = 0.001 Z_{\text{base}} = 0.254 \ \Omega$$

3.7.2 DC Line Phase Reactors

The DC line reactors can also be calculated:

$$Z_{\text{base}} = \frac{\sqrt{3}(350 \text{ kV})^2}{345 \text{ MVA}} = 614.99 \ \Omega$$

$$X_L = \omega L = 614.99 \ \Omega$$

$$L = \frac{(0.1)(614.99)}{2\pi \times 50} = 0.196 \text{ H} = 196 \text{ mH}$$

$$R = (1\%)(0.1) = 0.001 Z_{\text{base}} = 0.615 \ \Omega$$

3.8 CONTROL SYSTEM

The control method used in this research was the vector control method which uses the dq transformation system that is used to translate the three-phase stationary coordinates into a two-phase rotating system. To start, the three-phase stationary coordinate system is converted to the two-phase, α - β stationary coordinate system and then the α - β stationary coordinate system is transformed to the dq rotating coordinate system [83].

Clark and Inverse-Clark transformations are used for the transformation into the stationary α - β reference frame and vice-versa, and translate the values from the stationary α - β reference frame to the synchronously rotating dq reference frame, or from the synchronously rotating d-q to the stationary α - β reference frame. Figure 3-3 shows the reference frames.

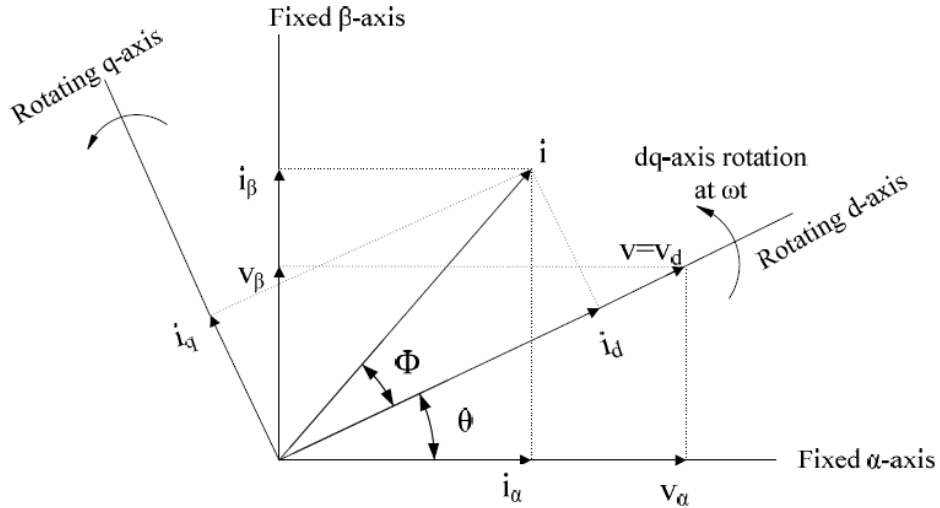


Figure 3-3 Vector control transformation axes [83]

3.9 INNER CURRENT CONTROL LOOP

The inner current control loop, whose block diagram is shown in Figure 3-5, is made up of controllers, decoupling factors and feedforward terms. From Figure 3-4, the converter equations, when transformed to the dq axes, can be written as

$$L \frac{di_d}{dt} = -Ri_d + \omega_e Li_q - u_d + v_d \quad (3.9)$$

$$L \frac{di_q}{dt} = -Ri_q + \omega_e Li_d - u_q + v_q \quad (3.10)$$

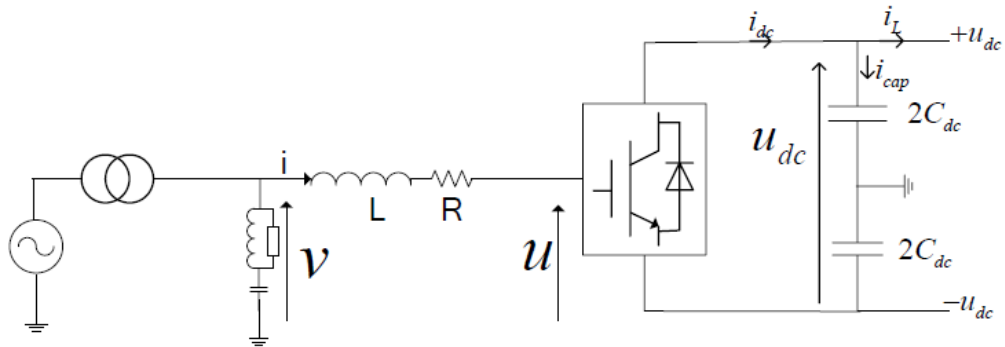


Figure 3-4 VSC Model Single Line Diagram [80]

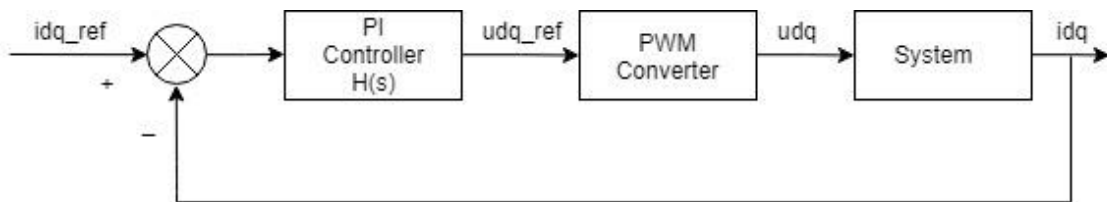


Figure 3-5 Inner current controller block diagram

There are two regulators inside the controller block, one for the d axis and the other for the q axis current control which are responsible for generating a voltage set point $u_{d\ ref}$.

3.9.1 PI Regulator

The PI regulator can be represented by

$$H(s) = K_p + \frac{K_i}{s} = K_p \left(\frac{1 + T_i s}{T_i s} \right) \quad (3.11)$$

Given that K_p is the proportional gain, T_i is the integral time constant given by $T_i = \frac{K_p}{K_i}$.

The phase reactors and filters remove almost all harmonics as seen from the grid side. Therefore it is assumed that $u_{dq} = u_{dq\ ref}$. The output of the PI regulator block is therefore

$$u_{dq\ ref} = \left[I_{dq\ ref}(s) - I(s) \right] \left(K_p + \frac{K_i}{s} \right) \quad (3.12)$$

3.9.2 PWM Converter

The output of the converter is taken as an ideal transformer with a time delay. The voltage output of the converter follows a reference voltage signal which can be generally represented as

$$Y(s) = \frac{1}{1 + T_a s} \quad (3.13)$$

where $T_a = \frac{T_{switch}}{2} * 3$.

3.9.3 System

The system transfer functions can be taken from (3.9) and (3.10) and be re-written as

$$v_d - u_d = L \frac{di_d}{dt} + Ri_d - \omega_e Li_q \quad (3.14)$$

$$v_q - u_q = L \frac{di_q}{dt} + Ri_q + \omega_e Li_d \quad (3.15)$$

Where $\omega_e Li_d$ and $\omega_e Li_q$ are the cross-coupling terms between the two axes and can be considered as a disturbance in terms of a control angle [80].

3.10 OUTER CONTROLLER LOOPS

The outer controllers provide reference signals of the d and q components. The signal $i_{d\ ref}$ can be controlled by either the active power or the DC voltage; $i_{q\ ref}$ is controlled by the reactive power or AC voltage [82].

3.10.1 DC Voltage Control

This voltage controller is responsible for maintaining the active power exchange between the VSC-HVDC converters. The equations for active and reactive power are given by

$$P = v_d i_d ref \quad (3.16)$$

$$Q = -v_d i_q ref \quad (3.17)$$

The AC and DC sides of the converter, ignoring converter losses, can be represented using

$$i_{dc} = \frac{v_d}{u_{dc}} i_d ref \quad (3.18)$$

The imbalance between the AC and DC power leads to a change in voltage over the DC link capacitors, so that

$$C_{dc} \frac{du_{dc}}{dt} = \frac{v_d}{u_{dc}} i_d - i_L \quad (3.19)$$

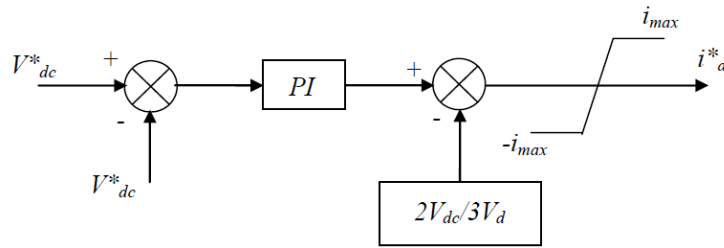


Figure 3-6 DC voltage controller block diagram [52]

Under unbalanced conditions, $i_{dc} = i_L$, therefore the reference of the d axis current $i_d ref$ will be $\frac{3u_{dc}}{2v_d} i_L$, where the $3/2$ factor is obtained from the Park's transformation [52].

3.10.2 Active and Reactive Power Control

The active and reactive power blocks can be represented by the control block shown in Figure 3-7 and, if v_d is assumed to be constant, expressed as

$$i_d ref = \frac{P_{ref}}{v_d} \quad (3.20)$$

$$i_q ref = -\frac{Q_{ref}}{v_d} \quad (3.21)$$

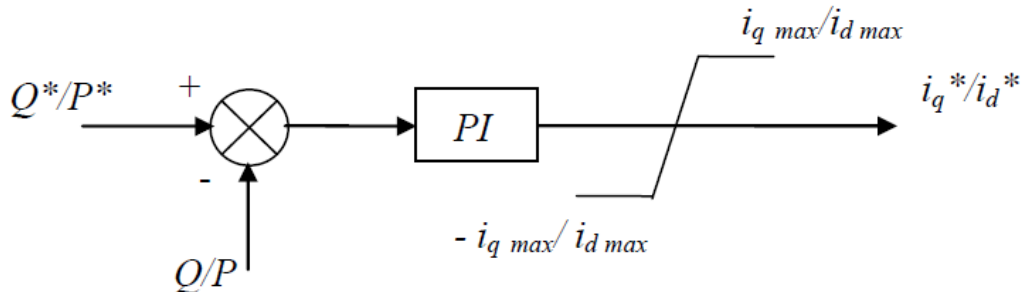


Figure 3-7 Active and Reactive power controller blocks [52]

3.10.3 AC Voltage Control

From Figure 3-4, the voltage drop over the phase reactor can be approximated using

$$\begin{aligned}
\Delta v &= v - u \approx v_d - u_d \\
(v_q = 0 \text{ (} v \text{ is reference) and } |u_d| \gg |u_q|) \\
\Delta v &\approx i_d R_p + i_q \omega_e L_q \approx i_q \omega_e L_q \\
Q &= v i_q \\
\Delta v &\approx Q \frac{\omega_e L_q}{v}
\end{aligned} \tag{3.22}$$

Taking $\omega_e L \gg R$ for the phase reactor, the reactor voltage drop depends on the flow of reactive power. With this assumption, the AC voltage variation depends on the reactive power flow, meaning the voltage can be regulated by controlling the q component of the current.

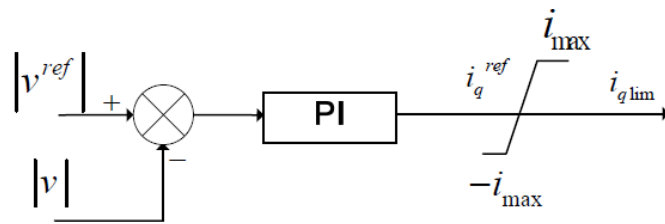


Figure 3-8 AC Voltage control block [80]

3.11 WIND FARM MODELLING

The models of the wind speed, the mechanics, aerodynamics and the control systems of the wind turbines are written in the dynamic simulation language (DSL) of DIgSILENT. DSL makes it possible for users to build their own blocks either as variations of existing models or as original models. These new models can be collected into a library, which can be easily used in the modelling of other wind farms with other wind turbines.

DIgSILENT software has been extended and developed for wind power applications, based on extensive communication and collaboration between DIgSILENT and Risø DTU National Laboratory for Sustainable Energy [84]. There are the two types of models in DIgSILENT that can be used for wind farm application:

1. Built-in models, which are standard electrical component models which already exist in the DIgSILENT library. A built-in model is used in this research.
2. DSL models, which are created by the user in the dynamic simulation language DSL.

There are four different types of wind turbine systems with different arrangements, as discussed in Chapter 2. Seven models that are described in the IEC 61400-27-1 that are available in DIgSILENT PowerFactory:

- **Type 1a:** Wind turbine with asynchronous generator directly connected to the grid

- **Type 1b:** Wind turbine with asynchronous generator directly connected to the grid with UVRT pitch control
- **Type 2:** Wind turbine with asynchronous generator with variable rotor resistance directly connected to the grid
- **Type 3a:** Wind turbine with doubly fed induction generator (DFIG)
- **Type 3b:** Wind turbine with doubly fed induction generator with crowbar
- **Type 4a:** Wind turbine connected through full-scale power converter
- **Type 4b:** Wind turbine connected through full-scale power converter with mechanical model

3.11.1 IEC 61400-27-1 Type 3a Wind Turbine Model

Type 3a DFIG Wind Generators of specification IEC 61400-27-1 rated at 2 MW are deployed in this thesis as built in DIgSILENT Power Factory. This IEC model is encrypted in DIgSILENT and therefore reference should be made to IEC 61400-27-1 for more details. The IEC 61400-27-1 can also be used for aggregated representation of several wind turbines or a whole wind farm in DIgSILENT by adjusting the number of parallel wind turbines. This was done for this research. The active power output of the generator is the active power dispatch times the number of parallel machines.

3.11.2 Mathematical Model of DFIG

A wind turbine is characterised by its power-speed characteristics. For a horizontal axis wind turbine, the amount of mechanical power P_{mech} , that a turbine produces in steady state is given by

$$P_{mech} = \frac{1}{2} \rho \pi R^2 u^3 C_p(\theta, \lambda) \quad (3.23)$$

where:

- ρ is the air density
- R is the turbine radius
- u is the wind speed
- $C_p(\theta, \lambda)$ is the power coefficient which depends on the pitch blade angle θ and the tip speed ratio λ . It is given by

$$\lambda = \frac{\omega_{rot} R}{u} \quad (3.24)$$

- ω_{rot} is the rotor turbine speed.

The power coefficient, C_p has a maximum value of 59 % meaning that the amount of power that can be extracted from an undisturbed tube of air with the cross-sectional area equal to the wind

turbine swept area cannot exceed 59 % of the total power [85]. This is called the Betz Law and is illustrated by

$$P_{ideal} = \left[\frac{1}{2} \rho \frac{8}{9} \left(\frac{2}{3} A \right) u^3 \right] = \frac{16}{27} \left(\frac{2}{3} \right) \rho \pi R^2 u^3 = 0.59 P_w \quad (3.25)$$

The system of equations for the DFIG comprises of two voltage equations, two flux equations and an equation of motion as presented in [86].

3.11.3 Voltage Equations

These are given by

$$u_s = r_s i_s + j \omega \psi_s + \frac{d\psi_s}{dt} \quad (3.26)$$

$$u_R = r_R i_R + j(\omega_0 - \omega_R) \psi_R + \frac{d\psi_R}{dt} \quad (3.27)$$

where:

- u_s is the stator voltage
- r_s is the stator resistance
- i_s is the stator current
- ω_0 is the synchronous speed
- ψ_s is the stator flux linkages
- u_R is the rotor voltage
- r_R is the rotor resistance
- i_R is the rotor current
- ω_R is the speed of the machine
- ψ_R is the rotor flux linkages

3.11.4 Flux Equations

These are given by

$$\psi_s = l_s i_s + l_M i_R \quad (3.28)$$

$$\psi_R = l_M i_s + l_R i_R \quad (3.29)$$

where:

- l_s is the stator self-inductance
- l_R is the rotor self-inductance
- l_M is the mutual inductance between stator and rotor

3.11.5 Equation of Motion

The equation related to the motion of the turbine is given by

$$\frac{d\omega_R}{dt} = \frac{1}{\theta_m} \left[k_R (\psi_{Rd} i_{sq} - \psi_{Rq} i_{sd}) + t_m \right] \quad (3.30)$$

where:

- ψ_{Rd} is the rotor flux linkages aligned with d-axis
- i_{sq} is the stator current aligned with q-axis
- ψ_{Rq} is the rotor flux linkages aligned with q-axis
- ψ_{sd} is the Stator current aligned with d-axis
- t_m is the mechanical torque of the machine

The inductances are defined by

$$l_s = l_h + l_{\sigma s} \quad (3.31)$$

$$l_R = l_h + l_{\sigma R} \quad (3.32)$$

- l_h is the magnetizing inductance
- $l_{\sigma s}$ is the Stator leakage inductance
- $l_{\sigma R}$ is the Rotor leakage inductance

3.12 MODAL ANALYSIS

Modal analysis can be performed when the system is in steady state after a load flow calculation, or after an RMS simulation [87]. The modal analysis is only valid when the system is subjected to small disturbances. In this research a small increase in load was induced in order to excite the oscillatory modes. The modal analysis builds a matrix system from the load flow and dynamic data. The eigenvalues and eigenvectors are then calculated from this matrix. DIGSILENT automatically does the linearization of the system since eigenvalue calculations can only be performed on a linear system. The implementation of the modal analysis as performed in DIGSILENT can therefore be summarized in the following steps:

1. Calculate the initial conditions of the system, ensuring that there is a convergence in the load flow.
2. Modal analysis calculation using either the QR/QZ or the Arnoldi/ Lanczos method.
3. Perform participation factor analysis on oscillatory modes.

The QR/QZ method is the conventional method of calculating the system eigenvalues and calculates all system modes. Whereas Arnoldi/ Lanczos (Selective Modal Analysis) method only calculates a part of the system eigenvalues about a certain reference point. This method is often used in extremely large systems and can be time consuming. It is particularly useful if the target area of interest for the eigenvalues are known. For this research, the QR/QZ method of modal analysis was used.

Conclusion

This chapter highlighted the sizing and mathematical modelling of the equipment, parameters and the components employed during the simulation phase of the research. Modelling of the VSC controllers and wind components were also done in this chapter.

4 MODEL VALIDATION AND TESTING

The focus of this chapter is to present the base network model used in this dissertation which consists of two networks interconnected through a HVDC transmission line using VSC converters. This is shown in Figure 4-1. The model represents the Zambia – Namibia Caprivi Link Interconnector. This is a 952 km, 350 kV overhead line. The Zambian network supplies power to the other area. It comprises a synchronous generator, and a local load of 5 MW, 1 MVar at 0.98 power factor, as the sending end. The receiving Namibian is modelled with an AC grid with a short circuit ratio of 5 and short circuit level at 10 000 MVA. This is external to the simulation as can be seen in Figure 4-1. The base network model was built and validated using DIgSILENT PowerFactory. This chapter presents the validation results of the VSC controllers used in this dissertation and goes on to present the small stability of the base network to identify the modes initially present.

4.1 BASE CASE

4.1.1 HVDC Parameters

The base case is shown in Figure 4-1 and VSC-HVDC parameters that are used in the base case are as calculated in Chapter 3. Table 4-1 summarises the parameter values used in the base case.

Table 4-1 VSC-HVDC Parameters used in Base Case

Parameter	Rating
DC Line	350 kV
DC Phase Reactors	$L = 196 \text{ mH}, R = 0.615 \Omega$
DC Capacitor	$1.543 \times 10^{-5} \text{ F},$ Total Q rating 300 MVar
Converter	315 MW, 890 A
Zambia Side Transformer	330/225 kV step down
Namibia Side Transformer	225/400 kV step up
AC Phase Reactors	$L = 80.9 \text{ mH}, R = 0.254 \Omega$

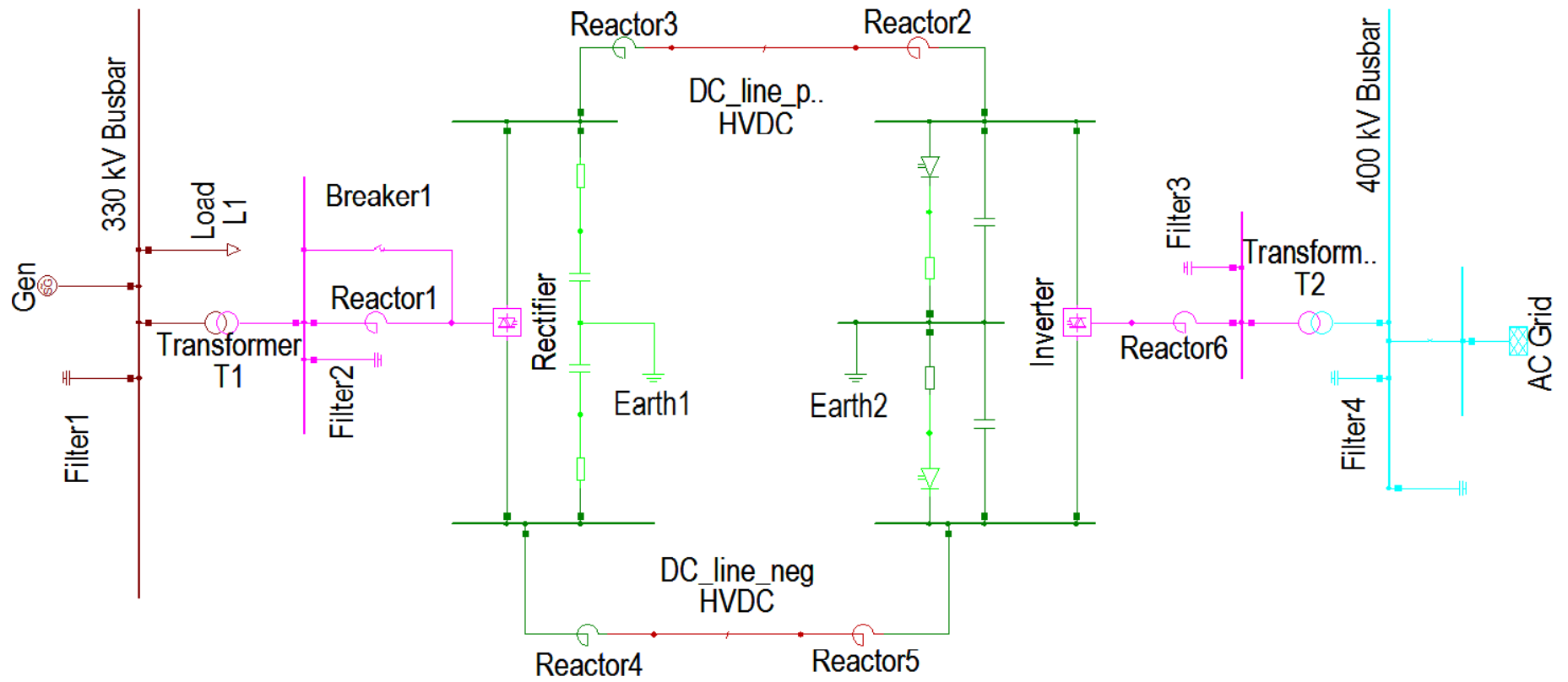


Figure 4-1 Base Case Network

4.2 VSC CONTROLLER PARAMETERS

4.2.1 Inner Controller

A PI controller is used for the inner controller. The inner controller has two PI controller blocks for the d and q axis signals. The d axis reference signal (i_{d_ref}) is compared with i_d which is measured from the system. The reference signals are obtained from the outer controllers. The same occurs for the q axis signals. The inner controller output is then compared with the carrier signal of the pulse width modulator (PWM). This controls the switching of the voltage source converter. The output signals of the inner controller are P_{md} and P_{mq} . The proportional gain of the inner current controller is $K = 2$ with an integral time of 0.002 s. The block diagram of the inner current controller is shown in Figure 4-2.

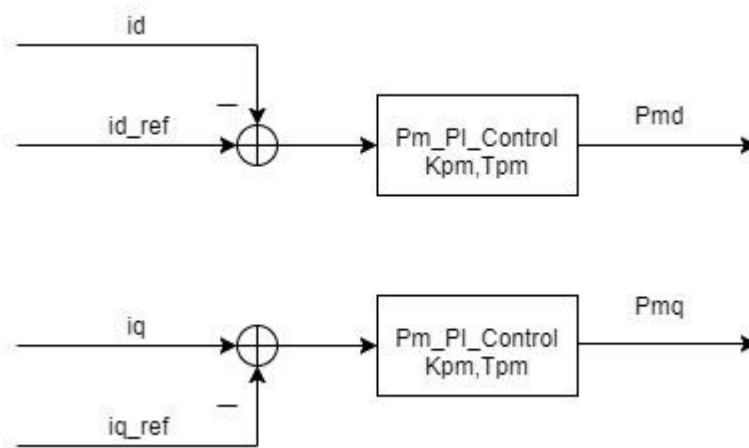


Figure 4-2 Inner Controller Block Diagram

4.2.2 Outer Controller

The outer controllers consist of a DC voltage controller. This generates a reference signal for the d axis (i_{d_ref}). The q axis reference signals (i_{q_ref}) are generated by a reactive power and AC voltage controller as shown in Appendix A-2. The reference signals produced by the outer controllers are fed to the inner current controller. The controller parameters are shown in Table 4.2.

Table 4-2 Outer Controller Parameters

Parameter	Value
Voltage controller Gain	10
Integral time constant of DC controller	0.1 s
AC and reactive power controller Gain	12
Integral time constant of AC and reactive power controller	100 s

4.3 CONTROLLER STEP RESPONSE TEST

A step response test is then used to verify that the VSCs are operating correctly for both the d and q axis controllers. To verify that the controllers are functioning as they should, the actual output signal from the controller should track its reference value.

The first test performed is the AC voltage step response, whose reference value is 0.9934 pu which is a pre-set value. An event is created to increase it to 1.02 pu after one second. Figure 4.3 shows that the AC voltage follows the reference value even when it is changed. A DC step response test event is also done where the DC reference value is increased from 1.0 pu to 1.046 pu at 1 s. Figure 4.4 shows that the DC voltage tracks its reference value even when it is changed. This confirms that the controllers are working correctly.

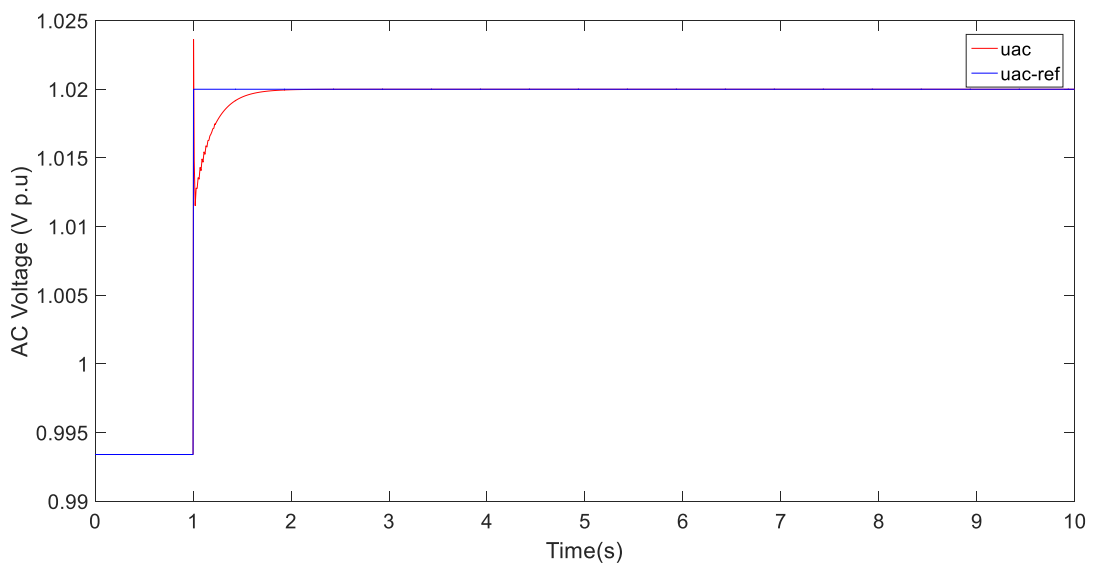


Figure 4-3 AC Voltage Step Response Test

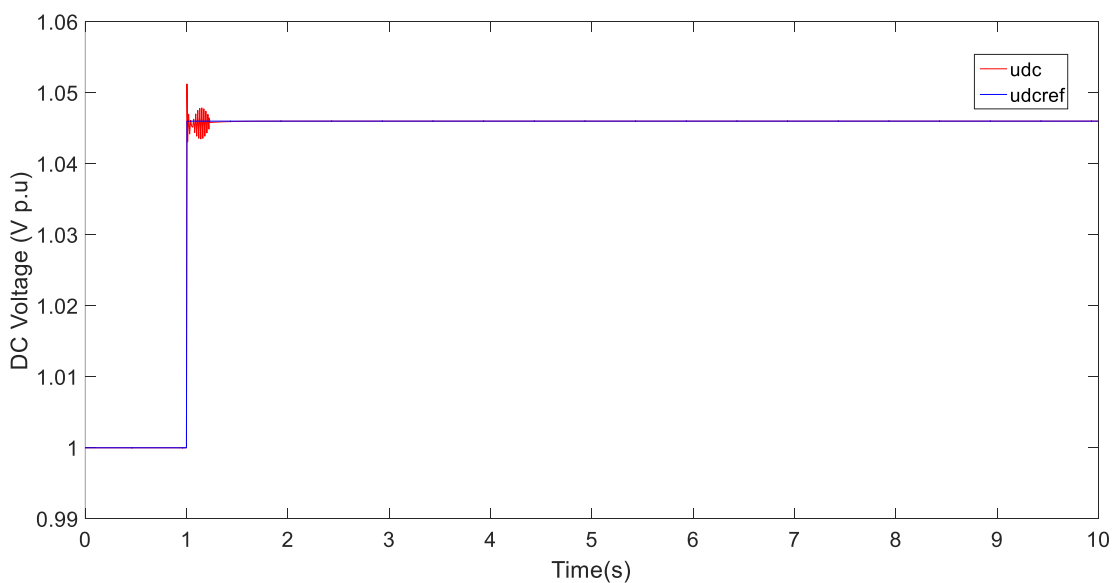


Figure 4-4 DC Voltage Step Response Test

4.4 BASE CASE MODAL ANALYSIS

A modal analysis of the base case having SCR = 5, and a small disturbance in the form of a 20 % load increase is done and found to have 10 oscillatory modes, of 5 complex conjugate pairs. The eigenvalue plot is shown in Figure 4-5.

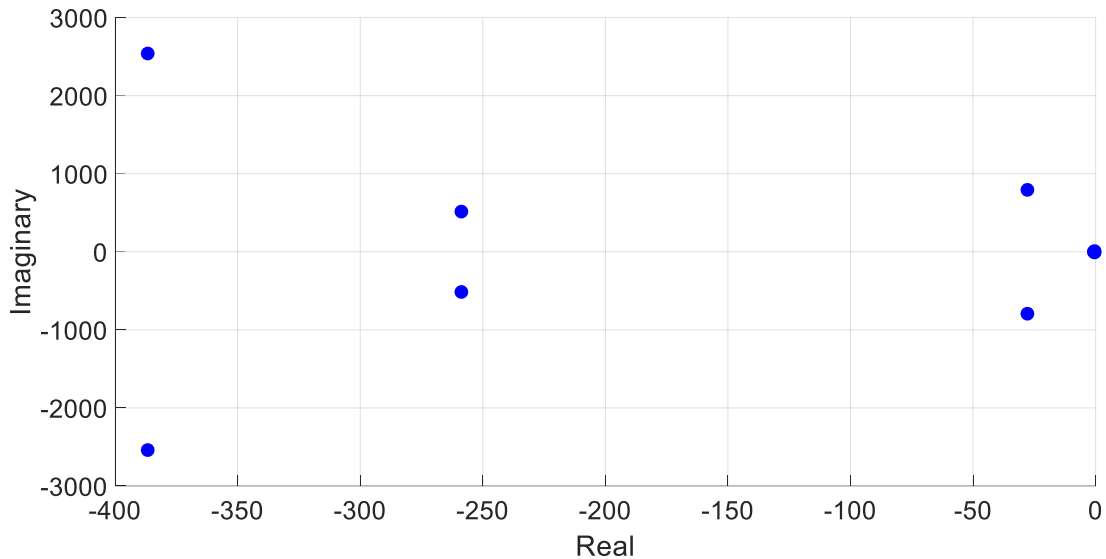


Figure 4-5 Eigenvalue plot of base case

All the real parts are negative and therefore the system is stable. All the modes are well damped. Table 4-3 gives a summary of the modes. Modes 18 & 19 and 22 & 23 have frequencies of 405 Hz and 82 Hz respectively. These are super synchronous oscillations caused by interaction between the controllers. These oscillations are damped out of the system very quickly; their damping time is in the order of 3 ms. Modes 20 & 21 had the lowest damping of 3.6 % at a frequency of 126.8 Hz and the participation factor shows that these oscillations were as a result of the DC line reactance. Mode pair 46 & 47 is also poorly damped at 5.4 % damping ratio with a slow damping time of 2.83 s. This is an electromechanical mode, specifically a local area mode, caused by the main generator oscillating against the rest of the system.

Table 4-3 Base Case Eigenvalues

Mode	Real Part[σ]	Imaginary Part[$j\omega$]	Frequency [Hz]	Damping Ratio	Damping Time Constant [s]
Mode 00018	-386.674	2542.461	404.6	0.1504	0.00259
Mode 00019	-386.674	-2542.46	404.6	0.1504	0.00259
Mode 00020	-27.7014	796.7085	126.8	0.0347	0.0361
Mode 00021	-27.7014	-796.709	126.8	0.0347	0.0361
Mode 00022	-258.867	516.7886	82.25	0.4479	0.00386
Mode 00023	-258.867	-516.789	82.25	0.4479	0.00386
Mode 00046	-0.35348	6.567553	1.045	0.0537	2.82902
Mode 00047	-0.35348	-6.56755	1.045	0.0537	2.82902
Mode 00050	-0.71799	0.465354	0.074	0.8392	1.39278
Mode 00051	-0.71799	-0.46535	0.074	0.8392	1.39278

Conclusion

The focus of this chapter was to validate the base model that employed the parameter values that were calculated in Chapter 3. The results of this chapter was the basis of the rest of the research as it sets the yardstick of how the different changes in the system affects its small signal stability.

5 RESULTS AND ANALYSIS

This chapter highlights the results obtained from simulations of the monopole and bipole systems with the incorporation of an onshore wind farm as an auxiliary supply to the VSC-HVDC link. The conditions explored include change in Short Circuit Ratio (SCR) as a measure of AC grid strength, change in inner and outer controller gains, and lastly varying wind power generation. The aim of the simulations was to establish the effects of incorporating wind energy into an HVDC system as well as the effect of the different conditions on the small signal stability. The chapter also provides a comparison between the bipole and monopole systems in terms of their small signal stability under the different conditions.

5.1 MONOPOLE WITH WIND POWER GENERATION

Figure 5-1. The wind farm is an aggregate wind power plant employing 50 wind generator units in parallel having a total capacity of 100 MW. This choice is motivated by the fact that the largest wind farms currently in South Africa have capacities ranging between 138 and 140 MW [88, 89]. The wind generators used in the research are Type 3 DFIG Wind Generators of IEC 61400-27-1 specification rated at 2 MW. These are a common type of generator used for onshore wind power generation. They can operate in variable winds while employing converters that are rated at only about 30 % of the generator capacity. The average rating for a wind turbine is in the range of 2 MW to 2.5 MW [90], therefore a value of 2 MW is selected for this study.

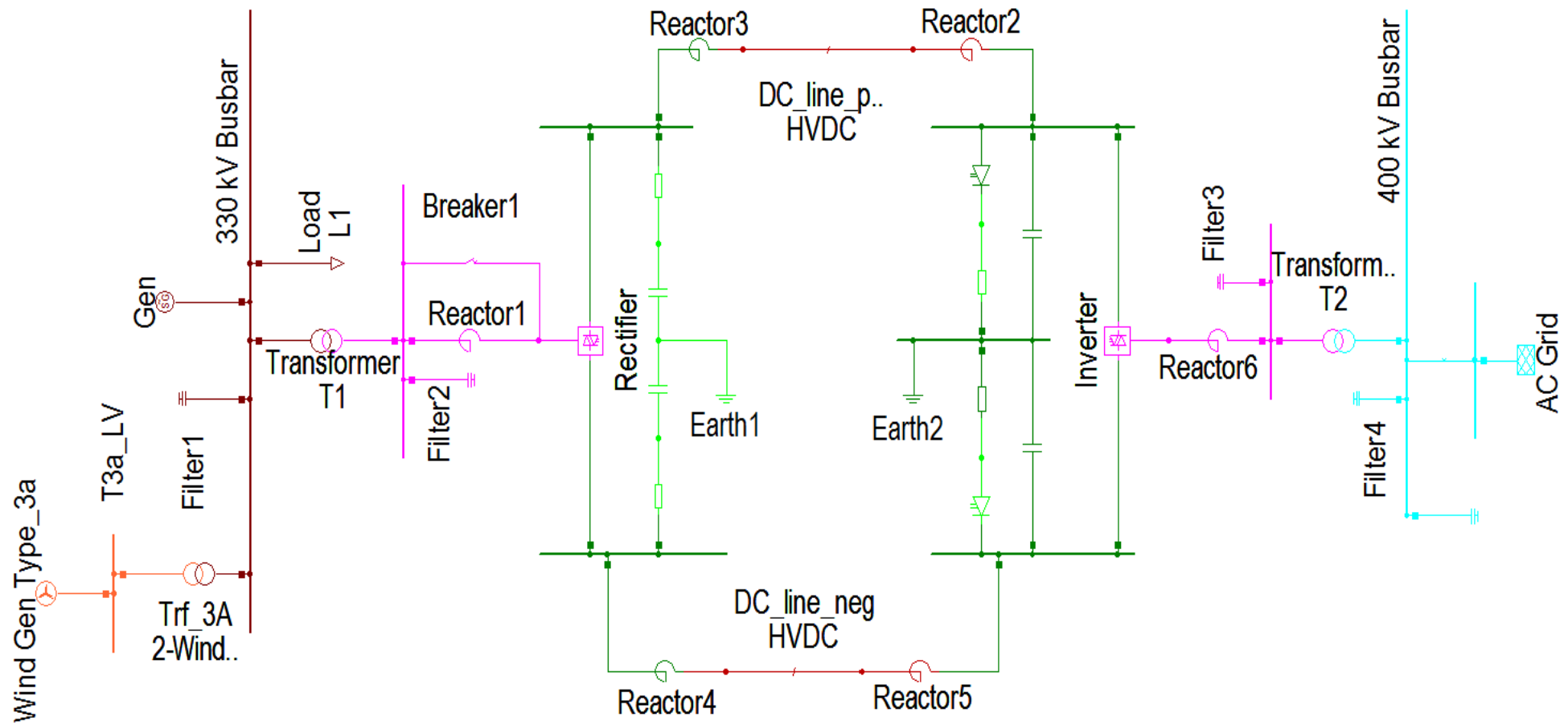


Figure 5-1 Monopole with wind power generation network

5.2 SMALL SIGNAL STABILITY ANALYSIS

A modal analysis of the monopole with wind power generation is performed. A small disturbance in the form of a 20 % increase of the load connected to the 330 kV busbar is simulated to excite the oscillatory modes. The system has 18 oscillatory modes with 9 complex conjugate pairs. The incorporation of the wind farm introduces 8 oscillatory modes or 4 mode pairs in addition to the oscillatory modes that are already in the system as shown in Figure 5-2.

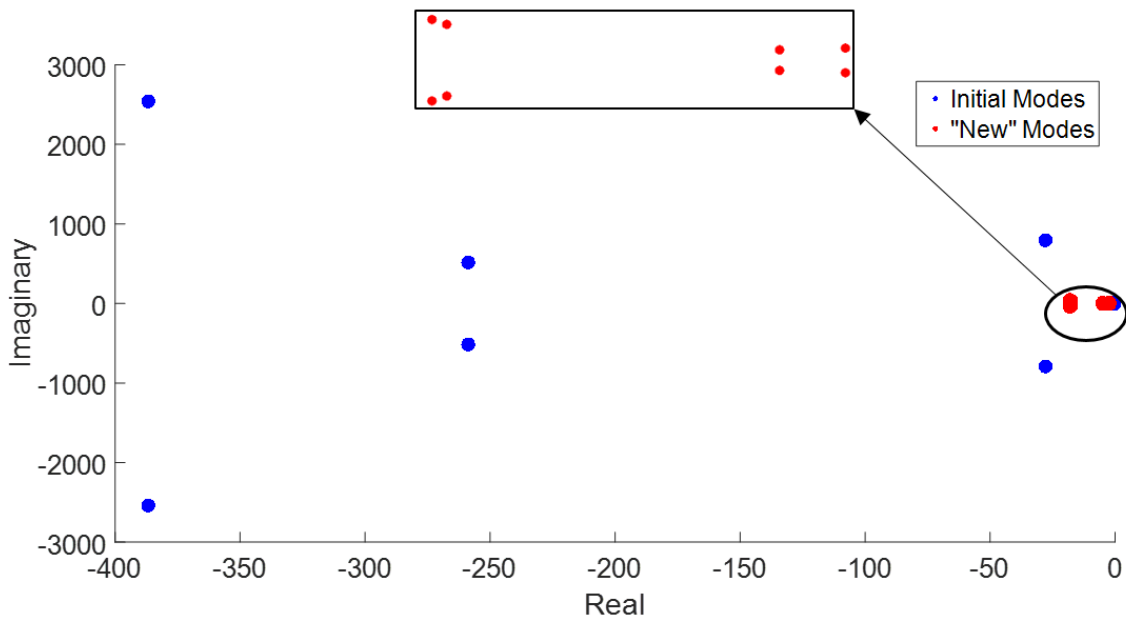


Figure 5-2 Eigenvalues of Monopole with Wind Generation

The added modes are highlighted in Table 5-1. The new modes are all very well damped and the system is stable. The incorporation of wind generation causes mode pair 46 & 47, which already had a low damping ratio of 5.5 % with a damping time of 2.83 s in the base case, to move and become less stable as its real part moves towards the imaginary axis. The damping also reduces to 4.8 % and therefore increases the damping time to 3.15 s.

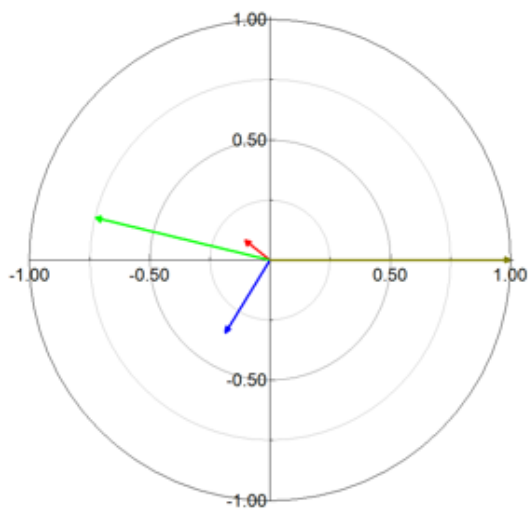
Table 5-1 Eigenvectors of VSC Monopole HVDC with wind power generation

Mode	Real Part [σ]	Imaginary Part [jω]	Damped Frequency [Hz]	Damping Ratio	Damping Time [s]
Mode 00018	-386.756	2542.449	404.6	0.1504	0.00259
Mode 00019	-386.756	-2542.45	404.6	0.1504	0.00259
Mode 00020	-27.7014	796.7085	126.8	0.0347	0.0361
Mode 00021	-27.7014	-796.709	126.8	0.0347	0.0361
Mode 00022	-258.788	516.8169	82.25	0.4477	0.00386
Mode 00023	-258.788	-516.817	82.25	0.4477	0.00386
Mode 00031	-18.0521	39.97825	6.362	0.4115	0.0554
Mode 00032	-18.0521	-39.9783	6.362	0.4115	0.0554
Mode 00033	-17.495	35.0154	5.572	0.44695	0.0572
Mode 00034	-17.495	-35.0154	5.572	0.44695	0.0572
Mode 00037	-2.37679	12.12434	1.9296	0.19237	0.4207
Mode 00038	-2.37679	-12.1243	1.9296	0.19237	0.4207
Mode 00039	-4.88313	10.06711	1.602	0.43643	0.20479
Mode 00040	-4.88313	-10.0671	1.602	0.43643	0.20479
Mode 00046	-0.31801	6.643686	1.057	0.0478	3.145
Mode 00047	-0.31801	-6.64369	1.057	0.0478	3.145
Mode 00050	-0.7313	0.428653	0.068	0.8627	1.3675
Mode 00051	-0.7313	-0.42865	0.068	0.8627	1.3675

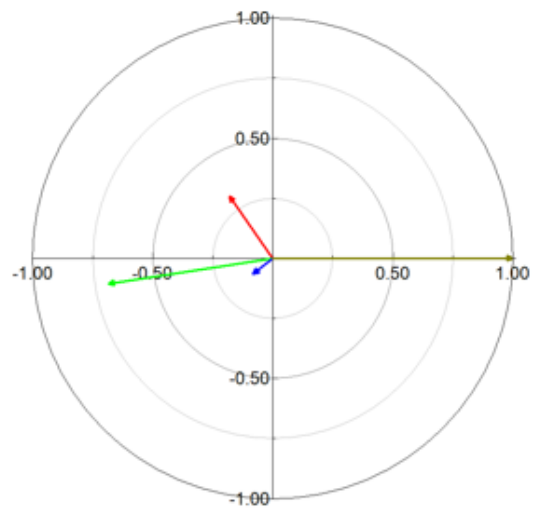
5.2.1 Participation Factor Analysis of New Modes

Figure 5-3 shows the participation factor analysis of the modes added by the wind generation. Figures 5-3 (a) and (b) show Modes 31 & 32 and 33 & 34 which are both sub synchronous oscillations since they have frequencies above 2 Hz. These are a result of the wind generator parameters oscillating against each other. In both cases, the wind generator synchronous reactance in the q and d axis, (X_{qr} and X_{dr}), (a) and (b) respectively, are oscillating against other parameters in the generator.

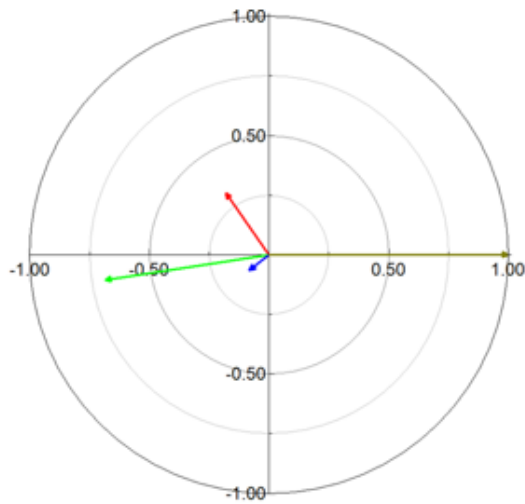
Modes 37 & 38 and 39 & 40, represented by (c) and (d), which are local modes, indicate that the synchronous reactance of the generator is oscillating against the active power controller of the wind turbines.



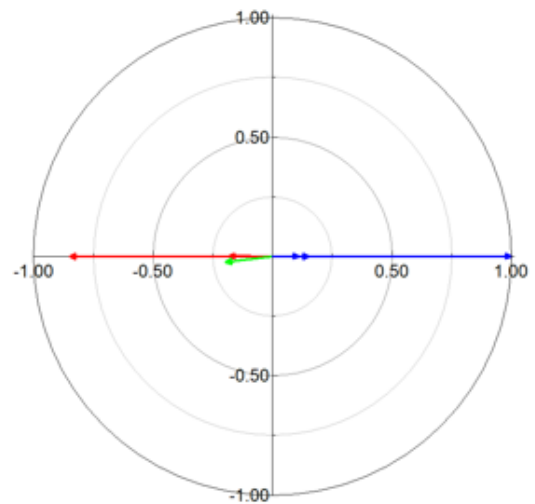
(a) Mode pair 31



(b) Mode pair 33



(c) Mode pair 37



(d) Mode pair 39

Figure 5-3 Participation factor of added modes

5.2.2 Time Domain Analysis

Time domain analysis is used to verify the results obtained from the modal analysis. Figure 5.4 shows that including a wind farm increases the oscillations of the overall system, therefore the damping of the systems worsens. This is due to the addition of new modes that are introduced by the wind farm.

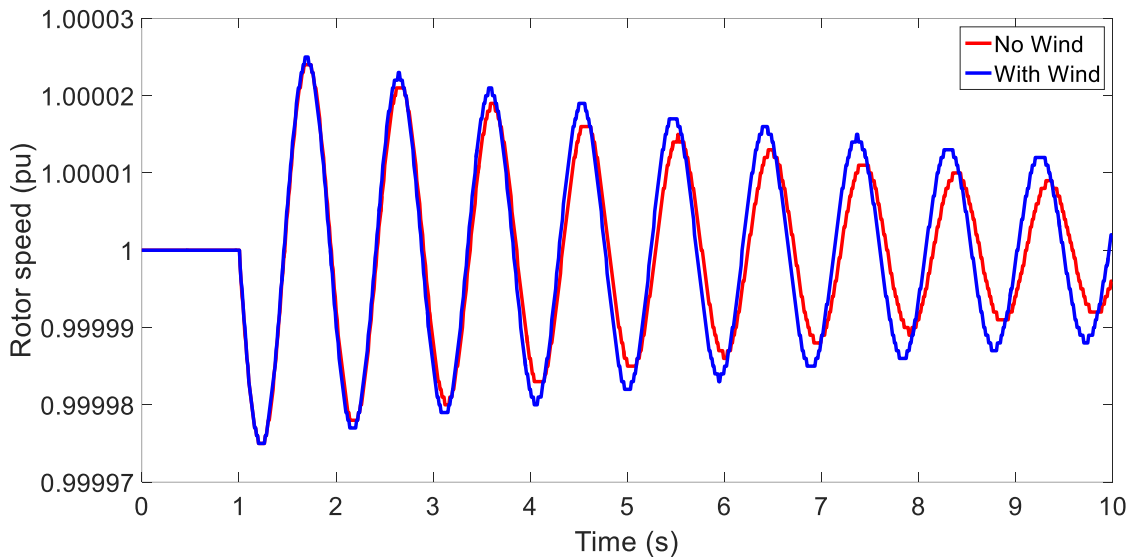


Figure 5-4 Time domain comparison with and without wind power generation

5.3 THE EFFECT OF SCR ON SMALL SIGNAL STABILITY

Nine oscillatory pairs are observed in the monopolar VSC-HVDC network. The majority stem from the controllers. As the short circuit ratio (SCR) of the AC grid increases, modes 18 & 19 and 22 & 23 begin to move further away from the imaginary axis; i.e., the real component of the modes became more negative and hence more stable. This is illustrated in Figure 5-5. This means that as the AC system becomes stronger, the stability of these modes improves. A SCR of less than 2 is considered low and hence the AC grid is very weak. A SCR between 2 and 3 is low, and one greater than 3 is considered strong. The Eigen trajectory indicates a rapid movement of the modes as the system improved from very weak, to weak, and continues moving consistently as the AC grid became stronger. Figure 5-5 illustrates the distribution of the nine mode pairs and their eigenvector trajectories with change in SCR. Modes 18 & 19 and 22 & 23 are observed to be control modes, having frequencies of 405 Hz and 82 Hz respectively. The other seven mode pairs in the system are unaffected by the strength of the AC grid.

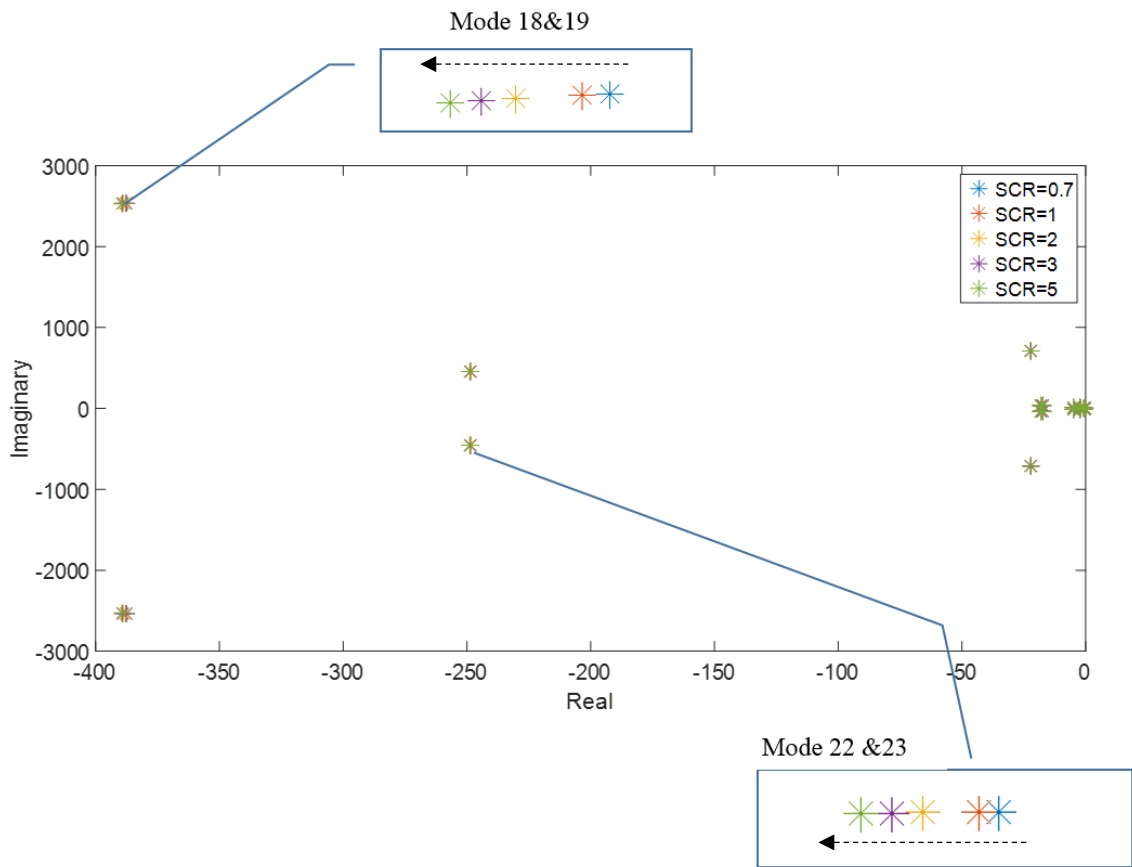


Figure 5-5 Effect of Change in SCR on Eigenvector Trajectory

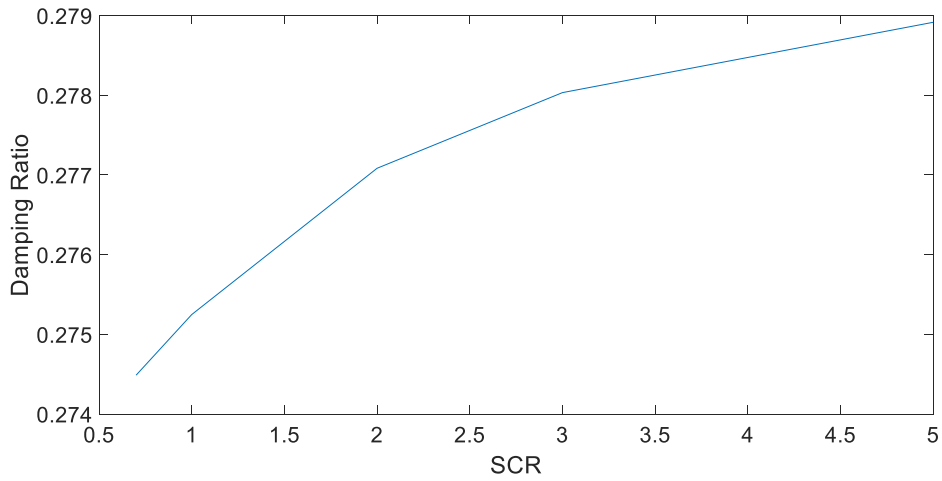


Figure 5-6 Effect of change in SCR on Damping Ratio of modes 18 & 19

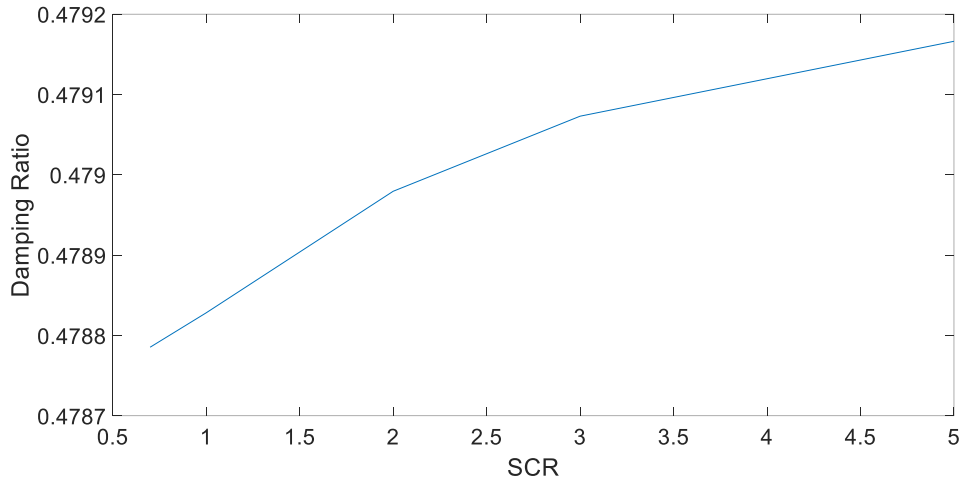


Figure 5-7 Effect of change in SCR on Damping Ratio of modes 22 & 23

Figures 5-6 and 5-7 indicate that the damping ratios of modes 18 & 19 as well as 22 & 23 responded in a similar pattern as the SCR of the AC grid increases. Both modes are well damped, but mode 22 & 23 are better damped than 18 & 19. The damping ratios of these modes improve as the AC system becomes stronger. The graphs becomes less steep as the AC grid changes from being very weak, to weak and then strong. This means that as the SCR continues increasing, the effect it had on the damping ratio of these modes lessen. This shows that once the AC system is strong, further strengthening will have little effect on the damping.

5.4 EFFECT OF CHANGE IN INNER (CURRENT) CONTROLLER GAIN

Figure 5-8 shows that when the current controller gain is increased, modes 18 & 19 move towards the imaginary axis and hence becomes less stable with an increase in gain. Since the gain is increased in smaller steps, the rate of movement of the mode is initially very fast, and then slows down at larger gain values. The same is true for modes 22 & 23. An increase in current controller gain, however, shows that 22 & 23 move away from the imaginary axis. As the gain increases, the mode becomes more negative and hence more stable. As observed with the effect of SCR, changing the inner current controller gain had no effect on the other modes.

The damping ratio of modes 18 & 19 reduces as the gain increases, whereas that of modes 22 & 23 increases as the gain increases. Figures 5-9 and 5-10 show that from gain 5 upwards, the rates of increase and decrease drastically slows down. Higher current controller gains do not have a significant impact on the small signal stability of the network.

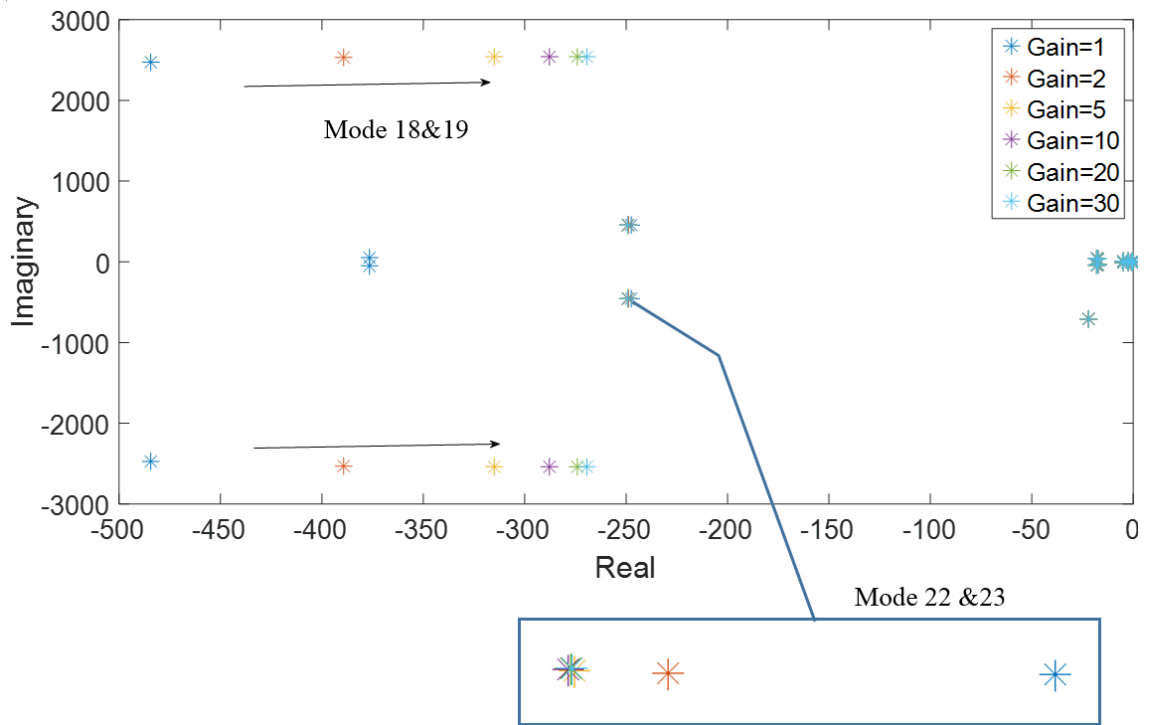


Figure 5-8 Effect of Varying Inner Current Gain

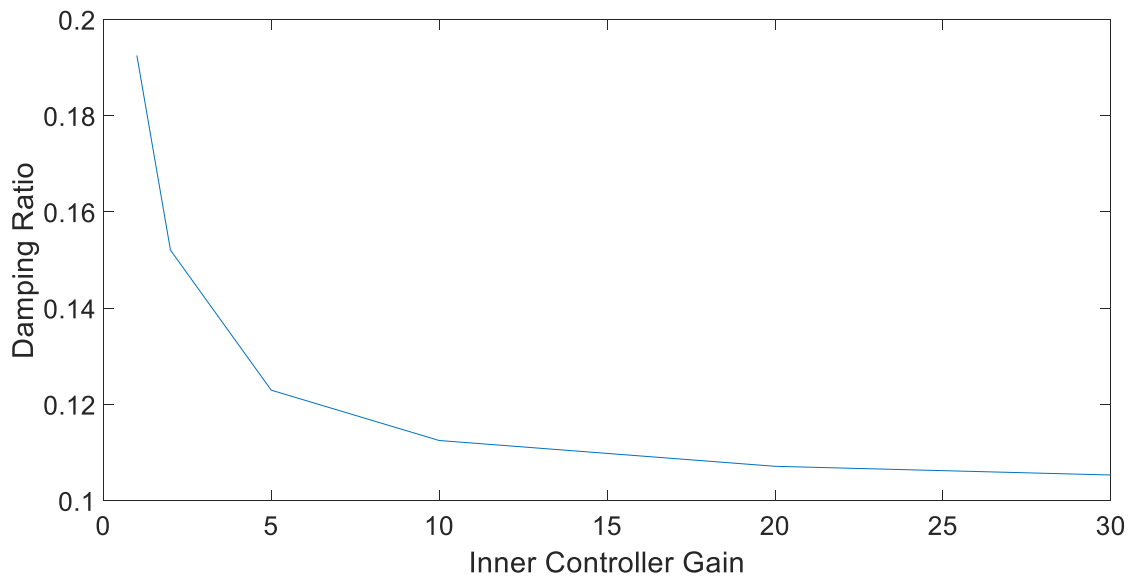


Figure 5-9 Effect of varying Inner Current Controller Gain on Modes 18 & 19

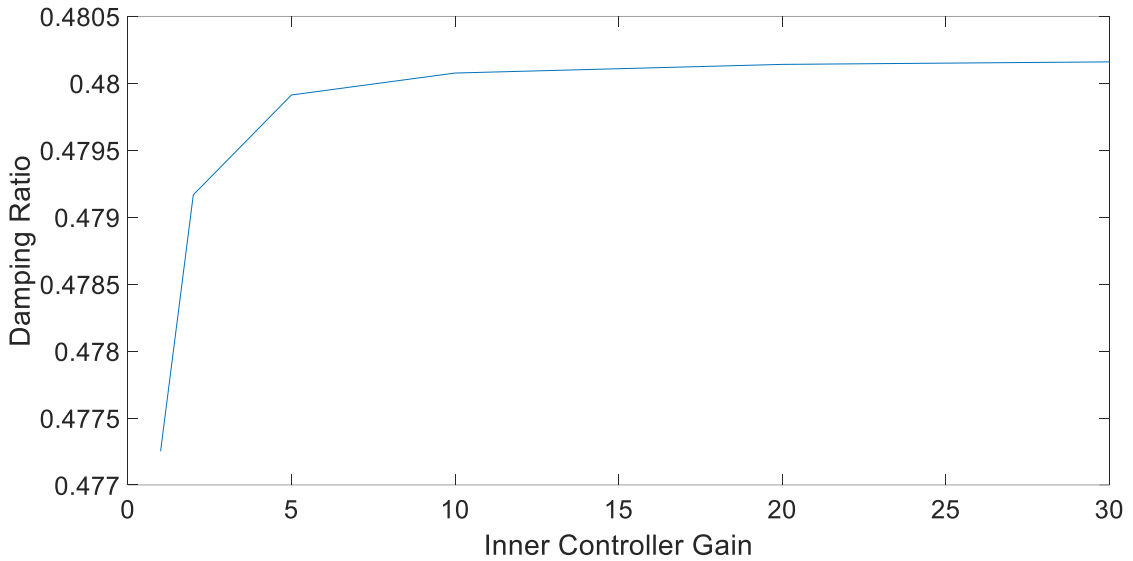


Figure 5-10 Effect of varying Inner Current Controller Gain on Modes 22 & 23

5.5 EFFECT OF OUTER (DC VOLTAGE) CONTROLLER GAIN

Figure 5-11 indicates that varying the outer controller gain also only has effects on modes 18 & 19 as well as 22 & 23. Modes 18 & 19 become more stable as the gain increases, the fastest movement being seen at increases in the smaller gain values. Modes 22 & 23 move towards the imaginary axis as the controller gain increases and therefore becomes unstable. The rate at which it is becoming unstable begins to slow down at the much higher gain values. An extra mode pair, 26 & 27 is observed at the lower gain values and disappeared at gain 5 and beyond. The damping of modes 18 & 19 was increasing as the gain was increasing until it reached its peak damping, after which it started decreasing with increasing gain as shown in Figure 5-12.

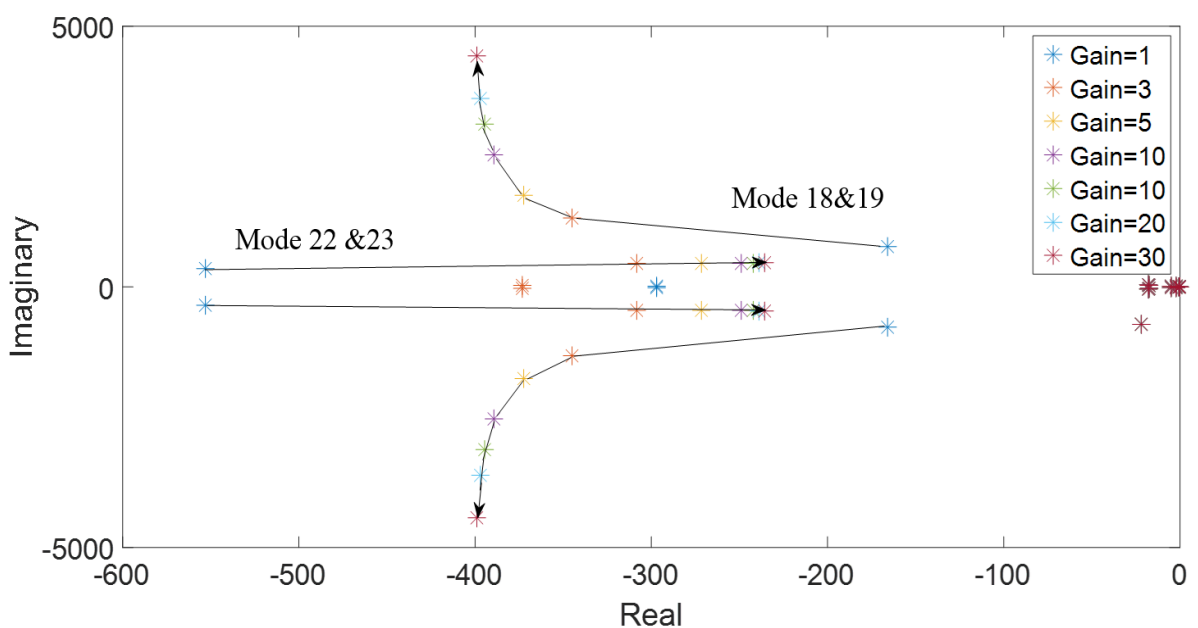


Figure 5-11 Effect of varying Outer Controller Gain

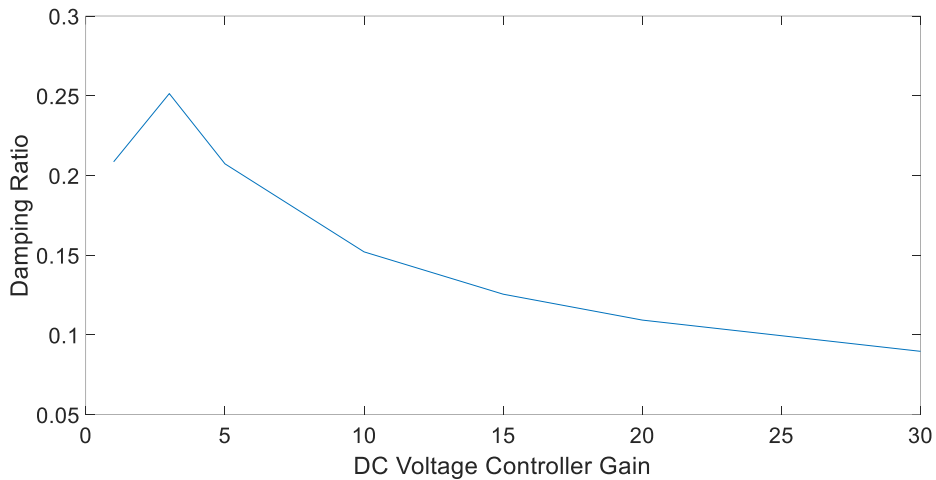


Figure 5-12 Effect of varying Outer Controller Gain on modes 18 & 19

For modes 22 & 23, and increase in outer controller gain sees a decrease in damping. The drop in damping ratio is quite sharp before gain 5 and thereafter starts decreasing at a slower rate as shown in Figure 5-13. As the higher value gains continue to increase, they have little effect on the damping ratio.

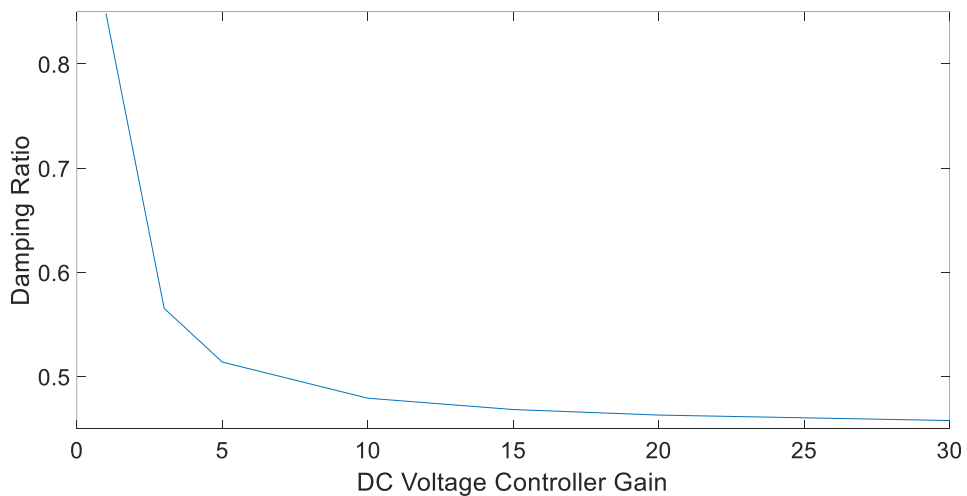


Figure 5-13 Effects of varying Outer Controller Gain on modes 22 & 23

5.6 EFFECT OF VARYING WIND POWER OUTPUT

In this section the wind power is varied. The MVA rating of the generation source is kept constant as the generator dispatch is varied. Increasing the output active power of the wind farm has different effects on different modes. Even the modes that are not affected in previous scenarios are affected by change in wind output power. The only mode that is unaffected by this condition was mode pair 20 & 21. This mode pair has the lowest damping ratio of 0.031 and remains so at all values of wind power output. Mode pair 37 & 38 also have a low damping ratio compared to the other modes and therefore this mode is critical to observe. As the wind output power increases,

this mode became more stable and its damping also improves as shown in Figure 5-14. Modes 46 & 47 are well damped, but have a lower damping ratio compared to the others and this ratio decreases as the wind power output increases. This is not of any concern because even though the damping ratio is lower than of the other modes, it is not critically low. Figure 5-15 shows the effects of wind power change on several different modes.

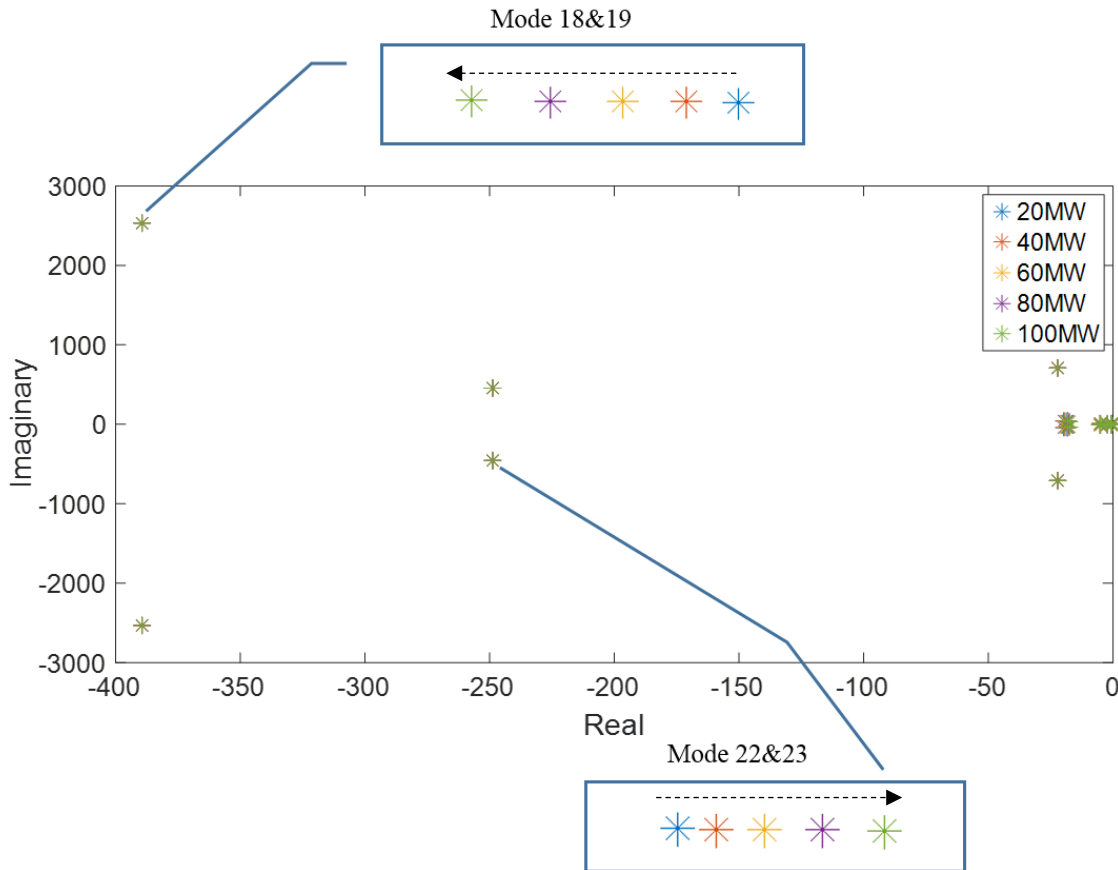


Figure 5-14 Effect of varying wind speed

It can also be observed that wind power output levels 20 MW, 40 MW and 60 MW have an extra mode pair which are not present in the other levels of output power. This mode pair, however poses no concern because it is well damped, having a damping ratio of 0.67. The frequency of this mode pair is 0.023 Hz making it an inter-area mode, signifying that the wind farm generators are swinging against the main generators.

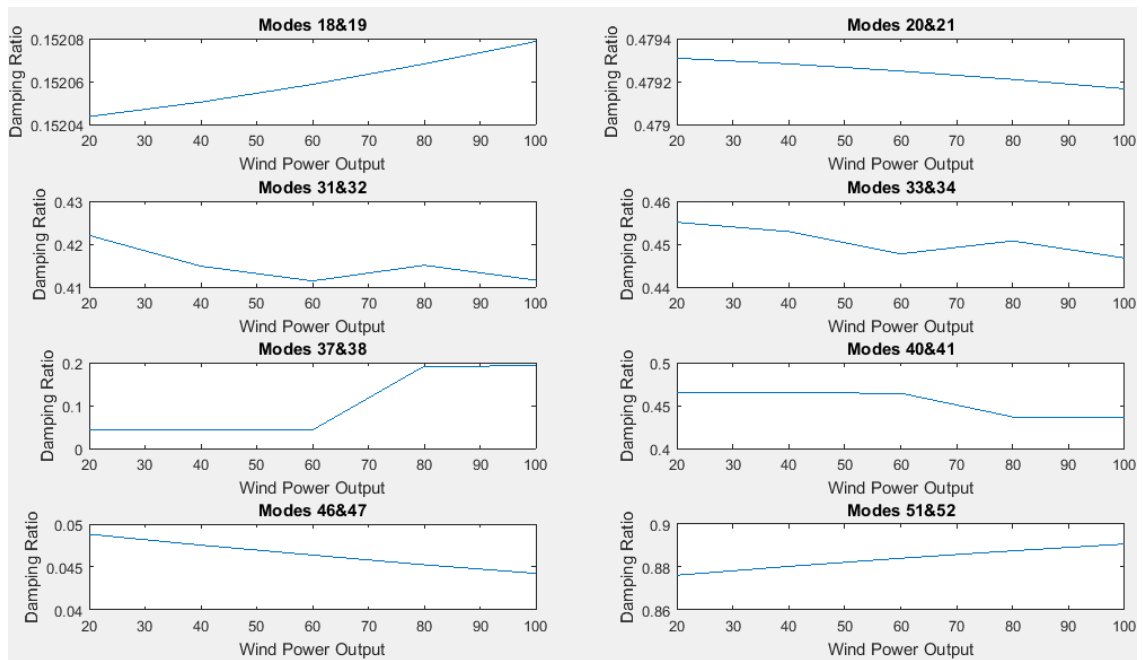


Figure 5-15 Effect of Wind Power Output on Damping Ratio of different modes

5.7 EXPANSION OF THE MONOPOLE TO A BIPOLE VSC-HVDC NETWORK

To investigate bipolar operation, a modal analysis is carried out here on the VSC-HVDC bipolar extension shown in Appendix A-5. This has a SCR of 5 and a small load increase of 20 % load used done in order to excite the oscillatory modes to trigger. The network is found to have 22 oscillatory modes of 11 pairs as shown in Figure 5.16 and Table 5.2. The eigenvalues in the expansion have similar modes in corresponding locations on the other half of the bipole. The oscillatory modes, as with the monopole, consist of sub-synchronous oscillations as well as electromechanical oscillations. All the modes have negative real parts and hence the system is stable. Mode pairs 45 & 46 and 47 & 48 have the lowest damping ratios of 4.3 % and 5.7 % respectively. These are local area oscillations because their damping frequencies are 1.74 Hz and 1.13 Hz which means that the main generator is oscillating against the rest of the system. The other oscillatory modes are quite well damped.

Table 5-2 Eigenvectors of bipole expansion

Mode	Real Part [σ]	Imaginary Part [$j\omega$]	Damped Frequency [Hz]	Damping Ratio	Damping Time [s]
Mode 00020	-338.183	1275.713	203.036	0.256	0.00296
Mode 00021	-338.183	-1275.71	203.036	0.256	0.00296
Mode 00022	-338.096	1265.541	201.417	0.258	0.00296
Mode 00023	-338.096	-1265.54	201.417	0.258	0.00296
Mode 00024	-253.13	509.5695	81.10051	0.445	0.00395
Mode 00025	-253.13	-509.57	81.10051	0.445	0.00395
Mode 00027	-256.826	507.7669	80.81362	0.451	0.00389
Mode 00028	-256.826	-507.767	80.81362	0.451	0.00389
Mode 00040	-17.959	39.94516	6.35747	0.410	0.05568
Mode 00041	-17.959	-39.9452	6.35747	0.410	0.05568
Mode 00042	-18.4622	37.43073	5.957286	0.442	0.05416
Mode 00043	-18.4622	-37.4307	5.957286	0.442	0.05416
Mode 00045	-0.47254	10.94439	1.741854	0.0431	2.11620
Mode 00046	-0.47254	-10.9444	1.741854	0.0431	2.11620
Mode 00047	-0.40698	7.109501	1.131512	0.0572	2.45710
Mode 00048	-0.40698	-7.1095	1.131512	0.0572	2.45710
Mode 00049	-5.30576	10.11894	1.610479	0.4643	0.18847
Mode 00050	-5.30576	-10.1189	1.610479	0.464	0.18847
Mode 00059	-0.7681	0.470824	0.074934	0.853	1.30192
Mode 00060	-0.7681	-0.47082	0.074934	0.853	1.30192
Mode 00063	-0.13468	0.147398	0.023459	0.675	7.42513
Mode 00064	-0.13468	-0.1474	0.023459	0.675	7.42513

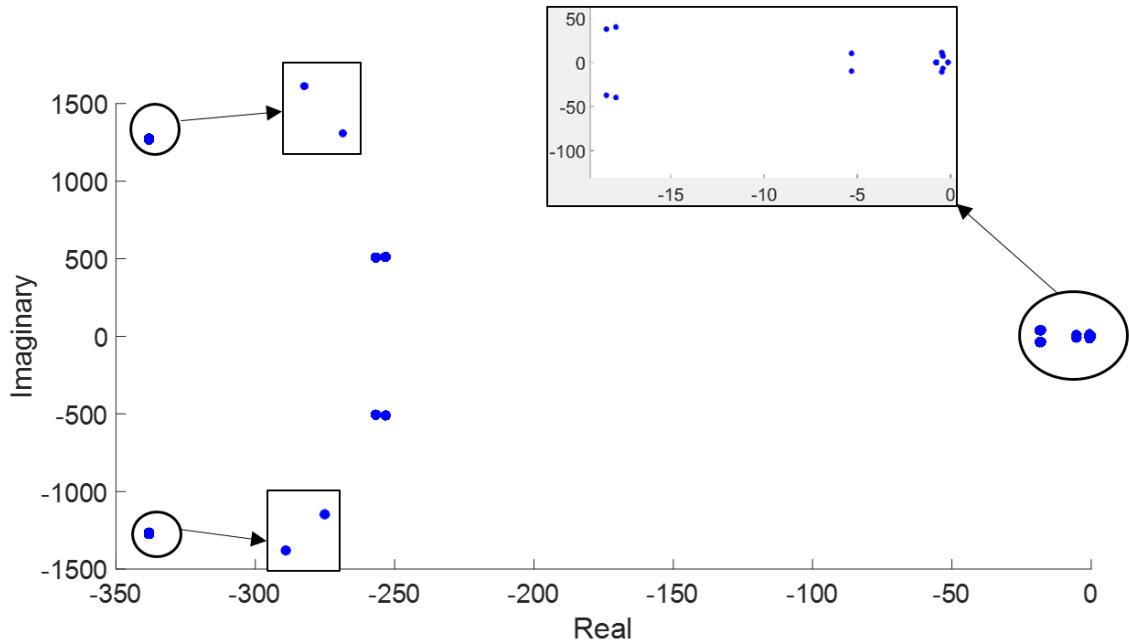


Figure 5-16 Eigenvalues for Bipole expansion

5.8 EFFECT OF SCR ON SMALL SIGNAL STABILITY

In this section the effects of change in short circuit ratio are investigated. A change in short circuit ratio has an effect on four of the eleven mode pairs; 20 & 21, 22 & 23, 24 & 25 and 27 & 28. Figure 5-17 shows the eigenvector trajectory of these modes. The pairs 20 & 21 and 22 & 23 are the same point on the corresponding half of the bipolar system. This is the same for mode pairs 24 & 25 and 27 & 28. These modes, as expected, behave in a similar manner; i.e, they have similar damping ratios at the different values of SCR. Mode pair 20 & 21 move further away from the imaginary axis as the system becomes stronger and therefore becomes more stable. This is also the case for mode pair 24 & 25. The change in SCR only has a very slight, almost negligible effect on the movement of the other two pairs as shown in Table 5.3. Figure 5-17 shows that the rate at which the eigenvectors are moving away from the imaginary axis is very slow, as indicated by the very minimal gaps between the modes. The very small changes in damping ratio in Table 5-3 confirm this.

The change in SCR, however, has no effect on poorly damped local area electromechanical modes. Table 5.3 shows that these modes, even though they are affected by a change in SCR, are very well damped and overall posed no concern on the system stability

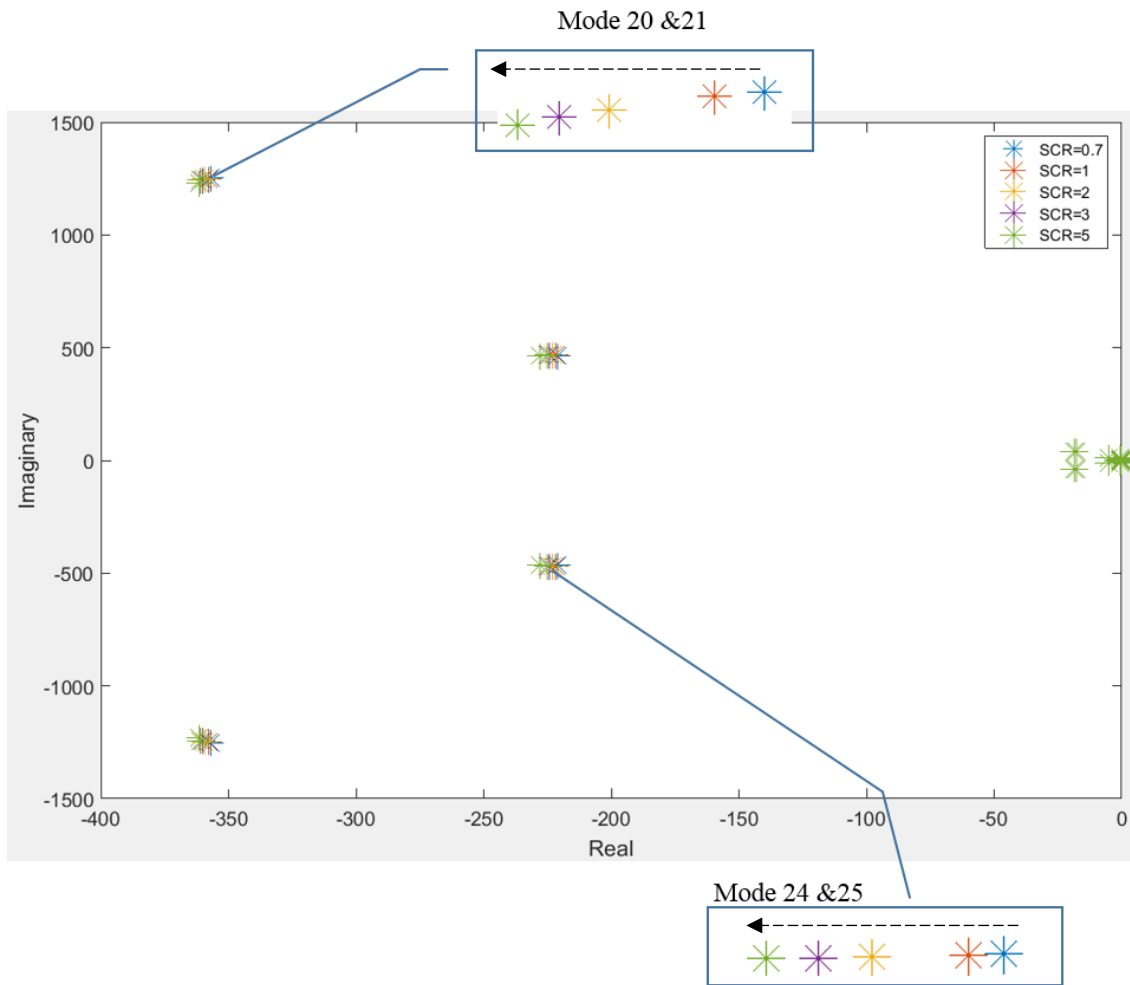


Figure 5-17 Effect of change in SCR on Eigenvectors

Table 5-3 Effect of SCR on Damping Ratio

Mode \ SCR	0.7	1	2	3	5
20 & 21	0.274	0.275	0.277	0.278	0.279
22 & 23	0.282	0.282	0.282	0.282	0.282
24 & 25	0.429	0.429	0.431	0.432	0.434
27 & 28	0.439	0.439	0.439	0.439	0.439

5.9 EFFECT OF INNER CURRENT CONTROLLER GAIN

In this section the effects of inner current controller gain are investigated. As observed with a change in SCR, only four mode pairs are affected by a change in inner current controller gain. Mode pairs 20 & 21 and 22 & 23 are affected significantly. These modes rapidly move away from the imaginary axis as the gain is increased from Gain = 1 to Gain = 2 and then when the gain is increased from Gain = 2 to Gain = 5 they rapidly move towards the imaginary axis. This is shown in Figure 5-18 and confirmed by the actual eigenvector coordinates in Table 5-4. Any further

increase from Gain = 5 either has no effect on the movement of the mode or the movement is very minimal, especially at the higher values of gain. Gain = 2 is the furthest from the imaginary axis, and hence this the best gain value for the inner current controller for the greatest stability. Mode pairs 24 & 25 and 27 & 28, are effected by the change in gain values, but this effect is insignificant since the modes do not deviate much from their original position, and at the higher gain values, do not move at all.

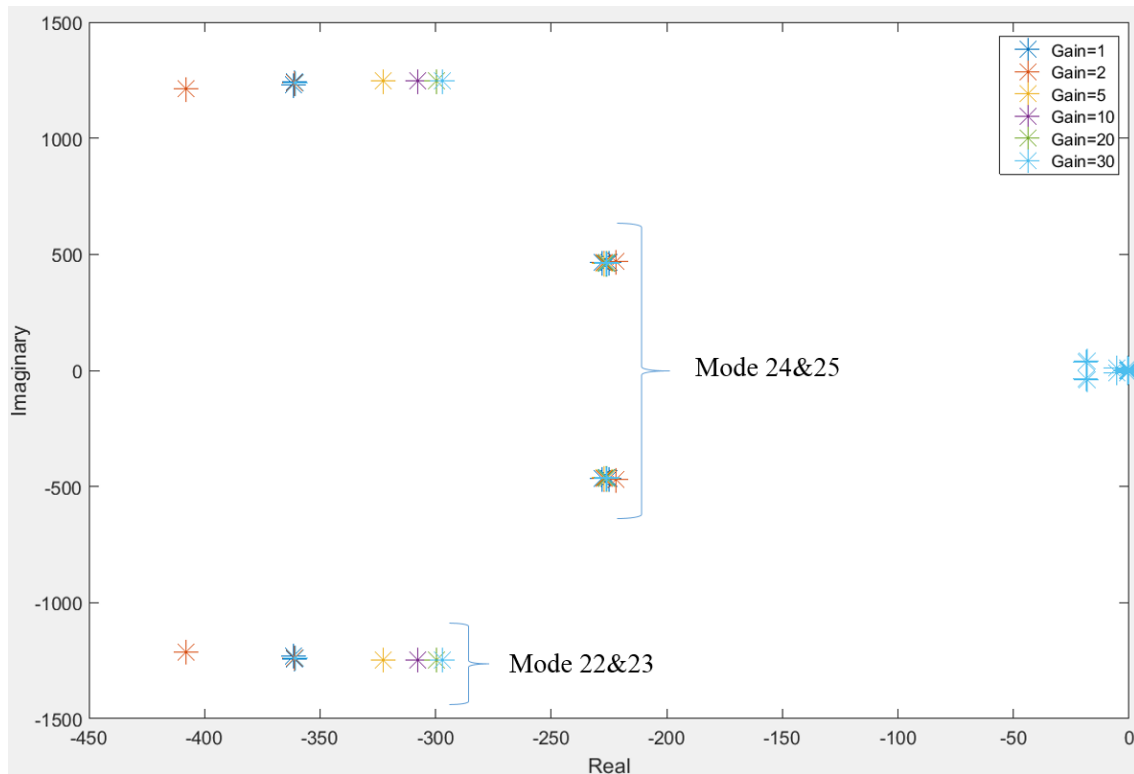


Figure 5-18 Effect of Varying Inner Current Controller Gain

Table 5-4 Eigenvectors of Modes affected by change in Inner Current Controller Gain

Gain \ Mode	1	2	5	10	20	30
20 & 21	$-360 \pm j1243$	$-361 \pm j1238$	$-322 \pm j1245$	$-308 \pm j1247$	$-299 \pm j1248$	$-297 \pm j1248$
22 & 23	$-362 \pm j232$	$-408 \pm j1214$	$-360 \pm j1237$	$-360.7 \pm j1237$	$-360.8 \pm j1243$	$-360.8 \pm j1243$
24 & 25	$-225 \pm j467$	$-222 \pm j472$	$-226 \pm j467$	$-226 \pm j467$	$-226 \pm j467$	$-226 \pm j467$
27 & 28	$-228 \pm j466$	$-227 \pm j472$	$-227 \pm j462$	$-226 \pm j460$	$-226 \pm j460$	$-226 \pm j460$

Table 5-5 shows that all the affected modes are very well damped despite the inner current controller gain value. As shown by the movement of the eigenvectors, the highest damping ratio for mode pairs 20 & 21 and 22 & 23 is at Gain = 2, which is where mode pairs 24 & 25 and 27 & 28 experience their lowest damping ratio, as illustrated in Table 5-5. Even though this is the lowest damping ratio for the latter modes, it is not far off from the damping ratios for the other gain values. For all the mode pairs, a change in inner current controller gain has little or no effect at higher values of the gain. Mode pairs 45 & 46 and 47 & 48, which have the lowest damping ratios in the system, are still unaffected by this condition.

Table 5-5 Effects of Varying Current Controller Gain on Damping Ratio

Gain Mode	1	2	5	10	20	30
20 & 21	0.279	0.280	0.251	0.239	0.234	0.232
22 & 23	0.282	0.319	0.280	0.280	0.280	0.280
24 & 25	0.434	0.426	0.436	0.436	0.436	0.436
27 & 28	0.439	0.437	0.441	0.441	0.441	0.441

5.10 EFFECT OF OUTER CONTROLLER GAIN

The widely dispersed modes at different settings of the outer (DC) controller gain in Figure 5-19 shows how significant an impact this condition has on the oscillatory modes. This shows that every change in gain results in the rapid movement of the modes. All four mode pairs are affected by the change in outer controller gain as shown by their eigenvectors in Table 5.6. Mode pair 20 & 21 are unaffected by the lower gains. This is shown by the effect on the damping ratio in Table 5-6. However, an increase of gain beyond Gain = 10 sees rapid movement of the mode pair away from the imaginary axis, hence becoming more stable. When the outer controller gain is increased at the lower gain values, mode pair 22 & 23 rapidly move away from the imaginary axis and become more stable until Gain = 10. It can be seen from Table 5-7 that a very low gain value, the damping ratio is 0.099, which is quite low. Further increase in gain after Gain = 10 has very slight or no effect on the movement of the mode. This further increase therefore has no effect on damping ratio.

Modes 24 & 25 are least affected by change in the low and extremely high gain values. As the gain is increased, the pair move closer to the imaginary axis, becoming less stable. The biggest shift of the mode occurs from Gain = 3 to Gain = 5, and then from Gain = 5 to Gain = 10, where the damping ratio drops from 89.7 % to 68.9 % and then to 43.4 % respectively. Mode pair 27 & 28 slightly shifts away from the imaginary axis at Gain=10 where the damping ratio was at its peak value of 43.9 %. It can be concluded that Gain = 10 is the best gain for the maximum level of system stability.

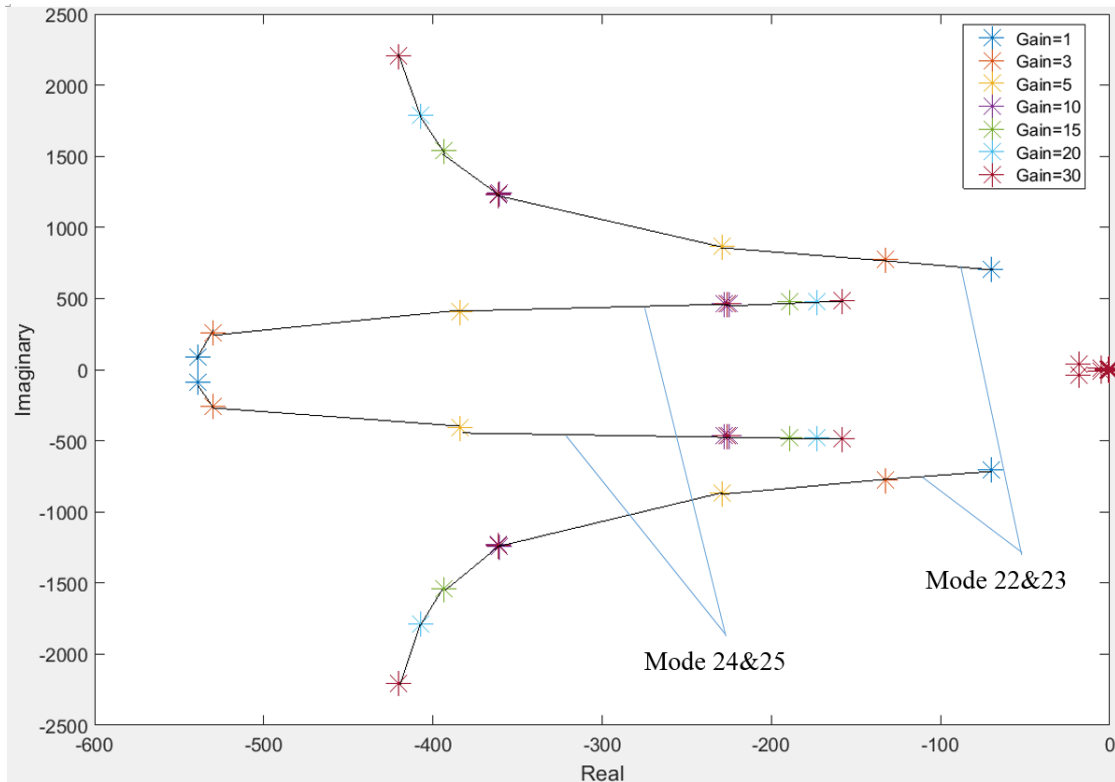


Figure 5-19 Effect of Varying Outer Controller Gain

Table 5-6 Eigenvectors of Modes affected by change in Outer Controller Gain

Gain \ Mode	1	3	5	10	15	20	30
20 & 21	$-361 \pm j1238$	$-361 \pm j1238$	$-361 \pm j1238$	$-361 \pm j1243$	$-393 \pm j1538$	$-407 \pm j1788$	$-420 \pm j2203$
22 & 23	$-70 \pm j703$	$-132 \pm j773$	$-229 \pm j871$	$-362 \pm j1232$	$-361 \pm j1237$	$-361 \pm j1238$	$-361 \pm j1238$
24 & 25	$-539 \pm j87$	$-530 \pm j260$	$-384 \pm j404$	$-225 \pm j467$	$-189 \pm j475$	$-173 \pm j479$	$-158 \pm j482$
27 & 28	$-226 \pm j467$	$-226 \pm j467$	$-226 \pm j467$	$-227 \pm j466$	$-226 \pm j467$	$-226 \pm j466$	$-226 \pm j466$

Table 5-7 Effects of Varying Outer Controller Gain on Damping Ratio

Gain \ Mode	1	3	5	10	20	15	30
20 & 21	0.280	0.280	0.280	0.279	0.248	0.222	0.187
22 & 23	0.099	0.169	0.254	0.282	0.280	0.280	0.280
24 & 25	0.436	0.436	0.436	0.439	0.436	0.436	0.436
27 & 28	0.987	0.897	0.689	0.434	0.370	0.340	0.312

5.11 EFFECT OF WIND POWER OUTPUT

Section 5.6 addressed the variation of wind power output in the monopole configuration, whereas this section addresses the bipole. A change in wind power output does not have an effect on the high frequency oscillations. Their damping ratios remain unchanged at all values of wind power output. However, the electromechanical modes are affected, including mode pairs 45 & 46 and 47 & 48 which are the most poorly damped modes in the system. This effect was not seen in the previous scenarios which investigated controller gain and SCR; which had no effect on these badly damped modes. This means that these modes have to be closely monitored at different levels of wind power because they are so close to the imaginary axis, as shown in Figure 5-20 and Table 5-8. Irregular and inconsistent wind energy is important to observe in terms of the system stability.

Table 5-8 Eigenvectors of the poorly damped modes

Mode \ MW	20	40	60	80	100
45 & 46	$-0.467 \pm j10.9$	$-0.468 \pm j10.9$	$-0.470 \pm j 0.9$	$-0.471 \pm j10.9$	$-0.473 \pm j10.9$
47 & 48	$-0.424 \pm j7.07$	$-0.419 \pm j7.08$	$-0.415 \pm j7.09$	$-0.411 \pm j7.10$	$-0.407 \pm j7.11$

Mode pair 47 & 48 is the more sensitive of the two as shown by the rapid movement of the modes in Figure 5-20. As the output wind power increases, this pair move closer to the imaginary axis. Modes 45 & 46, on the other hand, move slightly away from the imaginary axis as the output wind power increases. Table 5-9 shows how the damping ratios of these two mode pairs change as the wind power output changes. This confirms that mode pair 45 & 46 has its highest damping at higher wind power output levels, and mode pair 47 & 48 has its highest damping at lower wind power output levels.

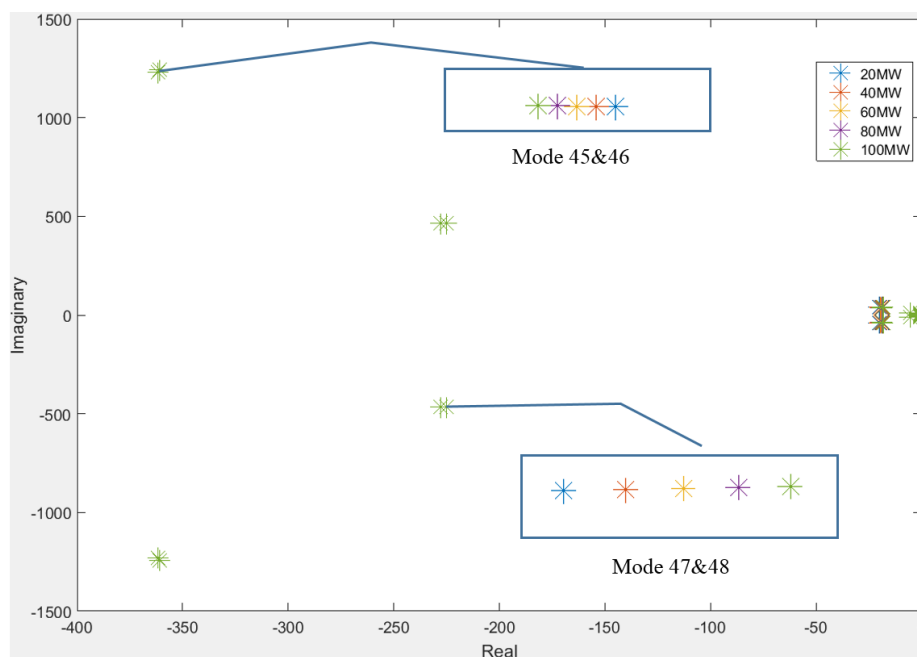


Figure 5-20 Effect on Varying Wind Power Output of Eigenvector Trajectory

Table 5-9 Damping Ratios of the poorly damped modes at different levels of wind power output

MW Mode	20	40	60	80	100
45 & 46	0.0426	0.0428	0.0429	0.0430	0.0431
47 & 48	0.0599	0.0591	0.0584	0.0578	0.0572

5.12 COMPARISON: MONOPOLE AND EXPANSION TO BIPOLE

5.12.1 Time domain Analysis

Figure 5-21 shows that both systems, both excited by a 20% load increase which served a disturbance, are not well damped since their settling times are high and they have not settled by the end of the 10 s simulation time. The oscillations for the monopole are higher in magnitude than those of the bipole expansion. This can be supported by the fact that even though the worst damped mode of the monopole has a 0.0478 damping ratio compared to the lowest of the bipole, having a 0.0431 damping ratio, the damping time of that mode has a much larger damping time of 3.14 s as opposed to 2.11 s for the bipole mode.

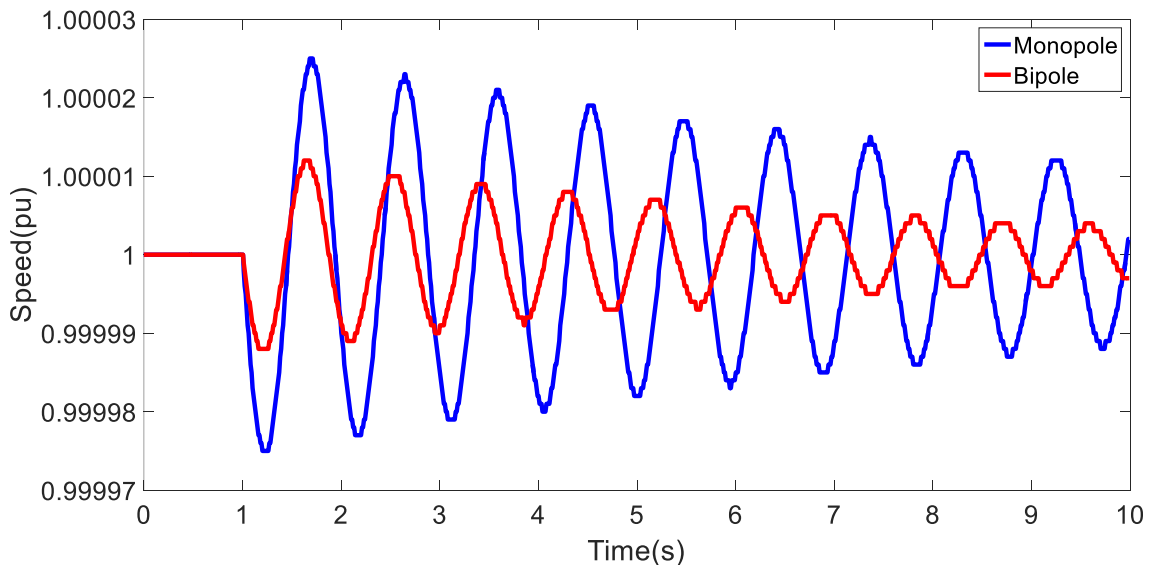


Figure 5-21 Time domain of monopole and bipole expansion rotor oscillations

5.12.2 Effects of Different conditions

The bipole expansion results in addition of modes in similar locations as the monopole base case. It can be seen in Figures 5-22 to 5-25 that the bipole expansion behaves in the same manner as the monopole system under the different conditions. For SCR variation, the monopole is more stable than the bipole expansion at higher real negative values as seen in Figure 5-22.

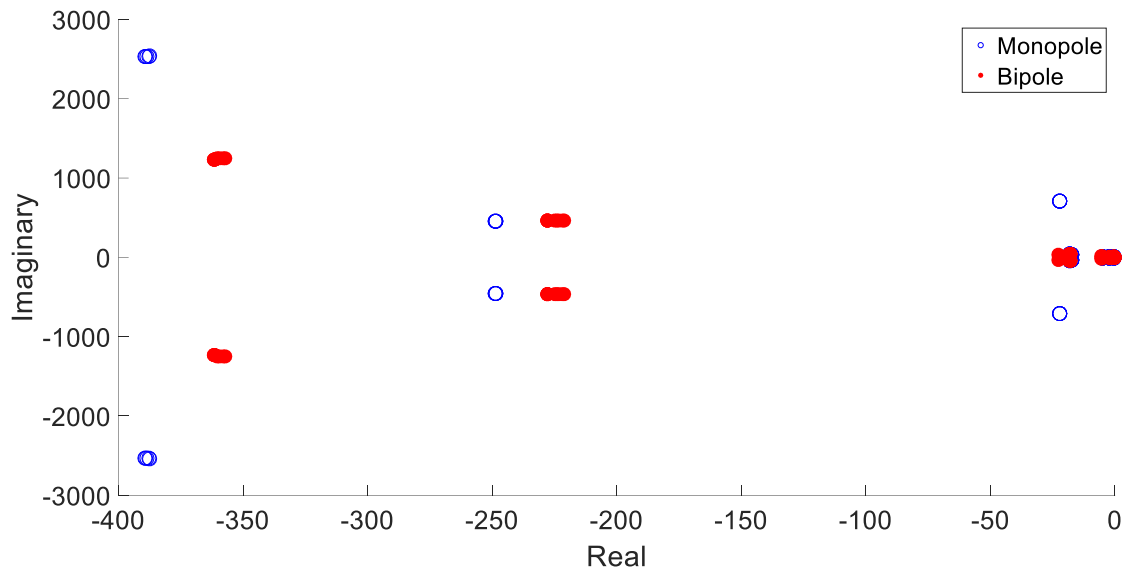


Figure 5-22 Monopole and Bipole Comparison with varying SCR

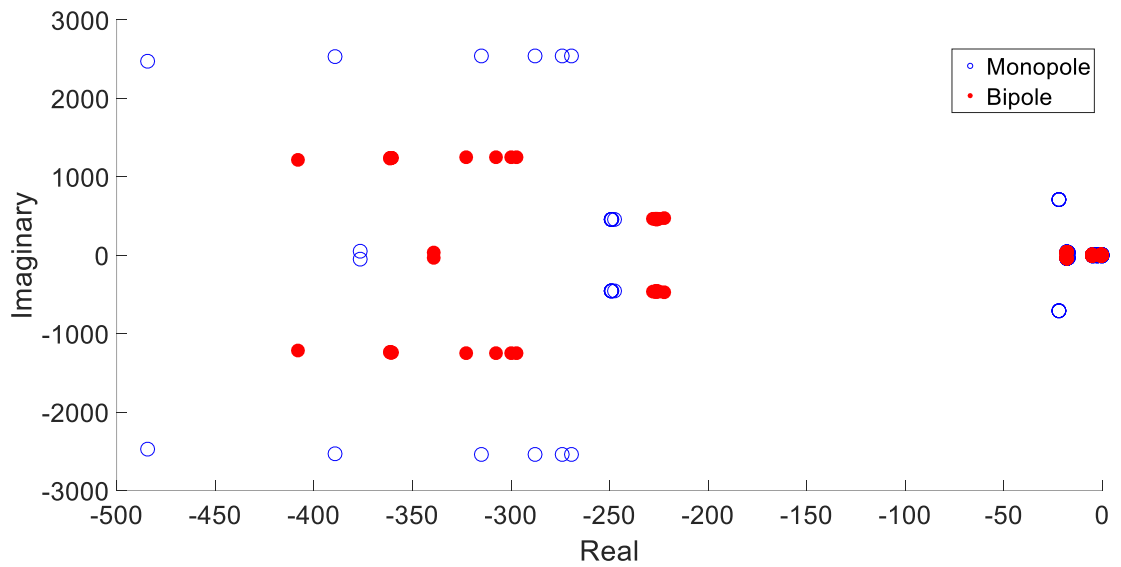


Figure 5-23 Monopole and Bipole Comparison with varying inner current controller gain

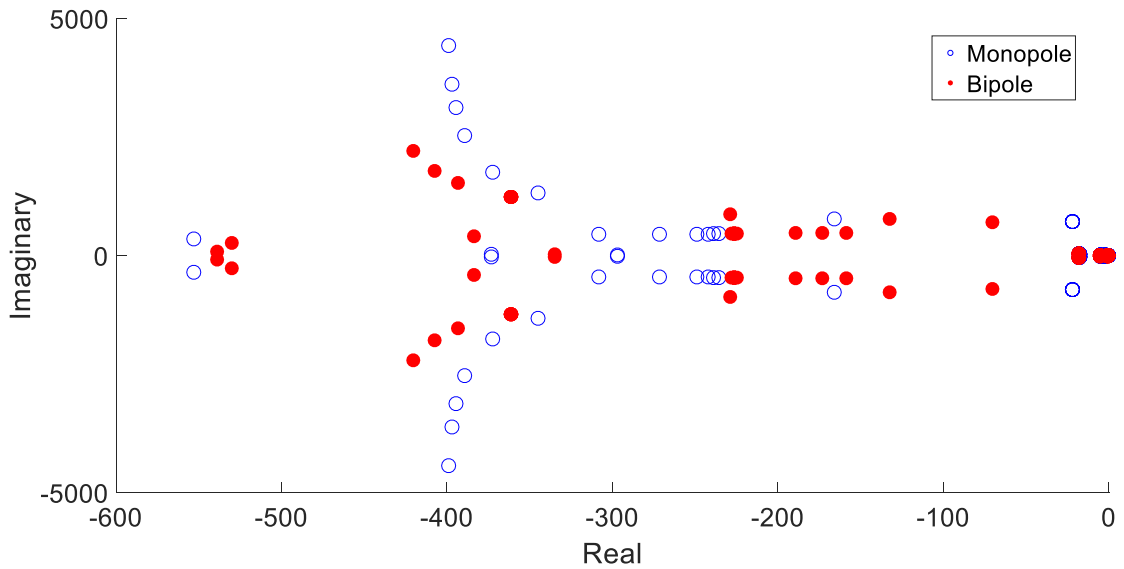


Figure 5-24 Monopole and Bipole Comparison with varying outer controller gain

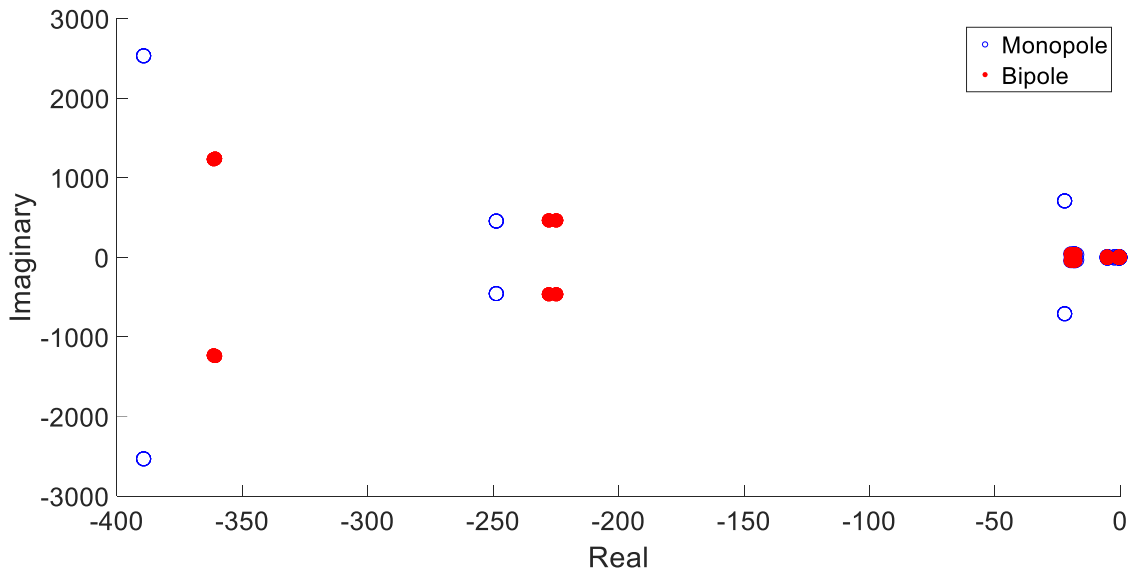


Figure 5-25 Monopole and Bipole Comparison with varying wind power output

5.13 POWER OSCILLATION DAMPING

This section looks at the design of a Power System Stabilizer (PSS) as well as a Thyristor Controlled Series Capacitor (TCSC) aimed specifically at improving electromechanical modes for both wind integrated Monopole and the Bipole configurations. The performance of the two power oscillation damping controllers are compared in these two configurations.

5.13.1 Power System Stabilizers

Power System Stabilizers (PSS) are the most common and most cost-efficient solutions to damping of electromechanical oscillations. They are installed in the excitation systems of synchronous generators [91] and add damping to the generator excitation rotor oscillations by

controlling its excitation using auxiliary stabilizing signals [75]. A PSS arrangement is shown in Figure 5-26. If excitation is controlled by means of an Automatic Voltage Regulator (AVR) without a PSS, the system becomes unstable. The inclusion of a PSS eliminates the negative effects of the AVR on the damping torque [92].

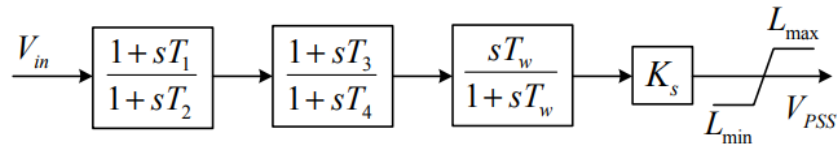


Figure 5-26 Classical PSS block diagram [90]

Lead-Lag Blocks: Addressing Figure 5-26. The PSS has phase compensation circuits to compensate for the phase lag between the exciter input and the electrical torque. In practice, two or more first order phase compensation blocks are used to attain the desired compensation. T_1 to T_4 are the time constants of the lead-lag blocks.

Wash out block: This is the third block in Figure 5-26. This serves as a high pass filter, having a time constant T_w ranging from 1 to 20 s. It is important for the prevention of steady variations in speed from the altering of the field voltage [93]. For local mode oscillations in the range of 0.8 to 2.0 Hz, a T_w value of 1.5 s is suitable. For inter-area oscillations, T_w can be 10 s or greater, since lower time constants result in considerable phase leads at low frequencies [75].

Stabilizer gain: This is the last block in Figure 5-26 and determines the amount of damping introduced by the PSS. Ideally, the gain should be set at a value that provides maximum damping. The value of gain is selected by investigating the effect on critical modes for a wide range of values without compromising the stability of other modes. The damping increases with increasing stabilizer gain up to a particular point, beyond which further increase in gain diminishes the damping. The PSS output is limited to avoid extreme magnitudes of the output signal. The transfer function of a Power System Stabilizer can be represented by

$$G_{PSS}(s) = \frac{V_{PSS}}{V_{in}} = K \left[\frac{1+sT}{1+s\frac{T}{\alpha}} \right]^N \left[\frac{sT_w}{1+sT_w} \right] \quad (5.1)$$

where N is the number of lead-lag blocks, $T = T_1 = T_3$ is the time constant, and $T_2 = T_4 = T\alpha$. α is the filtering ratio and T_w is the washout time constant.

5.13.2 Residue Based Tuning of the PSS

One method commonly used to tune Power System Stabilizers is the residue based method. Movement of the eigenvector λ can be described by

$$\Delta\lambda_i = R_i K G_i(\lambda_i) - \theta_R \quad (5.2)$$

where R is the residue of a particular mode i , which gives the measure of that mode's sensitivity to a feedback between the output and the input. G is the PSS transfer function [94]. The aim of a PSS is to improve the damping of the specific oscillatory mode. There are two parts to designing and tuning a power system stabilizer:

- i) Design of the Phase Compensator
- ii) Optimization of the PSS gain

5.13.3 Phase Compensator Design

The design of the lead compensator depends on the angle of the particular mode that requires improved damping.

- 1) The compensation angle is determined by

$$\theta_{PSS} = 180 - \theta_R \quad (5.3)$$

Given that θ_R is the residue angle.

- 2) The number of compensation blocks to be used is

$$N = \frac{\theta_{PSS}}{60^\circ} \quad (5.4)$$

The angle of compensation for each block should not exceed approximately 60° in order to minimize noise sensitivity at high frequencies and also due to limitations of the RLC circuit [95].

- 3) The filter ratio and time constant are

$$\alpha = \frac{1 - \sin\left(\frac{\theta_{PSS}}{N}\right)}{1 + \sin\left(\frac{\theta_{PSS}}{N}\right)} \quad (5.5)$$

$$T = \frac{1}{\omega_i \sqrt{\alpha}} \quad (5.6)$$

The time constants T_1 to T_4 are obtained from

$$T = T_1 = T_3 \quad (5.7)$$

$$T_2 = T_4 = \alpha T \quad (5.8)$$

5.13.4 Optimization of the PSS Gain

The stabilizer gain is carefully chosen by tracking the movement of the critical mode under investigation. When increasing the gain other modes may shift towards to the unstable complex plane. Therefore, care must be taken to observe the movement of the other modes while increasing the gain from zero. An appropriate PSS gain can be selected as 30 % to 50 % of the value when the system becomes unstable [96].

5.14 PSS DESIGN FOR MONOPOLE CONFIGURATION

Without the inclusion of the power system stabilizer and automatic voltage regulator, the oscillatory mode pair 46 & 47 are poorly damped, with a damping ratio of 4.78 % with the eigenvector position at $-0.318 \pm j6.643$. Although it is above 3 %, the damping should preferably be above 5 %.

A time domain analysis was carried out where an RMS simulation is run for 10 s and the rotor angle observed. There is a small disturbance in the system where the load is increased by 20 % at $t = 1.00$ s. Figure 5-27 shows the rotor angle oscillations of the main generator. The oscillations are reducing but at a very slow rate. This system is not unstable but, due to the fact that it is significantly underdamped, with time the generator shaft will become fatigued, and eventually the generator shaft will be damaged leading to its failure.

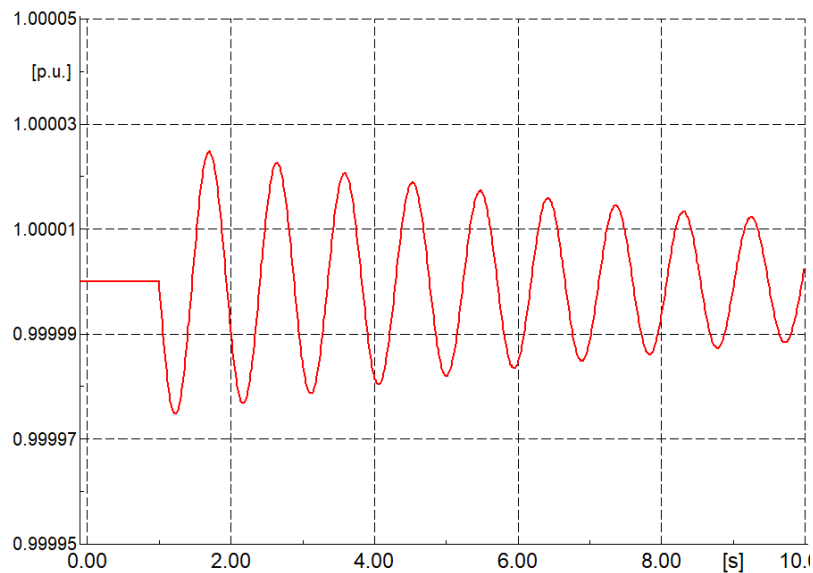


Figure 5-27 Rotor Speed without PSS and AVR



Figure 5-28 Power System Stabilizer of PSS

A power system stabilizer was added to the system to improve the damping of the mode at $-0.318 \pm j6.643$ which had a damping ratio of 0.0478 at a frequency of 1.057 Hz. This is shown in Figure 5-28. A lead compensator was designed using the process and criteria outlined in the methodology. The compensation angle was determined first:

$$\theta_{PSS} = 180 - 87.26 = 92.7^\circ$$

Each compensation block is only allowed a maximum of 60° therefore the number of compensation blocks was determined using (5.4). This gives

$$N = \frac{92.7^\circ}{60^\circ} = 1.55 \approx 2$$

The filter ratio was determined using (5.5) so that

$$\alpha = \frac{1 - \sin\left(\frac{92.7^\circ}{2}\right)}{1 + \sin\left(\frac{92.7^\circ}{2}\right)} = \frac{0.276}{1.724} = 0.160$$

The time constants T_1 to T_4 are determined using (5.6), (5.7) and (5.8):

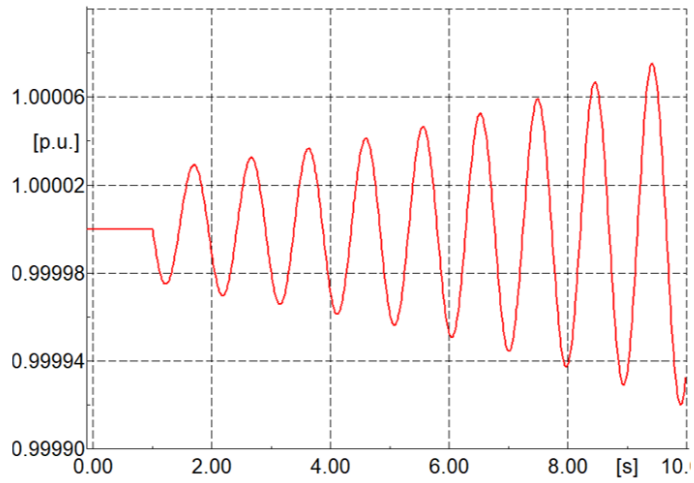
$$T = \frac{1}{2\pi(1.057)\sqrt{0.160}} = 0.379 \text{ s}$$

$$T = T_1 = T_3 = 0.379 \text{ s}$$

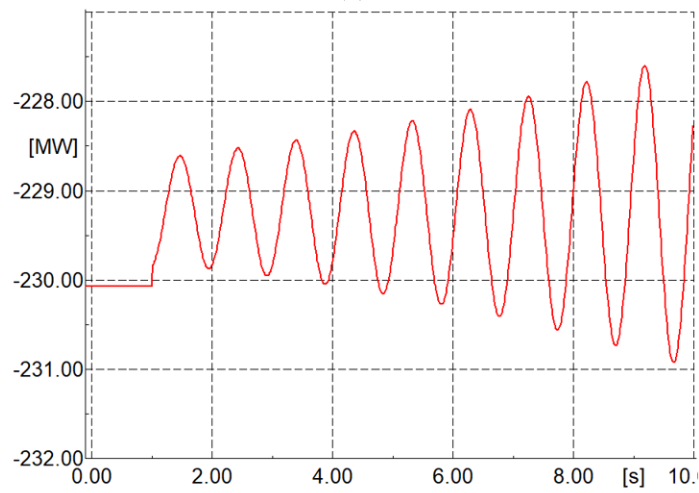
$$T_2 = T_4 = \alpha T = 0.160 \times 0.379 = 0.0606 \text{ s}$$

Optimization of the PSS Gain

The stabilizer gain is carefully chosen by tracking the movement of the critical mode under investigation. When increasing gain other modes may shift towards the unstable complex plane so that care must be taken to observe the movement of the other modes while increasing the gain from zero. When the PSS Gain is set to zero, it can be seen from Figure 5-29 that the oscillations has increasing amplitude and therefore the system is unstable. In order to determine the optimum gain for stability, this gain value is increased. Figures 5-30 to 5-33 show how increasing gain improves the settling time for the oscillations. The higher the gain value, the fewer the oscillation translating to an improved settling time. This was true until Gain = 40. Gain = 50 did not show any significant change in the settling time but a slight distortion begins to appear at about 1.5 to 2 s. This is initially only visible the AC active power graph. Distortion worsens as the gain further increases as shown in Figures 5-34 and 5-35.

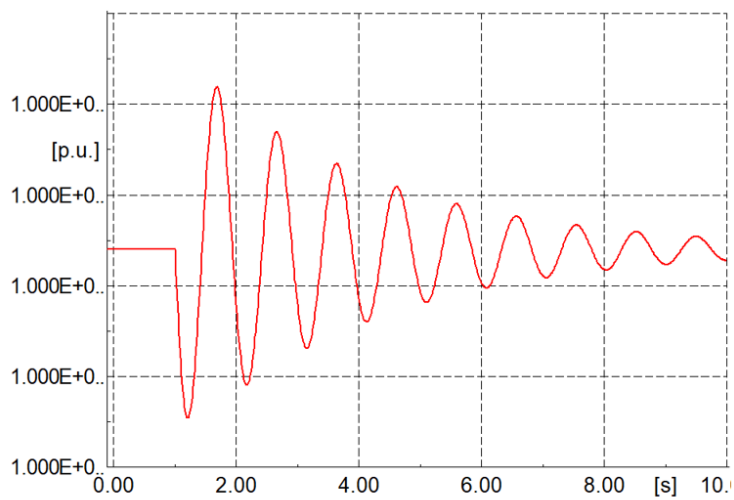


(a)



(b)

Figure 5-29 Time domain analysis at Gain = 0
(a) Rotor Speed (b) Active Power



(a)

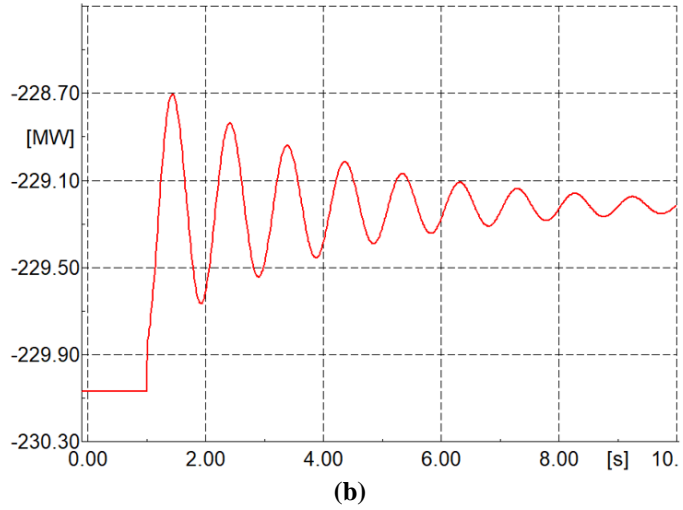


Figure 5-30 Time domain analysis at Gain = 10
 (a) Rotor Speed (b) Active Power

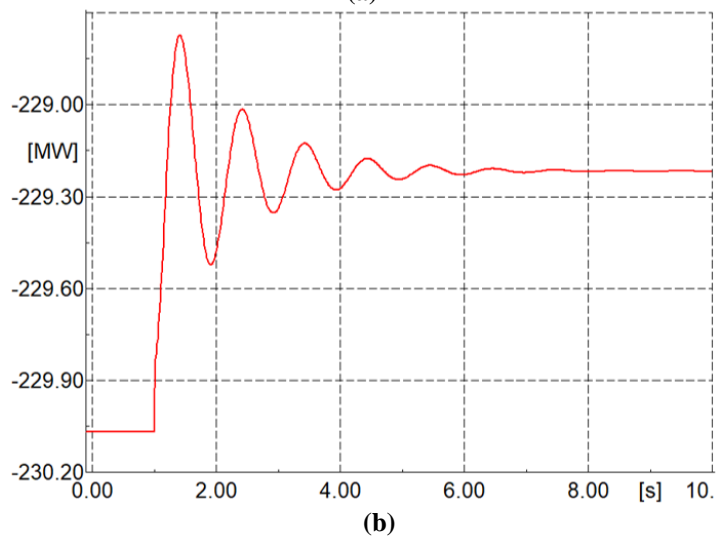
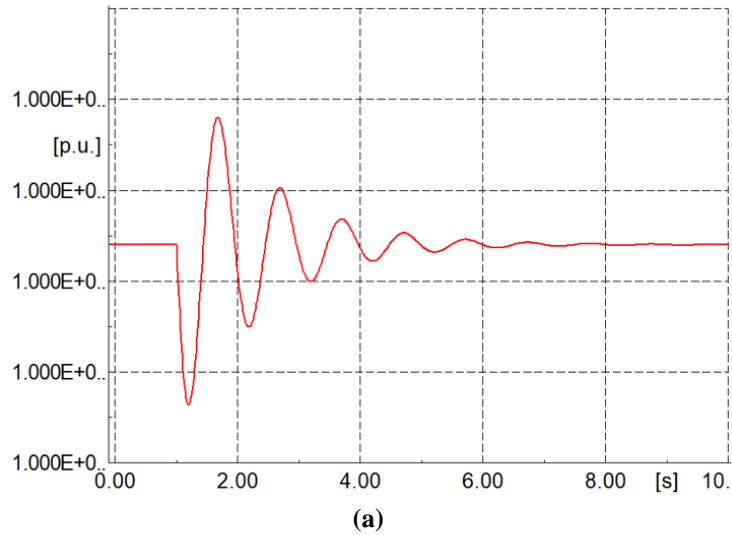
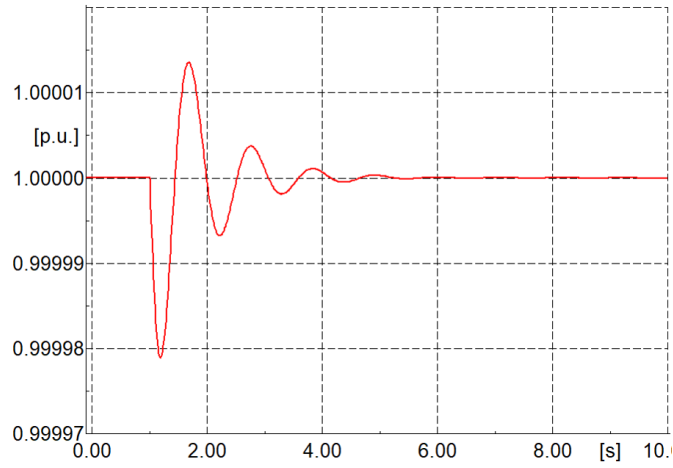
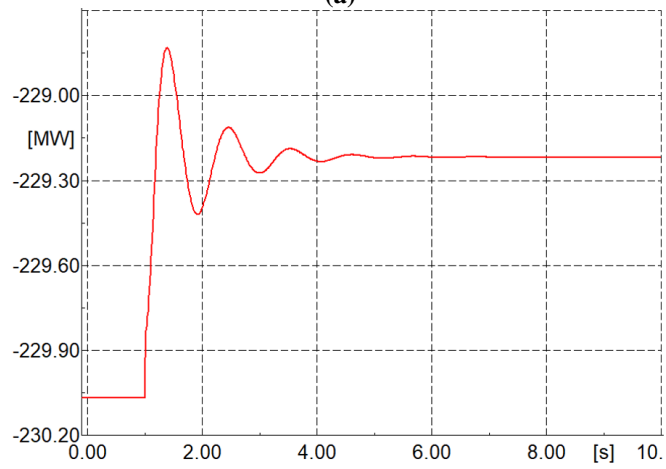


Figure 5-31 Time domain analysis at Gain = 20
 (a) Rotor Speed (b) Active Power

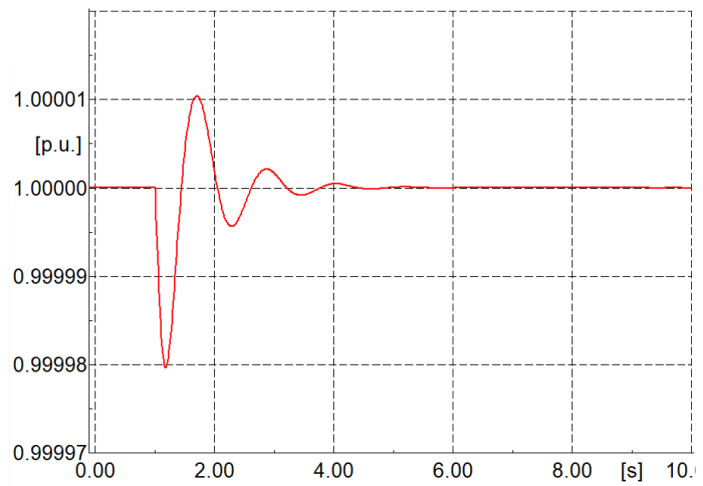


(a)

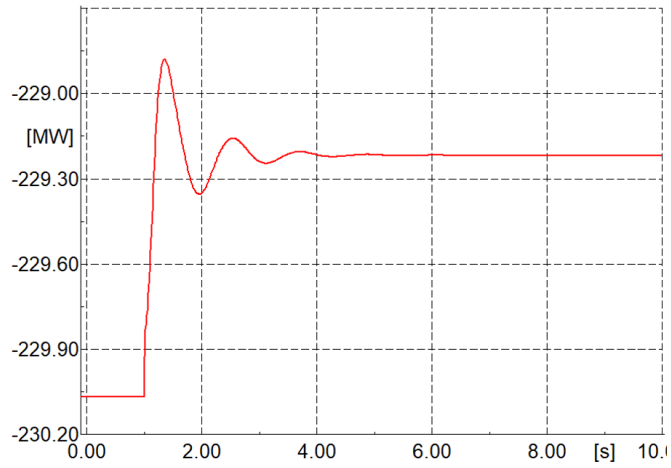


(b)

Figure 5-32 Time domain analysis at Gain = 30
(a) Rotor Speed (b) Active Power



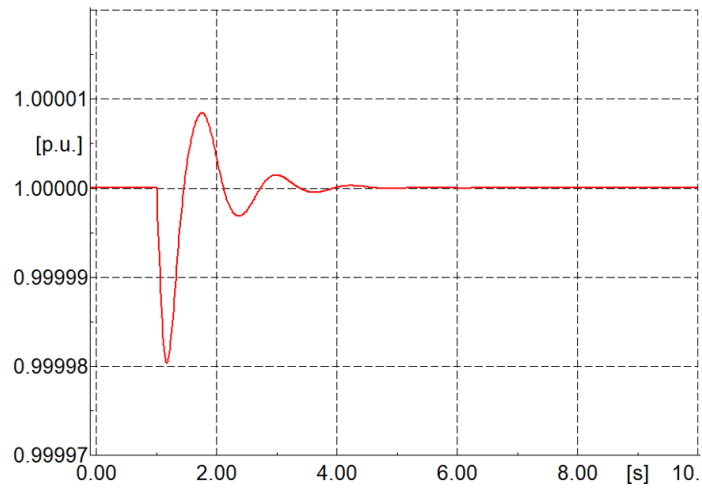
(a)



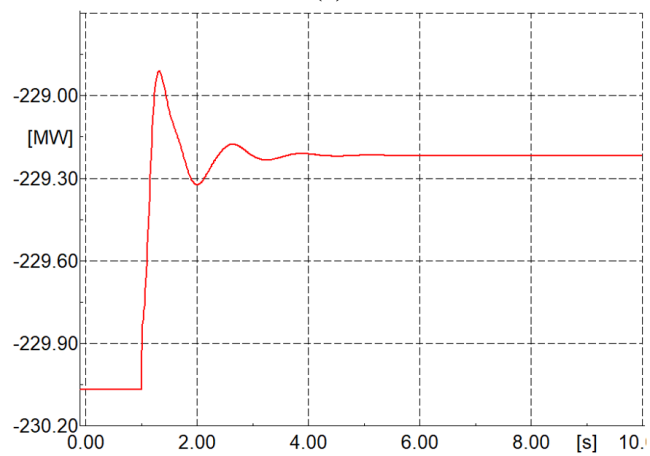
(b)

Figure 5-33 Time domain analysis at Gain=40

(a) Rotor Speed (b) Active Power



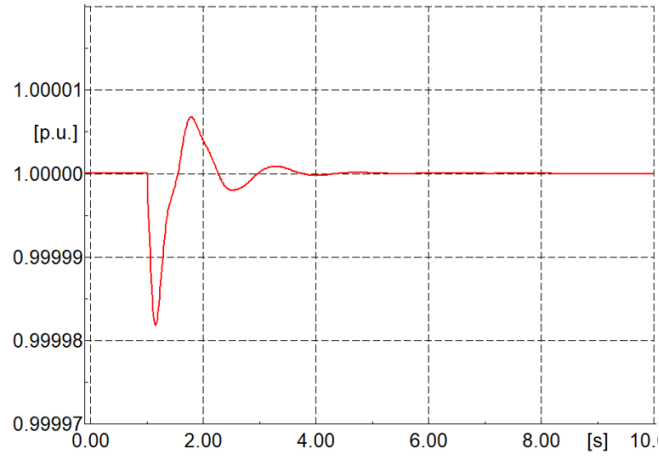
(a)



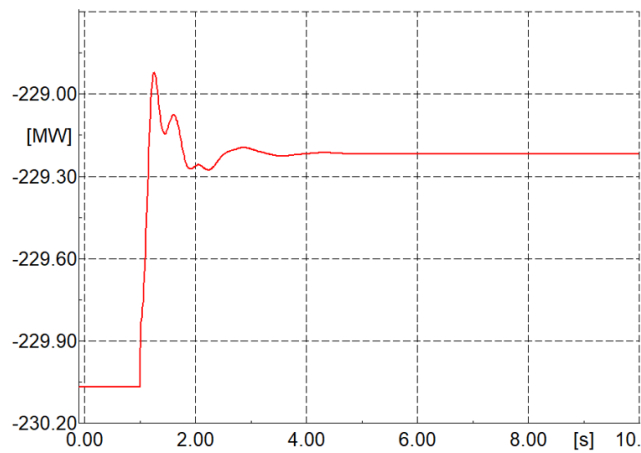
(b)

Figure 5-34 Time domain analysis at Gain = 50

(a) Rotor Speed (b) Active Power



(a)



(b)

Figure 5-35 Time domain analysis at Gain = 80
(a) Rotor Speed (b) Active Power

5.15 PSS DESIGN FOR BIPOLE CONFIGURATION

A power system stabilizer, coupled with an automatic voltage regulator (AVR) was designed to improve the damping of the two most poorly damped modes in the system: mode pairs 45 & 46 at $-0.472 \pm j10.944$ and more pairs 47 & 48 at $-0.407 \pm j7.109$, which have frequencies of 1.74 Hz and 1.13 Hz respectively. These mode pairs have damping ratios of 0.0431 and 0.0572 respectively. As done with the monopole, the PSS for the bipole configuration was designed using the mode with the lowest damping so that

$$\theta_{\text{PSS}} = 180 - 87.53 = 92.47^\circ$$

$$N = \frac{92.47^\circ}{60^\circ} = 1.54 \approx 2$$

The filter ratio and time constants T_1 to T_4 were determined from

$$\alpha = \frac{1 - \sin \frac{92.47^\circ}{2}}{1 + \sin \frac{92.47^\circ}{2}} = \frac{0.276}{1.724} = 0.161$$

$$T = \frac{1}{2\pi(1.13)\sqrt{0.161}} = 0.351 \text{ s}$$

$$T = T_1 = T_3 = 0.351 \text{ s}$$

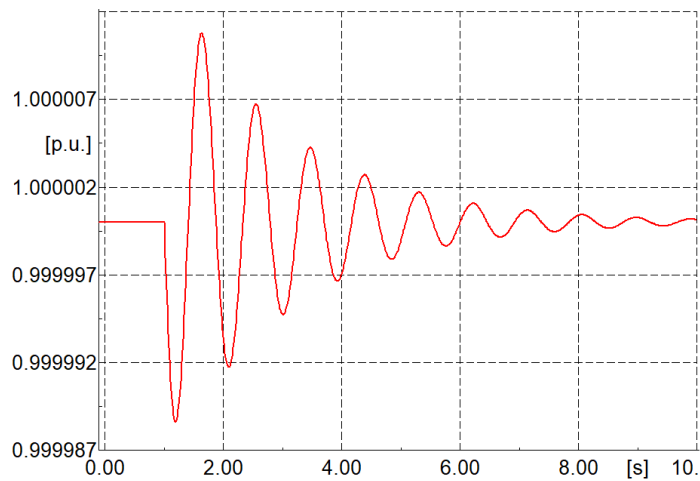
$$T_2 = T_4 = \alpha T = 0.161 \times 0.351 = 0.0565 \text{ s}$$

PSS Gain Optimization

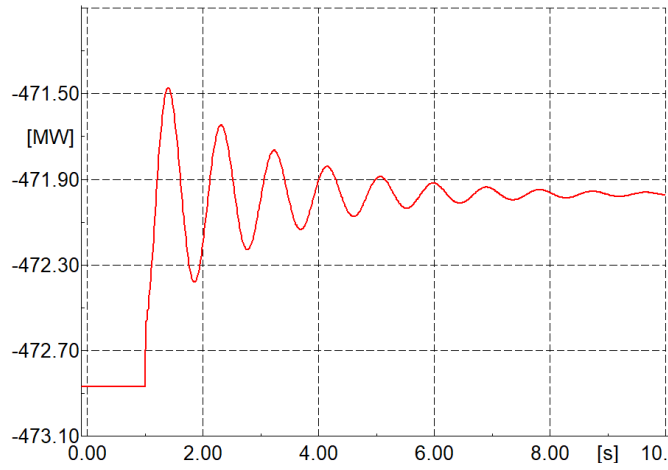
As with the monopolar configuration, the system shows instability at PSS Gain = 0. Increasing the gain value improves the damping of the system up until Gain = 30. Figures 5-36 to 5-38 show how the increase in gain damped out the oscillations. Distortions begin to appear at Gain = 40. Increase from 40 continues to distort the speed and active power waveforms, indicating that there is some noise in the system at these higher values. Table 5-10 shows the damping ratios of the two lowest mode pairs with and without a PSS.

Table 5-10 Eigenvector with and without PSS

Without PSS + AVR		With PSS + AVR	
Eigenvector	Damping	Eigenvector	Damping
$-0.473 \pm j10.94$	0.043	$-2.374 \pm j12.11$	0.192
$-0.407 \pm j7.11$	0.057	$-1.666 \pm j4.958$	0.319

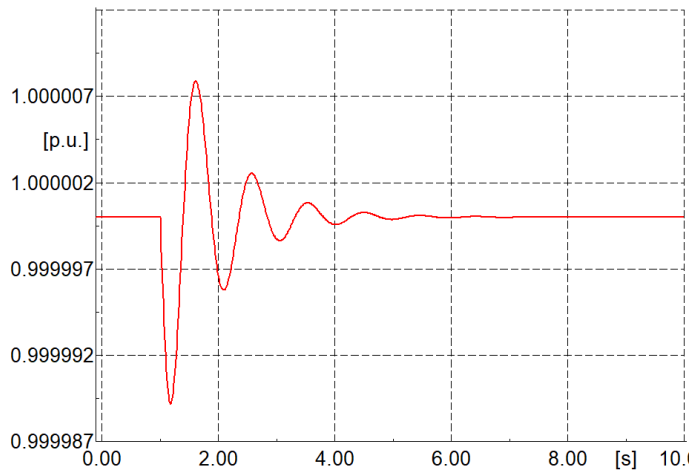


(a)

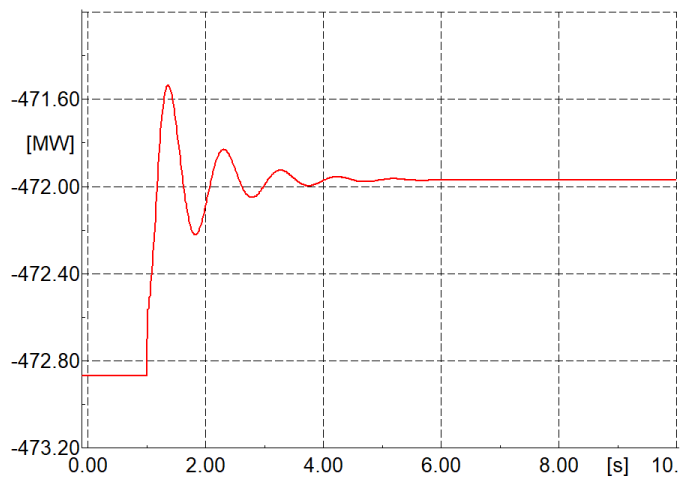


(b)

Figure 5-36 Power System Stabilizer at Gain = 10
(a) Rotor Speed (b) Active Power

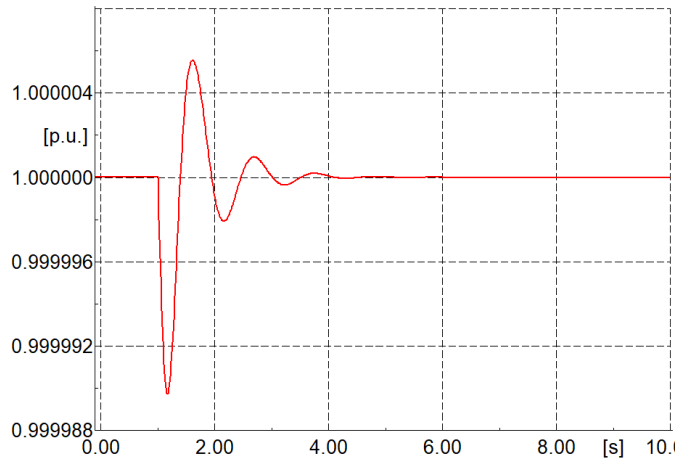


(a)

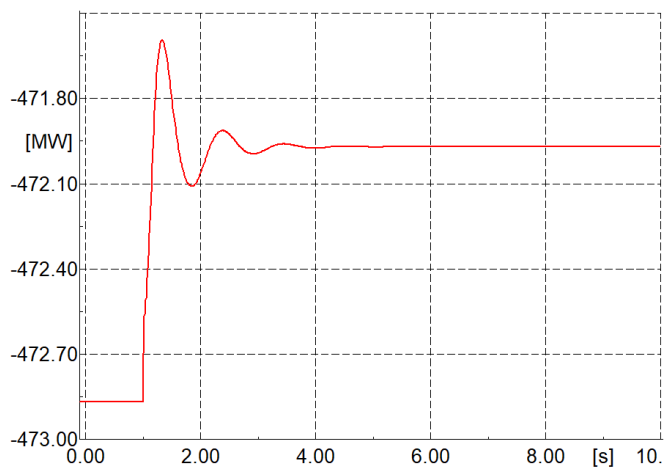


(b)

Figure 5-37 Power System Stabilizer at Gain = 20
(a) Rotor Speed (b) Active Power

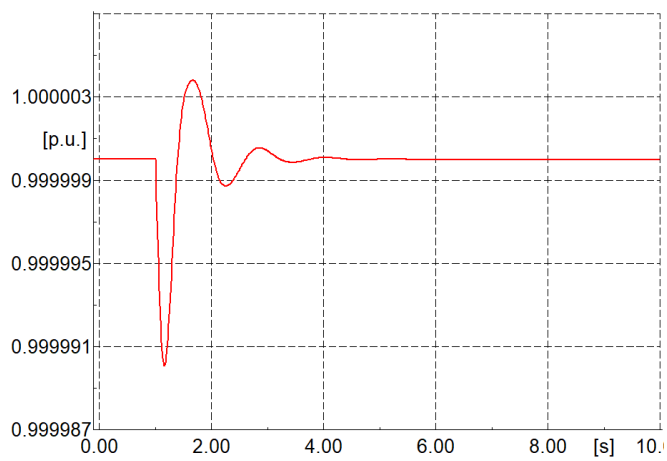


(a)



(b)

**Figure 5-38 Power System Stabilizer at Gain setting 30
(a) Rotor Speed (b) Active Power**



(a)

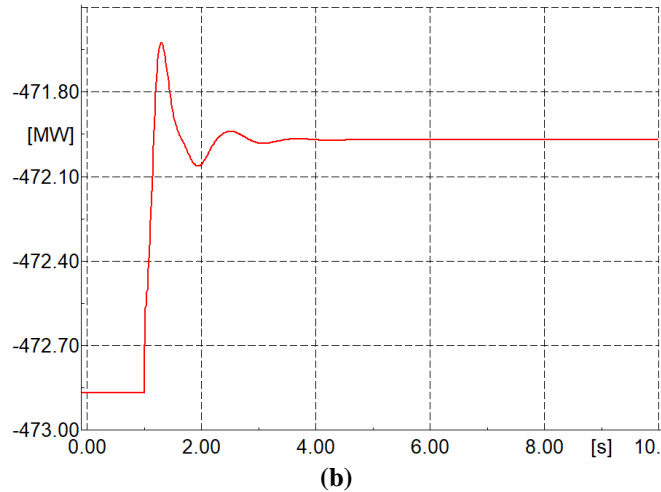


**Figure 5-39 Power System Stabilizer at Gain setting 40
(a) Rotor Speed (b) Active Power**

5.16 DESIGN OF TCSC FOR MONOPOLE AND BIPOLE CONFIGURATIONS

The PSS may not produce satisfactory damping at some operating conditions and disturbances, hence other effective alternatives are required in addition to the PSS. In recent years, through developments in power electronics, flexible AC transmission systems (FACTS) controllers have been widely used in power system [97]. In this study, the FACTS controller used is the TCSC, as illustrated in Figure 5-40.

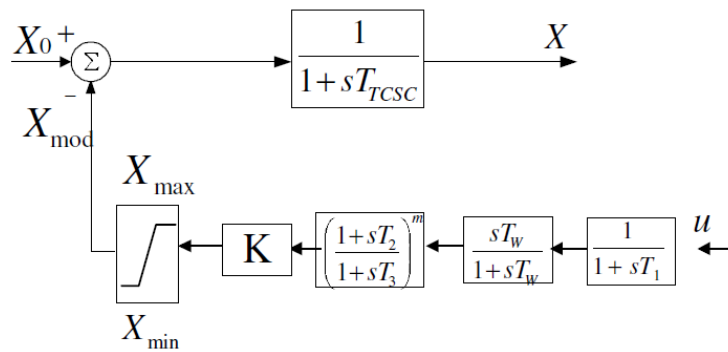


Figure 5-40 TCSC Block Diagram [98]

X_0 is the impedance reference point obtained from the higher-level controller is considered constant and is given by

$$X_0 = \frac{X_c X}{-X_c + X} \quad (5.9)$$

X is the output impedance of the TCSC, and X_{mod} is the modulated signal from the damping controller. The transfer function of the TCSC is

$$KH(s) = K \frac{1}{1+sT_1} \left[\frac{1+sT_2}{1+sT_3} \right]^N \left[\frac{sT_w}{1+sT_w} \right] \quad (5.10)$$

The block $\frac{1}{1+sT_1}$ is the controller measurement block whereas $\frac{1}{1+sT_{TCSC}}$ is the finite delay resulting from the firing controls and natural response of the TCSC. T_{TCSC} , the firing time constant, is usually in the range of 15 to 50 ms [98]. T_1 is the insertion time of the transient function. The lead-lag compensation block parameters are calculated using the same procedure as that of the PSS [99].

The TCSC gain optimization is also carried out in a similar manner to the PSS gain where the movement of the oscillatory modes are tracked as the gain is increased from zero [100].

The TCSC is placed in series with the AC transmission, before the rectifier, in the monopole system in Figure 5-1, and in the upper rectifier for the bipole in Figure A-5. The parameter values selected for this study are shown in Table 5-11. The phase compensation time constants are the same as those used in the PSS design.

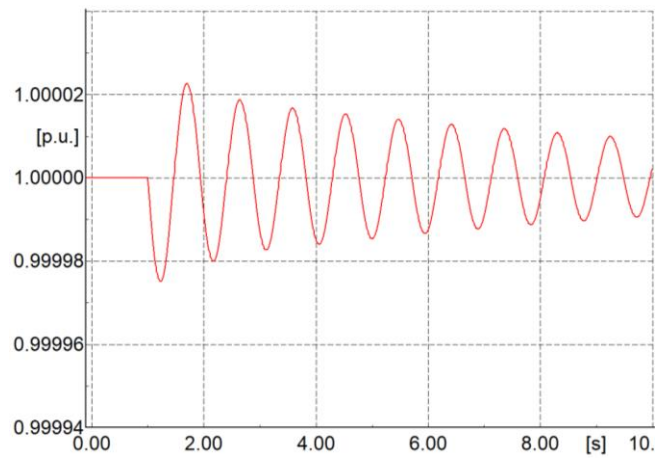
Table 5-11 TCSC design parameters

Parameter	Value
T_{TCSC}	0.05 s
T_w	5 s
T_1	5 s
X_{min}	15 pu
X_{max}	30 pu
X_C	10 Ω
K	0.002

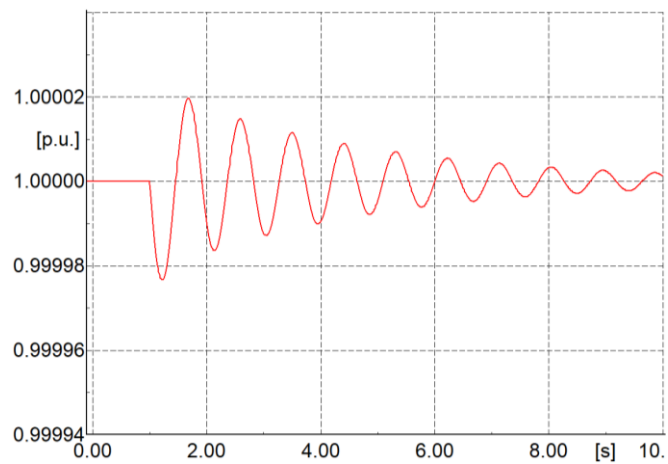
Gain Optimization

For simulation, the gain values are increased, starting from 0 in steps of 0.005 as shown in Figures 5-41 (a) to (h). Their effect on the generator rotor speed is then tracked in order to tune it to the optimum value. It can be seen in Figures 5-41 (a) to (h) that the optimal gain for the TCSC in the monopolar configuration is 0.002. When the gain is further increased to 0.003, distortions in the

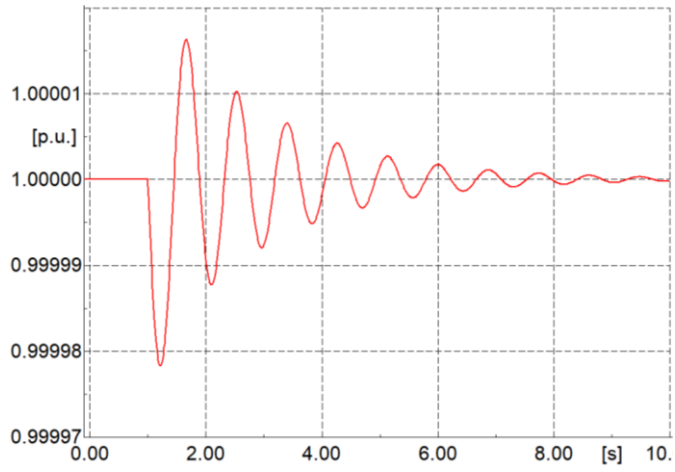
generator speed oscillations begin to appear. Increasing the gain even further to 0.0035 results in an unstable system. Tuning of the TCSC in the bipole gives the same result.



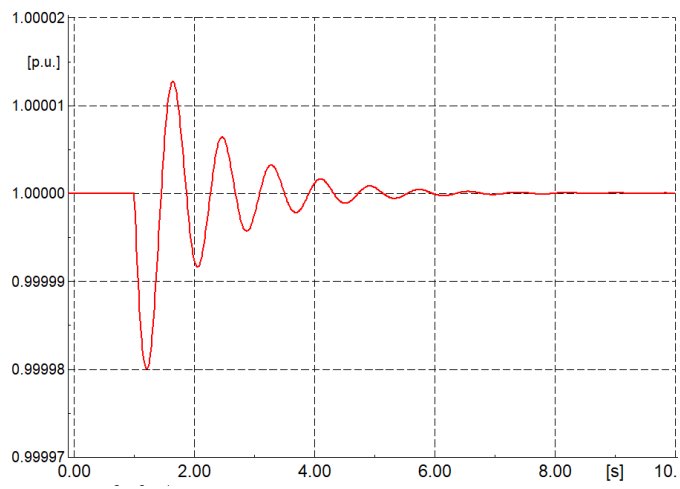
(a) Gain = 0



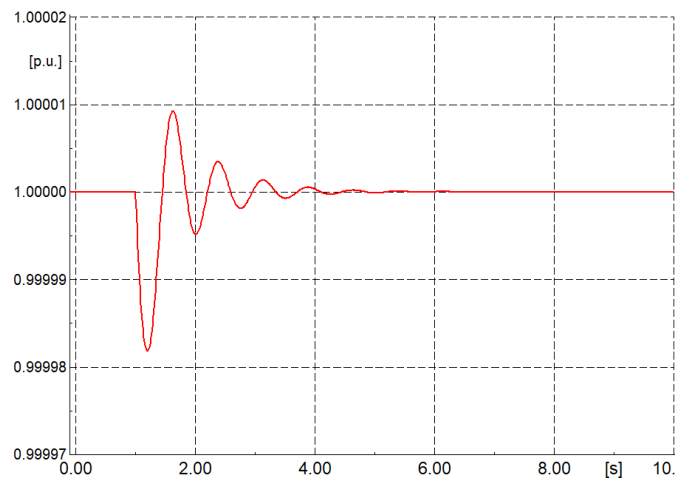
(b) Gain = 0.0005



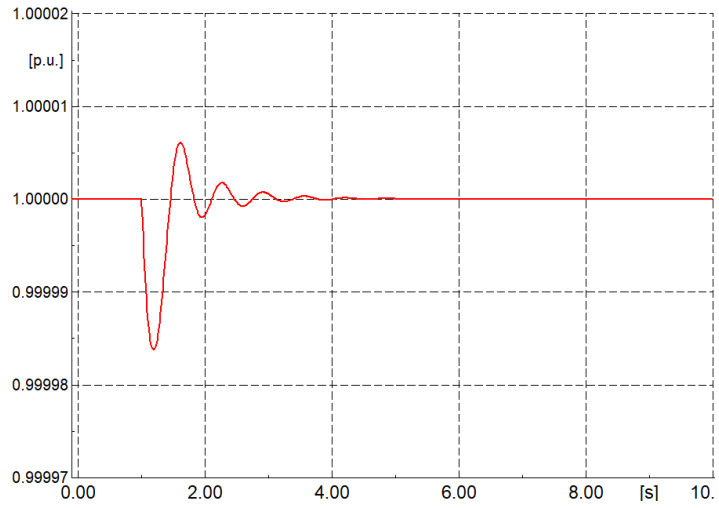
(c) Gain = 0.001



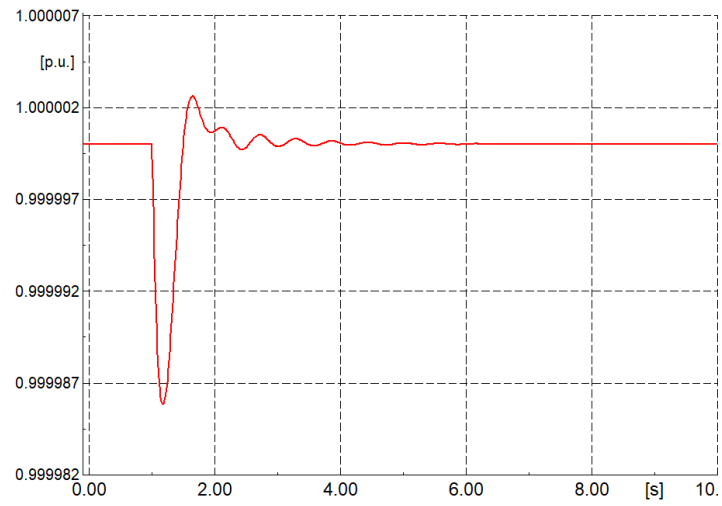
(d) Gain = 0.0015



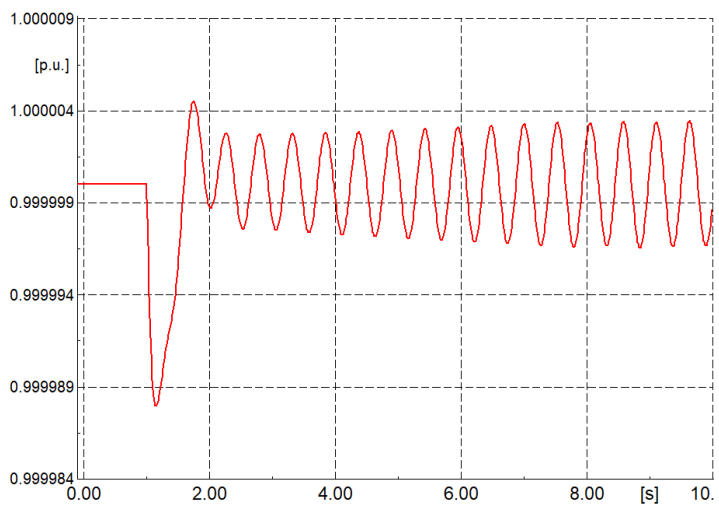
(e) Gain = 0.002



(f) Gain = 0.0025



(g) Gain = 0.003



(h) Gain = 0.0035

Figure 5-41 TCSC Gain Optimization

5.17 PSS AND TCSC TIME DOMAIN ANALYSIS

The PSS and TCSC perform in a similar manner for the monopole and bipole systems. The time domain analysis shown in Figures 5-42 and 5-43 show that the damping is significantly improved using power oscillation damping controllers. The AVR on its own causes the system to become unstable, but once paired with the PSS, the oscillations are damped faster than when there is no damping controller. In the monopole, the PSS performs better than the TCSC as the speed returns to its pre disturbance value at about 2.9 s whereas with the TCSCs, this value is around 4.1 s. For the bipole configuration, there is only a slight difference in the performance of the two damping controllers as the settling time of the TCSC improves to 3.3 s in this configuration. Figure 5-42 shows that the generator speed returns to its initial value at 3.2 s with the PSS and at 3.5 s with the TCSC.

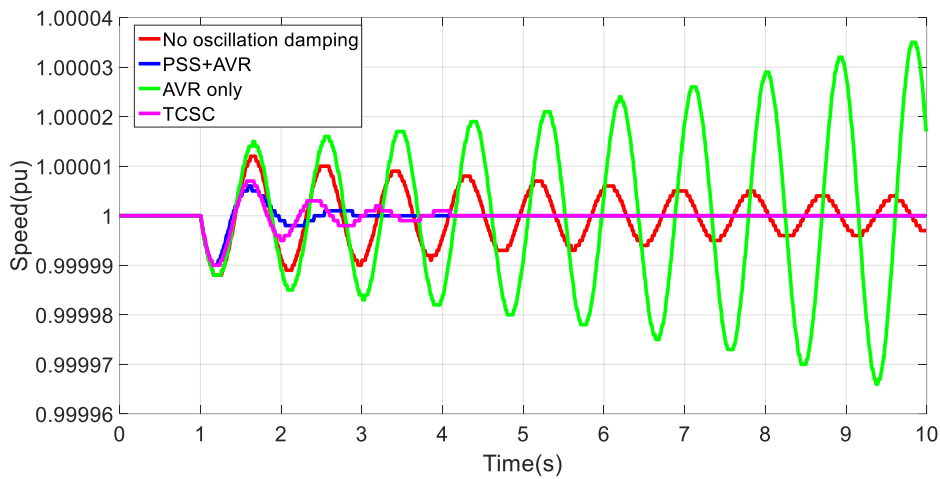


Figure 5-42 Monopole oscillation damping

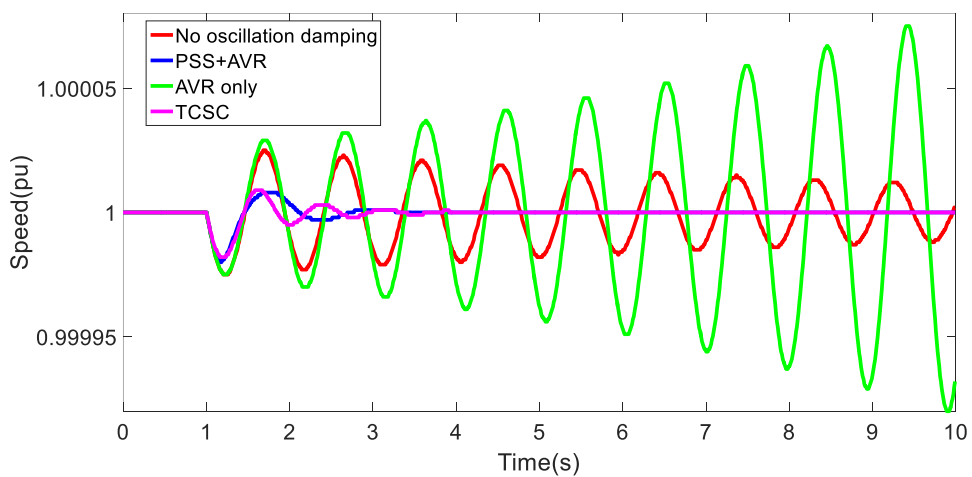


Figure 5-43 Bipole oscillation damping

5.18 CONCLUSIONS

The following deductions can be made with regards to the effect of the investigated conditions on the wind energy incorporated monopole and bipole networks.

Monopole with Wind Generation

Introducing wind generation adds extra modes into the system. These modes are sub synchronous oscillatory as well as local electromagnetic modes. The added modes are well damped and therefore the system remains stable. The electromechanical mode that is poorly damped in the base system becomes worse with the introduction of wind power. This is illustrated by the time domain analysis which shows an increase in amplitude of the oscillations compared the monopole network without wind generation.

The majority of the oscillatory modes of the system are generally unaffected by changes in SCR and controller gain. Only two mode pairs are affected by these changing conditions. The condition that has the most adverse effect on these two mode pairs is the varying of the inner and outer controller gains. This can be seen by the more dispersed eigenvector trajectories, indicating rapid movement of the modes as the gains are changed. This shows that controller gain has a significant effect on small signal stability of a monopole VSC-HVDC system.

Change in wind output power, however, has an effect on all the modes except for one mode pair - 20 & 21, which remains unaffected by any change incurred by the system. This is unlike the other conditions that only have an effect on two oscillatory mode pairs. Modes 20 & 21, being the only exceptions, remain unaffected because the source of this mode is the overhead DC line, therefore any change in the system conditions will not affect this mode. Most modes are highly sensitive to varying wind generation. This is an indication that the intermittence of wind power would have an effect on the small signal stability of the system and therefore must be paid close attention to.

Bipole with Wind Generation

It is important to establish the sensitivity of the oscillatory modes in order to identify what parameters to monitor when expanding a system from a monopole to a bipole. Knowing the behaviour of different modes in the system, under different conditions, is also a deciding factor when deciding the necessary mitigation techniques for damping of the critical modes.

The modes in the bipole system show that there are similar modes at the same point on corresponding half of the bipole network. As with the monopole, the different conditions of the VSC-HVDC System have different effects on the small signal stability of the bipolar system.

A change in SCR and change in the controller gains do not have an effect on most modes in the system, except four oscillatory modes. This is the same as the monopole system. These four modes respond to the change in conditions in a similar manner to those in the monopole.

Both the monopole and bipole systems, as observed in the time domain analysis, show that the oscillations are not damped out by the end of the 10 s simulation time. The generators in both systems are likely to suffer fatigue in the long run if the oscillations caused by modes are not damped out. Consequently, it is important to include some power oscillation damping measures in order to increase the lifespan of the system as well as improve stability.

In conclusion, the oscillatory modes are most sensitive to the controller parameters and therefore during the design or expansion of a VSC-HVDC network, it is important to ensure that controllers are set to values that provide the best stability to the system.

Damping Controllers

For the monopole system, it can be concluded that a PSS gain selection of 40 is the best for damping out the system electromechanical oscillations. The PSS, coupled with an AVR is included in the main generator and the damping of the oscillatory mode is greatly improved to a damping ratio of 26.9 % at $-1.409 \pm j5.039$. By $t = 4.0$ s the oscillations are damped out completely and the system is back to being stable, compared to the previous case where the oscillations were not damped out by $t = 10.0$ s. The electromechanical mode pair 46 & 47, which initially have a damping ratio of 4.8 %, now has a damping ratio of 26.9 % with the inclusion of the PSS.

The PSS is also designed for the bipole system and the best gain is 30. The damping ratios of the two lowest modes are improved to 19.2 % and 31.9 % respectively, which is well above the acceptable minimum of 5 %. A time domain analysis confirms this damping as well as the movement of the eigenvectors more towards the left of the S plane, proving that the system becomes more stable with the inclusion of the PSS.

The TCSC design for the monopole is exactly the same as for the bipole. Both systems result in a best gain of 0.002. The settling time for the oscillations is much lower in the bipole system, therefore the TCSC functions better in this configuration. The damping ratio of the electromechanical mode pair 46&47 improved from 4.8 % at $-0.318 \pm j6.643$ to 24.6% at $-2.029 \pm j8.00$, only slightly less than the effect that the PSS had on the damping of this mode pair.

In conclusion with regards to the comparison of the two damping controllers, the PSS offers better damping than the TCSC which is clearly evident in the monopole configuration. The performance of the two damping controllers are comparable in the bipole configuration since the settling time of the oscillations only differs by a small margin.

6 CONCLUSIONS AND RECOMMENDATIONS

6.1 CONCLUSIONS

In order to address the research questions in raised in Chapter 1, the following points can be concluded from the simulation and results of this research.

- Three networks were designed, built and simulated in DIgSILENT PowerFactory software. The first being the Base Case network which was a monopole HVDC system, the second was a monopole with wind generation and the third was a bipole system with wind generation.
- All three networks were found to be stable as all the oscillatory modes lay on the left hand side of the S plane.
- Although stable, the oscillations displayed a high settling time and these could result in machine fatigue, hence they may be detrimental to the generator life cycle.
- The modes that were observed in the base network were super synchronous control oscillations caused by the interaction of the controllers, and also electromechanical modes, specifically local modes, resulting from the main generator oscillating against the rest of the network.
- A wind farm was successfully added to the monopole system as an auxiliary source and the monopole system was expanded to a bipole network.
- The addition of the wind farm added extra modes to the network, which were sub synchronous modes as well as electromagnetic modes, specifically local modes.
- Expanding the monopole to a bipole added even more oscillatory modes. The bipole had similar modes in corresponding parts of the other half of the bipole.
- The mode with highest damped frequency in the monopole system was at the super synchronous frequency of 405.6 Hz and a similar mode was found in the bipole system at half its monopole frequency of 203 Hz.
- These networks were subjected to different conditions of short circuit ratio (SCR), varying inner and outer controller gains, and varying wind generation levels.
- The movement of the oscillatory modes under these conditions were observed, establishing their effect on small signal stability. A change in the inner and outer controller gains was established to have the most effect on the affected modes.
- Two mode pairs were affected by the change in SCR and the change in the inner and outer controller gains in the monopole systems, and four in the bipole system.
- Most oscillatory modes in the monopole and bipole networks were significantly sensitive to the varying wind power generation levels. This is established from the observation that

even those modes that were unaffected by change in SCR and controller gains, were affected by change in wind generation levels.

- A PSS and TCSC were designed using the residue method to improve the damping of the electromechanical oscillatory modes and hence the small signal stability of the monopole and bipole systems.
- The best gain of the monopole PSS was 40 and the bipole was 30, whereas the gain for the TCSC was the same for both the monopole and the bipole at 0.002. Further increase of any of these optimal gain settings saw the introduction of noise into the system.
- The damping controllers were both successful at improving the stability of the monopole and bipole systems, the PSS being the better of the two as it provided a shorter settling time. This was more significant in the monopole since the settling time resulting from the two differed by 1.2 s, whereas in the bipole, this difference was reduced to a margin of 0.4 s.

To address the research questions posed in Chapter 1, the findings of this research may help planners and engineers to better predict the behaviour of a VSC based HVDC network with wind energy in terms of its small signal stability. It can be concluded that wind energy does indeed add extra oscillatory modes to a VSC based HVDC system, reducing the overall stability of the system. The outcomes of this research could help control engineers when tuning VSC controllers for use in similar systems. This research contributes to the knowledge base that will help formulate grid codes for small signal stability requirements in HVDC systems.

6.2 RECOMMENDATIONS FOR FUTURE RESEARCH

For future research, it is recommended that transient stability studies should be done in order to further validate the small signal stability results obtained here. It is recommended to extend the research to the investigation of how the small signal stability of the multi-terminal configuration would be affected by the different conditions. This is because multi-terminal HVDC systems are beginning to be incorporated into power systems, and it is important to establish the interactions that occur in these types of systems. Another scenario that could be investigated in future research is the stability analysis of a hybrid system that incorporates both LCC and VSC converters, which aims to optimise the advantages offered by each converter technology.

Although DFIG wind turbines are a mature technology, more recent wind turbine types such as Permanent Magnet Synchronous Generators can be investigated and compared with the results obtained using DFIGs in this research. In terms of converter topology, modular multi-level converters can be investigated instead of the two level converters implemented in this study.

Other methods of small signal stability analysis can be used instead of the conventional eigenvalue analysis. Some of these methods include the probabilistic small signal stability

analysis, which account for the vulnerable nature of modern day power systems. Probabilistic small signal stability analyses employ numerical methods such as the Monte Carlo method or analytical methods such as the Gram-Charlier expansion method.

More advanced and modern solutions of improving small signal stability can be implemented and the converter control of the system could be improved further by using an active damping controller and further improvements can be done on the wind generator controls since the system stability was quite sensitive to changes in the with power.

REFERENCES

- [1] B. K. Blyden and I. E. Davidson, "Energizing Africa's Emerging Economy," *IEEE Power and Energy Magazine*, Vol.3, Iss. 4, pp 24-31, 2005.
- [2] J. W. B. J. Machowski and J. R. Bumby, *Power Systems Dynamics: Stability and Control*. West Sussex, United Kingdom: John Wiley & Sons, 2008.
- [3] E. Krige, "Harmonic Interaction between AC Systems and VSC-based HVDC schemes," Master of Science in Electrical Engineering, Electrical and Electronics Engineering, University of Stellenbosch, Stellenbosch, 2012.
- [4] J. Yu, "Influence of Embedded HVDC Transmission on AC Network Performance", Master of Science, Arizona State University, Arizona State University, 2013.
- [5] K. Mbangula, "An investigation into the impact of HVDC schemes on ESKOM HV network's transient stability", Master of Science in Electrical Engineering, Electrical and Electronics, University of Kwazulu-Natal, Durban, 2015.
- [6] G. Daelemans, K. Srivastava, M. Reza, S. Cole, and R. Belmans, "Minimization of steady-state losses in meshed networks using VSC-HVDC," *IEEE Power & Energy Society General Meeting*, 2009, pp. 1-5.
- [7] D. N. Huu, "Small signal assessment of an AC system integrated with a VSC-HVDC network," *IEEE International Conference on Computer as a Tool (EUROCON)*, 2015, pp. 1-6.
- [8] D. GmbH. *DIGSILENT PowerFactory*. Available at: <http://www.digsilent.de/index.php/products-powerfactory.html>, 14 September, 2016.
- [9] C. Sulzberger, "Thomas Edison's 1882 Pearl Street Generating Station," *IEEE Global History Network*, 2010.
- [10] I. Cvetkovic, "Modelling, Analysis and Design of Renewable Energy Nanogrid Systems", Master of Science in Electrical Engineering, Virginia Polytechnic Institute and State University, Blacksburg, Virginia, 2010.
- [11] L. d. Andrade and T. P. d. Leao, "A Brief History of Direct Current in Electrical Power Systems," *History of Electro-technology Conference*, Lisbon, Portugal, 2012.
- [12] P. Kundur, *Power Systems Stability and Control*. United States of America: McGraw-Hill, 1994.
- [13] K. Meah and S. Ula, "Comparative Evaluation of HVDC and HVAC Transmission Systems," *Power Engineering Society General Meeting*, 24-28 June 2007.
- [14] J. Pan, R. Nuqui, K. Srivastava, T. Jonsson, P. Holmberg, and Y.-J. Hafner, "AC Grid with Embedded VSC-HVDC for Secure and Efficient Power Delivery," *IEEE Energy 2030 Conference*, Atlanta, USA, 2008.

- [15] T. Halder, "Comparative study of HVDC and HVAC for a bulk power transmission," *International conference on Power, Energy and Control*, pp 139-144, 2013.
- [16] L. Zhang, L. Harnefos, and H. P. Nee, "Interconnection of Two Very Weak AC Systems by VSC-HVDC Links Using Power-Synchronization Control," *IEEE Transactions on Power Systems*, vol. 26, pp. 344-355, 2011.
- [17] C. C. Bonilla and S. M. Tigga, "Design and Performance comparison of two level and multilevel converters for HVDC Applications", Master's in Electric Power Engineering, Department of Energy and Environment, Chalmers University of Technology, Goteborg, Sweden, 2011.
- [18] Z. Chen, J. M. Guerrero, and F. Blaabjerg, "A Review of the state of the art of power electronics for wind turbines," *IEEE Transactions on Power Electronics*, vol. 24, pp. 1859-1875, 2009.
- [19] O. E. Oluwafemi, I. E. Davidson, and K. N. I. Mbangula, "A Review of LCC-HVDC and VSC-HVDC Technologies and Applications," *IEEE 16th International Conference on Environment and Electrical Engineering (EEEIC)*, 2016.
- [20] B. K. Bose, "Evaluation of Modern Power Semiconductor devices and future trends of converters," *IEEE Transactions on Industry Applications*, vol. 28, pp. 403-413, 1992.
- [21] J. M. Carrasco, J. T. Bialasiewicz, R. C. P. Guisado, and J. I. Leon, "Power Electronics Systems for the grid intergration of renewable energy sources: A survey," *IEEE Transactions on Industrial Electronics*, vol. 53, pp. 1002-1016, 2006.
- [22] N. Chaudhuri, B. Chaudhuri, R. Majumder, and A. Yazdani, *Multi-terminal direct current grids: Modelling, analysis and control*, Wiley IEEE-Press, 2014.
- [23] F. Shewarega and I. Erlich, "Simplified Modeling of VSC-HVDC in Power System Stability Studies " *Proc of The Interational Federation of Automatic Control (IFAC)*, Cape Town, South Africa, Vol 47, Iss 3, 2014, pp 9099-9104.
- [24] X. I. Koutiva, T. D. Vrionis, N. A. Vovos, and G. B. Giannakopoulos, "Optimal Integration of an offshore wind farm to a weak AC gridI," *IEEE Transactions on Power Delivery*, vol. 21, pp. 987-994, 2006.
- [25] L. A. Soriano, W. Yu, and J.JRubio, "Modeling and control of wind turbine," *Mathematical Problems in Engineering*, vol. 2013, 2013, Article ID 982597.
- [26] O. E. Oni, I. E. Davidson, and K. N. I. Mbangula, "A review of LCC-HVDC and VSC-HVDC technologies and applications," *IEEE 16th International Conference on Environment and Electrical Engineering (EEEIC)*, 2016, pp. 1-7.
- [27] CIGRE, "Influence of embedded HVDC Transmission on System Security and AC Network Performance," 2013.

- [28] K. N. Hasan and T. K. Saha, "Reliability and Economic study of Multi-terminal HVDC with LCC & VSC Converter for Connecting Remote Renewable Generators to the Grid," *Power and Energy Society General Meeting (PES)*, 2013.
- [29] P. C. S. Krishnayya, S. Lefebvre, V.K.Sood, and N.J.Balu, "Simulator Study of Multiterminal HVDC With Small Parallel Tap and Weak AC Systems," *IEEE Transactions on Power Apparatus and Systems*, vol. PAS-103, pp. 3125-3132, 1984.
- [30] G. P. Adam, S. J. Finney, B. W. Williams, K. Bell, and G. M. Burt, "Control of Multi-Terminal DC Transmission System Based on Voltage Source Converters," *IET International Conference on AC and DC power transmission*, 2010.
- [31] D. Pudney, H. P. Systems, L. Wei, "VSC-HVDC best suited for power transmission in Africa," *Energize*. Nov. 2013, pp 32-33
- [32] S. Cole and R. Belmans, "Transmission of Bulk Power: The history of voltage source converter high voltage direct current systems," *IEEE Industrial Electronics Magazine*, Vol. 3, Iss. 3, 2009, pp 19-24.
- [33] L. G. Peng Wang, Xiong Liu, Fook Hoong Choo, "Harmonizing AC and DC: A Hybrid AC/DC Future Grid Solution," *IEEE Power and Energy Magazine*, Vol 11, Iss. 3, 2013, pp. 76-83.
- [34] K. Meah and S. Ula, "A new simplified adaptive control scheme for multiterminal HVDC transmission systems," *International Journal of Electrical Power & Energy Systems*, vol. 32, pp. 243-253, 2010.
- [35] V. C. Billon, J. P. Taisne, V. Arcidiacono, and F. Mazzoldi, "The corsican tapping: From design to commissioning tests of the third terminal of Sardinia-Corsica-Italy HVDC Link," *IEEE Transactions on Power Delivery*, vol. 4, pp. 794-799, 1989.
- [36] M. Hausler, "Multiterminal HVDC for High Power Transmission in Europe," *CEPEX99*, Poland, 1999.
- [37] T. Magg, M. Manchen, E. Krige, J. Wasborg, and J. Sundin, "Connecting networks with VSC-HVDC in Africa: Caprivi Link interconnector," *IEEE Power Engineering Society Conference and Exposition in Africa (PowerAfrica)*, 2012, pp. 1-6.
- [38] T. Magg, M. Manchen, E.Krige, J. Wasborg, and J. Sundin, "Connecting networks with VSC-HVDC in Africa: Caprivi Link Interconnector," *IEEE Power Engineering Society Conference and Exposition in Africa (PowerAfrica)*, 2012.
- [39] E. A. I. T. Fund, "Caprivi Link Interconnector (Namibia)," *Project Completion Report*, Luxembourg 2012.
- [40] T. G. Magg, M. Manchen, E. Krige, E. Kanjii, R. Palsson, and J. Wasborg, "Caprivi Link HVDC Interconnector: Comparison between energized system testing and real-time simulator testing " *CIGRE*, Paper B4 107 2012, 2012.

- [41] R. N. J. Pan, L. Tang, and P. Holmerg, "VSC-HVDC Control and Application in Meshed AC Networks," *IEEE Power and Energy Society Annual Meeting (PES)*, Pittsburgh, Pennsylvania, 2008.
- [42] V. G. Agelidis, G. D. Demetriades, and N. Floure, "Recent advances in High Voltage Direct Current Power Transmission Systems," *IEEE International conference on Industrial Technology*, 2007, pp 206-213.
- [43] X. Koutiva, T. Vrionis, N. A. Vovos, and G. Giannakopoulos, "A simulation model of an HVDC Link using VSCs and a control system exploiting its capabilities," *Workshop on Computer Science and Information Technology*, Patras, Greece, 2002.
- [44] W. Taha, A. R. Beig, and I.Boiko, "Design of PI Controllers for a grid connected VSC based on optimal Disturbance Rejection," *IEEE Industrial Electronics Society Annual Meeting (IECON)*, 2015, pp 1954-1959.
- [45] L.Zhang, L.Harnefos, and H. P. Nee, "Modeling and control of VSC-HVDC Links connected to island systems," *IEEE Transactions on Power Systems*, vol. 26, pp. 783-793, 2011.
- [46] G. P. Adam and I. E. Davidson, "Robust and Generic Control of Full Bridge Modular Converter High Voltage DC Transmission Systems," *IEEE Transactions on Power Delivery*, vol. 30, pp. 2468-2476, 2015.
- [47] G. P. Adam, S. J. Finney, B. Williams, I. E. Davidson, and A. Y. M. Abbas, "Full Bridge Modular Multilevel Converter (FB-MMC) with Extended Control Range," *IEEE Region 8 International Conference*, pp. 833-837, September 14-16 2015.
- [48] M. M. C. Bajracharya, J. A. Sull, and T. Undeland, "Understanding tuning techniques of converter controllers for VSC-HVDC," *Nordic Workshop on Power and Industrial Electronics*, 2008.
- [49] K. R. Seenaa and T. K. Sindhu, "Power synchronization control of VSC-HVDC transmission for weak AC Systems," *International Journal of Power System Operation and Energy Management*, vol. 2, pp. 2231-4407.
- [50] P. B. Rodrigo, T. Pinto, S. F. Rodrigues, E. J. Wiggelinkhuizen, J. Pierik, and B. Ferreira, "A Novel Distributed Direct-Voltage Control Strategy for Grid Intergration of offshore Wind Energy Systems Through MTDC Network," *IEEE Transactions on Industrial Electronics*, vol. 60, 2013.
- [51] C. Bajracharya, "Control of VSC-HVDC for wind power", Master of Science in Energy and Environment, Department of Electric Power Engineering, Norwegian University of Science and Technology, 2008.
- [52] T. Kalitjuka, "Control of Voltage Source Converters for Power System Applications", Master of Science in Electric Power Engineering, Department of Electric Power Engineering, Norwegian University of Science and Technology, 2011.

- [53] R. Kavitha and N. Priya, "A control topology to enhance performance of weak grid under different power levels," *International Journal of Science and Research*, vol. 3, 2014.
- [54] T. H. S. Li and L. Xu, "Control of HVDC Using Conventional and Direct Current Vector Control Approaches," *IEEE Transactions on Power Electronics*, vol. 25, Iss 12, 2010, pp 3106-3118.
- [55] C. Du, "The Control of VSC-HVDC and its use for large industrial power systems", Licentiate of Engineering Thesis, Department of Electric Power Engineering, Chalmers University of Technology and Science, Sweden, 2003.
- [56] A. I. Stan and D. I. Stroe, "Control of VSC based HVDC transmission system for offshore wind power plants", Master of Science Thesis, Department of Energy Technology, Aalborg University, Denmark, 2010.
- [57] J. L. Dominguez-Garcia, O. Gomis-Bellmunt, F. Bianchi, and A. Sudria-Andreu, "Power control of voltage source converter for distributed generation," *PHYSCON*, 2011.
- [58] G. P. Adam, *Voltage source converter modulation, modelling, control and applications in power systems*, CreateSpace Independent Publishing Platform, 2013.
- [59] Energy.gov. *Wind Energy Technologies Office*. Available: <https://energy.gov/eere/wind/inside-wind-turbine-0>, 17 October 2017.
- [60] W. P. Program, *Wind turbine power output variation with steady wind speed*. Available: http://www.wind-power-program.com/turbine_characteristics.htm, October 23 2017.
- [61] REN21, "Renewables 2017 Global Status Report," Available: <http://www.ren21.net2017>, October 2017.
- [62] T. Ackermann, *Wind power in power systems*: John Wiley & Sons, 2005.
- [63] D. Van Hertem, O. Gomis-Bellmunt, and J. Liang, *HVDC grids: for offshore and supergrid of the future*, John Wiley & Sons-IEEE Press, 2016.
- [64] H. Li and Z. Chen, "Overview of different wind generator systems and their comparisons," *IET Renewable Power Generation*, vol. 2, pp. 123-138, 2008.
- [65] S. Tripathi, A. Tiwari, and D. Singh, "Grid-integrated permanent magnet synchronous generator based wind energy conversion systems: A technology review," *Renewable and Sustainable Energy Reviews*, vol. 51, pp. 1288-1305, 2015.
- [66] Y. Y. Frede Blaabjerg, Dongsheng Yang, Xiongfei Wang, "Wind Energy Systems," *Distributed Power-Generation Systems and Protection*, vol. 105, pp. 1311-1331, 2017.
- [67] F. Blaabjerg, M. Liserre, and K. Ma, "Power electronics converters for wind turbine systems," *IEEE Transactions on Industry Applications*, vol. 48, pp. 708-719, 2012.
- [68] O. Gomis-Bellmunt, A. Junyent-Ferre, A. Sumper, and J. Bergas-Jane, "Ride-through control of a doubly fed induction generator under unbalanced voltage sags," *IEEE Transactions on Energy Conversion*, vol. 23, pp. 1036-1045, 2008.

- [69] P. Kundur, J. Paserba, V. Ajjarapu, G. Andersson, A. Bose, C. Canizares, *et al.*, "Definition and classification of power system stability IEEE/CIGRE joint task force on stability terms and definitions," *IEEE Transactions on Power Systems*, vol. 19, pp. 1387-1401, 2004.
- [70] M. Gibbard, P. Pourbeik, and D. Vowles, *Small-signal stability, control and dynamic performance of power systems*: University of Adelaide Press, 2015.
- [71] T. F. Mazibuko, "Application of synchrophasors in multi-machine power system transient stability analysis", Master of Technology Electrical Engineering, Department of Electrical Engineering, Tshwane University of Technology, Pretoria, 2014.
- [72] L. R. Ankit Jah, Ashwinee Kumar, Pinak Ranjan Pati, "Transient Stability Analysis Using Equal Area Criterion Using Simulink", Bachelor in Technology in Electrical Engineering, Electrical Engineering, National Institute of Technology, 2009.
- [73] N. S. Nise, *Control Systems Engineering*, Sixth Edition ed. Asia: John Wiley & Sons, 2011.
- [74] *The Electric Power Engineering Handbook*. Auburn, Alabama: CRC Press, IEEE Press, 2001.
- [75] P. Kundur, *Power System Stability And Control*: McGraw-Hill Education, 1994.
- [76] I. S. R. W. Group, "Reader's guide to subsynchronous resonance," *IEEE Transactions on Power Systems*, vol. 7, pp. 150-157, 1992.
- [77] C. Karawita, "HVDC interaction studies using small signal stability assessment." Doctor of Philosophy Thesis, University of Manitoba, 2009.
- [78] S. S. Mvuyana, "Small signal stability assessment of the Eskom network based on measurements", Master of Science, University of Witwatersrand, 2015.
- [79] S. M'Builu-Ives, "Stability Enhancement of HVAC Grids Using HVDC Links", Master of Science, University of KwaZulu-Natal, 2016.
- [80] T. W. Shire, "VSC-HVDC based Network Reinforcement", Master of Science in Electrical Engineering, Mathematics and Computer Science, Delft University of Technology, 2009.
- [81] G. Pinares, "On the Analysis of DC Network Dynamics of VSC-based HVDC Systems", Thesis for Licentiate Degree, Department of Energy and Environment, Chalmers University of Technology, Göteborg, Sweden, 2014.
- [82] S. Lu, "DC Cable Short Circuit Fault Protection in VSC MTDC", Master of Science in Electrical Engineering, Delft University of Technology, 2015.
- [83] C. Bajracharya, "Control of VSC-HVDC for Wind Power", Master of Science in Energy and Environment, Department of Electrical Power Engineering, Norwegian University of Science and Technology, 2008.

- [84] A. D. Hansen, C. Jauch, P. E. Sørensen, F. Iov, and F. Blaabjerg, *Dynamic wind turbine models in power system simulation tool DIgSILENT*, National Laboratory Risø-R-1400, Denmark 2004.
- [85] B. Malinga, J. Sneckenberger, and A. Feliachi, "Modeling and control of a wind turbine as a distributed resource," *Proceedings of the 35th Southeastern Symposium on System Theory*, 2003, pp. 108-112.
- [86] F. Koch, I. Erlich, and F. Shewarega, "Dynamic simulation of large wind farms integrated in a multimachine network," *IEEE Power Engineering Society General Meeting*, 2003, pp. 2159-2164.
- [87] D. Peppas, "Development and analysis of Nordic32 power system model in PowerFactory." Master of Science, School of Engineering, Royal Insistute of Technology, 2008.
- [88] S. A. W. E. A. SAWEA. *SA to have 400 wind turbines spinning by year-end*. Available: <http://sawea.org.za/index.php>, 20 November 2017.
- [89] Turbines.co.za. *Wind Farms in South Africa*. Available: www.turbines.co.za, 20 November 2017.
- [90] J. Serrano-González and R. Lacal-Aránegui, "Technological evolution of onshore wind turbines—a market-based analysis," *Wind Energy*, 2016, Vol. 19 pp 2171–2187.
- [91] A. Mendonca and J. P. Lopes, "Simultaneous tuning of power system stabilizers installed in DFIG-based wind generation," *IEEE Power Tech*, Lausanne, 2007, pp. 219-224.
- [92] E. Telegina, "Impact of Rotational Inertia Changes on Power System Stability", Master of Science, Swiss Federal Institute of Technology, Zurich, 2015.
- [93] A. Mendonca and J. P. Lopes, "Robust tuning of power system stabilisers to install in wind energy conversion systems," *IET Renewable Power Generation*, vol. 3, pp. 465-475, 2009.
- [94] N. M. Razali, V. Ramachandaramurthy, and R. Mukerjee, "Power system stabilizer placement and tuning methods for inter-area oscillation damping," *IEEE International Power and Energy Conference, PECon'06*, 2006, pp. 173-178.
- [95] R. Preece, "Power System Modelling and Analysis Techniques," *Improving the Stability of Meshed Power Networks*, Ed: Springer, pp. 31-61, 2013.
- [96] Y. Zhang and R. Preece, "A comprehensive methodology for assessing power oscillation damping controllers for HVDC-based system stabilization," *IEEE PowerTech*, Eindhoven, pp. 1-6, 2015.
- [97] E. Yasoubi, M. Sedighzadeh, and A. Siadatan, "Coordinated design of PSS and TCSC controllers using colonal selection algorithm for stability enhancement of dynamical

- power system," *IEEE International Conference on Industrial Technology (ICIT)*, 2017, pp. 580-585.
- [98] Y. Lin, Z. Xu, and Y. Huang, "Power oscillation damping controller design for TCSC based on the test signal method," *IEEE Power Engineering Society General Meeting*, 2005, pp. 1671-1675.
- [99] R. Sadikovic, G. Andersson, and P. Korba, "Damping controller design for power system oscillations," *Intelligent Automation & Soft Computing*, vol. 12, pp. 51-62, 2006.
- [100] S. Subhash, B. Sarkar, and K. Padiyar, "Design of TCSC damping controller to damp Power swing oscillations," *National Power Systems Conference*, Kharagpur, 2002.

APPENDIX

This section includes additional information illustrating the block diagrams that were used in the simulation.

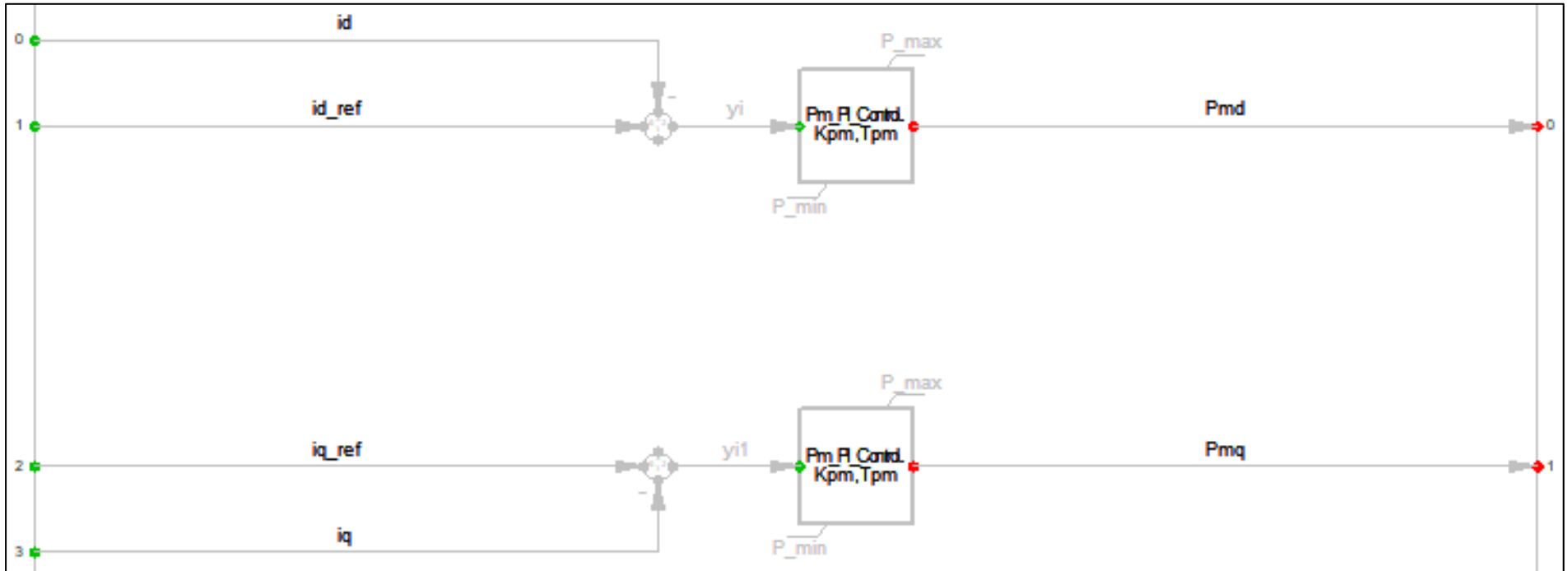


Figure A-1: Inner Controller Block Diagram

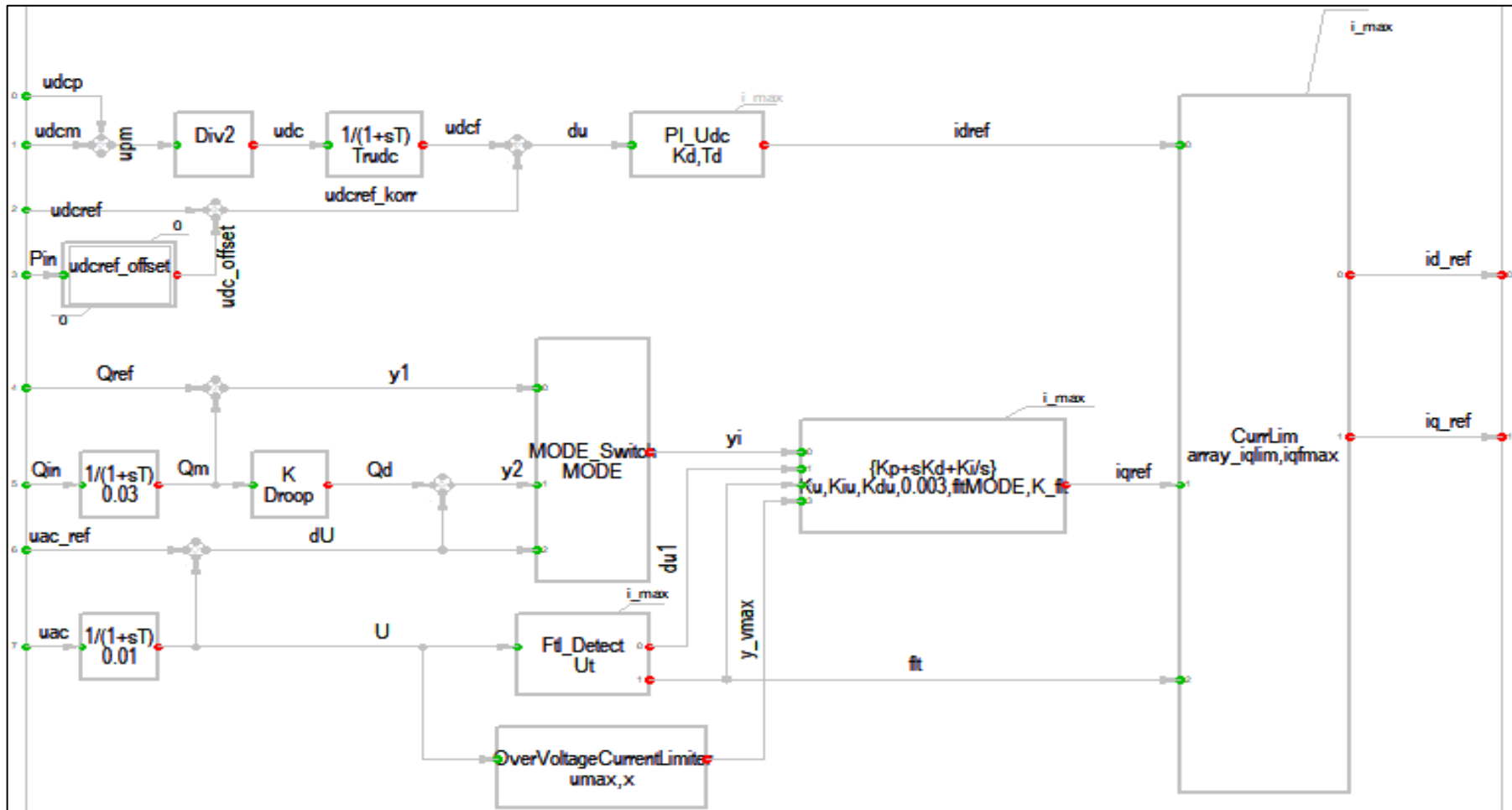


Figure A-2: Outer Control Block Diagram

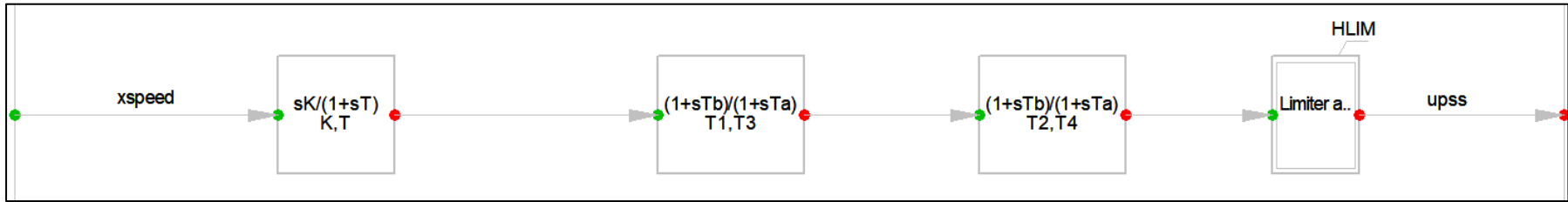


Figure A-3: Power System Stabilizer Block Diagram

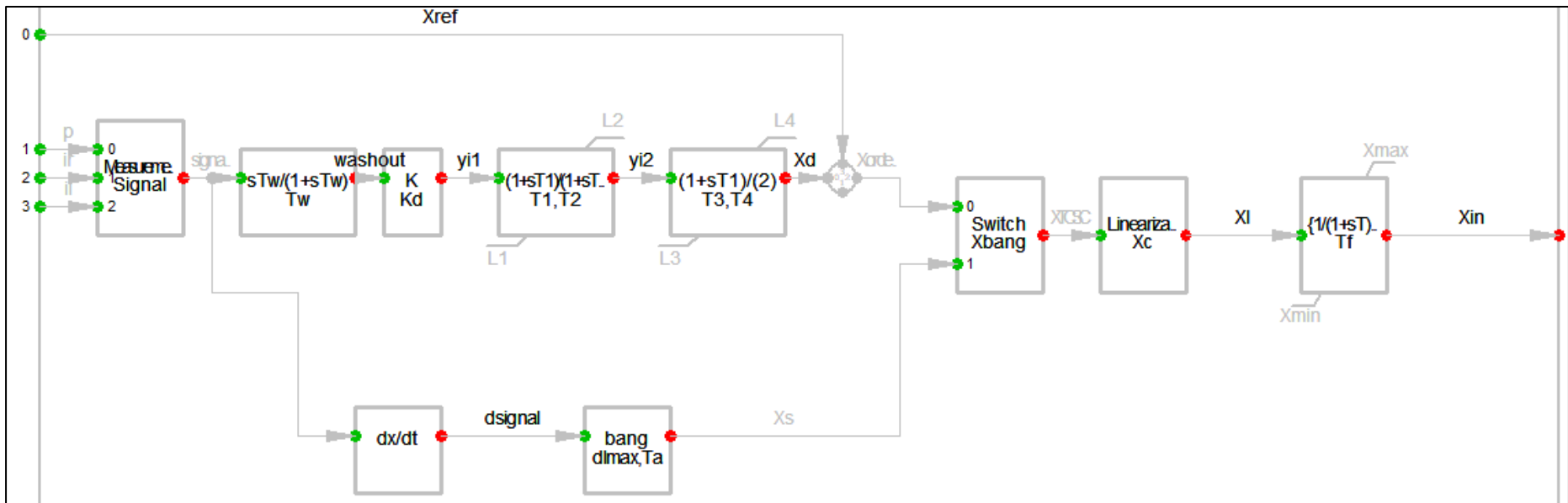


Figure A-4: TCSC Control Block Diagram

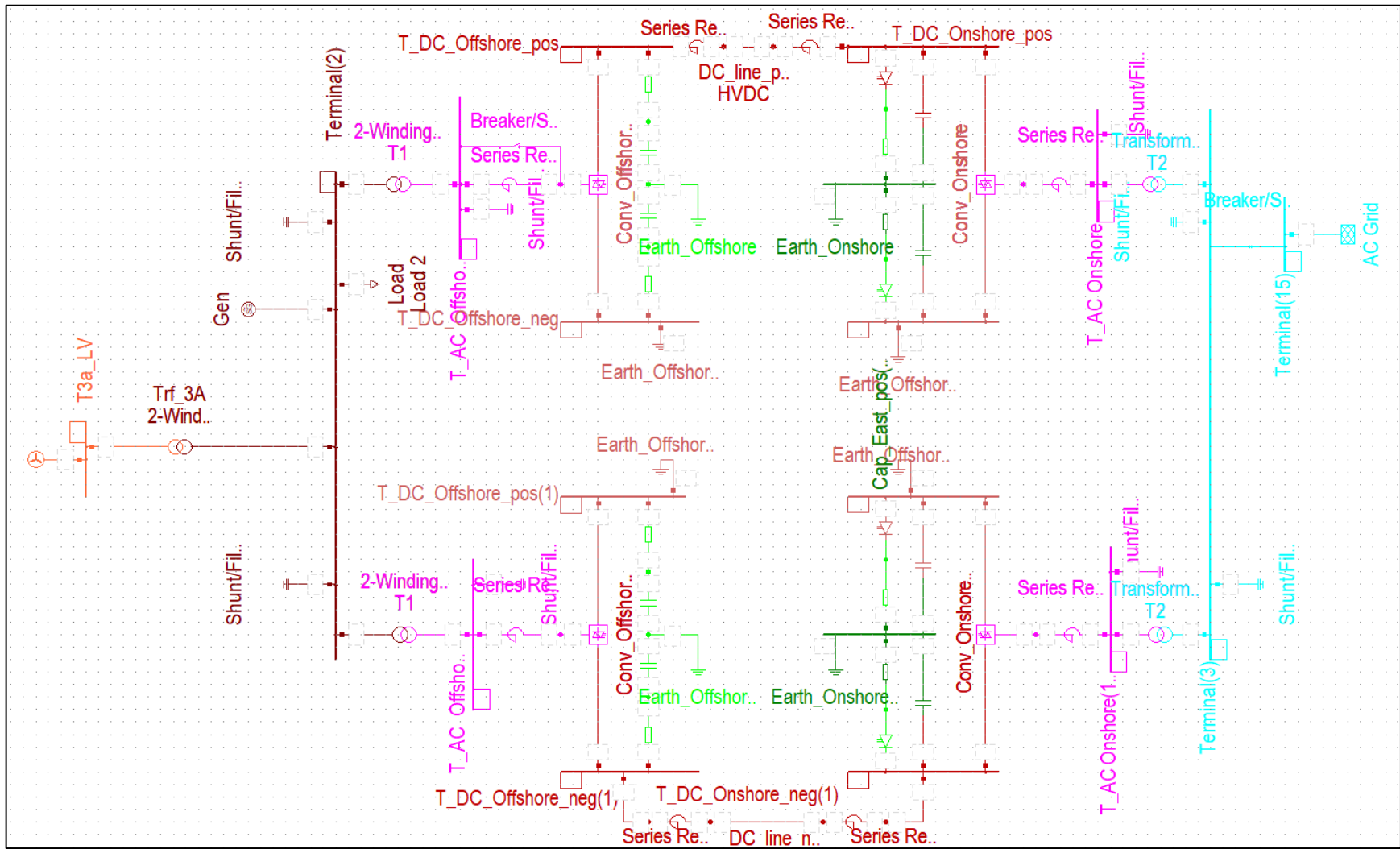


Figure A-5: Bipole Configuration

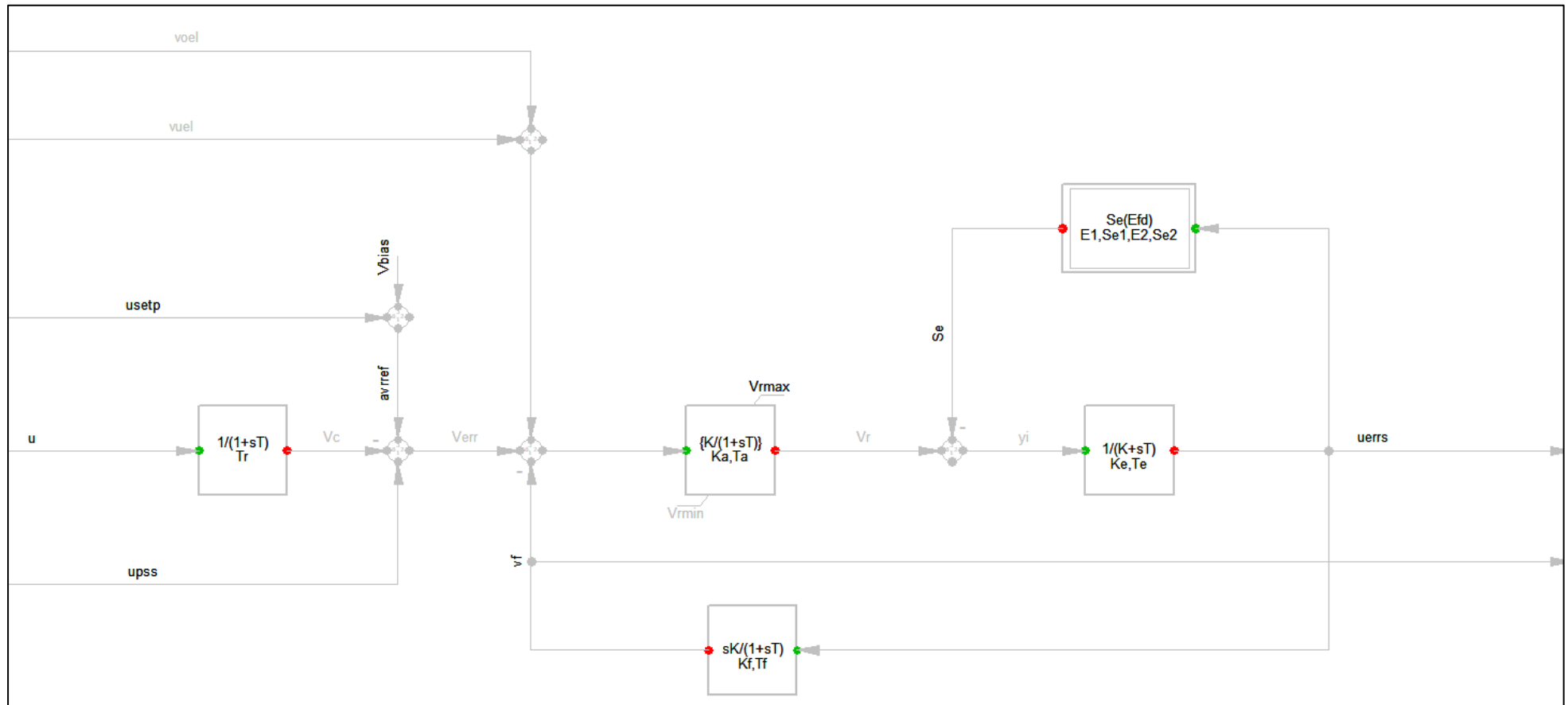


Figure A-6: Automatic Voltage Regulator 1986 IEEE Type 1 Excitation System

Table A-1: AVR Parameters

Parameter	Value
Measurement Delay T_r [s]	0.02
Controller Gain K_a [pu]	200
Controller Time Constant T_a [s]	0.03
Exciter Constant K_e [pu]	1
Exciter Time Constant T_e [s]	0.2
Stabilization Path Gain K_f [pu]	0.05
Stabilization Path Time Constant [s]	1.5
Saturation Factor 1 E_1 [pu]	3.9
Saturation Factor 2 S_{e1} [pu]	0.1
Saturation Factor 3 E_2 [pu]	5.2
Saturation Factor 4 S_{e2} [pu]	0.5
Controller Output Minimum $V_{r,min}$ [pu]	-10
Controller Output Maximum $V_{r,max}$ [pu]	10

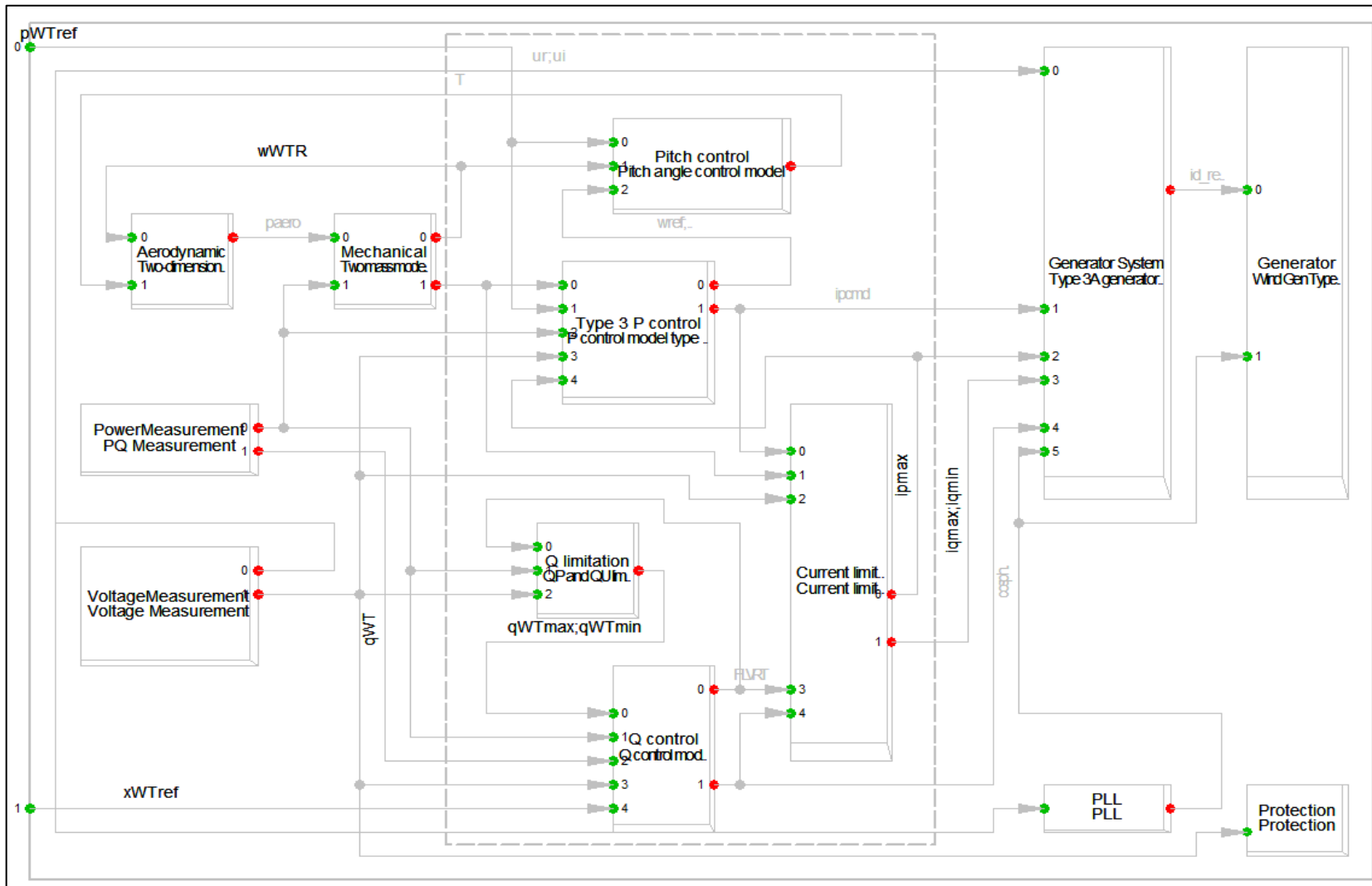


Figure A-7: Type 3 Wind Turbine Control Block Diagram